2010

Experimental study on single cement fracture exposed to CO2 saturated brine under dynamic conditions

Tevfik Yalcinkaya
Louisiana State University and Agricultural and Mechanical College, tevfikyalcinkaya@gmail.com

EXPERIMENTAL STUDY ON SINGLE CEMENT FRACTURE EXPOSED TO CO_2 SATURATED BRINE UNDER DYNAMIC CONDITIONS

A Thesis

Submitted to the Graduate Faculty of the
Louisiana State University and
Agricultural and Mechanical College
In partial fulfillment of the
Requirements for the degree of
Master of Science in
Petroleum Engineering

In

The Department of Petroleum Engineering

By
Tevfik Yalcinkaya
B.Sc., Middle East Technical University, Turkey, 2007
December, 2010

ACKNOWLEDGEMENTS

I would like to express my largest gratitude to my advisor, Dr. Mileva Radonjic for her support and guidance throughout my graduate studies. I would like to thank Dr. Stephen O. Sears and Dr. Richard G. Hughes for their valuable feedback and support as members of my thesis committee.

I would like to thank Darryl Bourgoyne, Fenelon Nunes and Gerry Masterman for their great help in setting up the laboratory. I am grateful to Dr. Clinton S. Willson and Corey Clibert for their help in image based porosity analysis. I greatly appreciate the help from Rivers Fike and Shannon Chollett for editing this thesis. I thank to Chevron Cementing Team, Weatherford Laboratories and Wanda LeBlanc for their help in conducting material characterization studies.

Finally, I would like to thank my parents, Gulcin and Suleyman Yalcinkaya and friends at LSU especially Koray Kinik, Sultan Anbar and Jose Chirinos for their support, encouragement and patience.

`

TABLE OF CONTENTS

`

`

`

LIST OF TABLES

`

LIST OF FIGURES

`

`

`

NOMENCLATURE

m_i = Molality, m (number of moles per 1 kg of aqueous solution)

z_i = Ion Charge, dimensionless

K = Equilibrium Constant, dimensionless

P_{CO2} = Partial Pressure of Carbon Dioxide (CO_2), bar

a_i = Ion Activity, dimensionless

I= Ionic Strength of an Aqueous Solution, m

γ_i =Ion Activity Coefficient, dimensionless

k = Permeability, D or m^2

ϕ = Porosity, %

b = Fracture Aperture, mm or μm

P = Pressure, psi or atm

T = Temperature, ^oC

Q = Flow Rate (bbl/day or ml/min)

w = Fracture Width (ft)

L = Fracture Length (in)

μ = Viscosity (cp)

p_f = Phenolphthalein End-point, ml

m_f = Methyl Orange End-point, ml

`

ABSTRACT

Carbon capture and storage is one of the technologies that could help reduce CO_2 concentration in the atmosphere while contributing to cutback of Greenhouse Gas emissions. Depleted oil and gas fields are favorable targets for CO_2 storage because existing wells can be readily used as injection wells. However, a number of abandoned wells also serve as gateway to the reservoir which should be considered in the context of effective Carbon capture and storage. Wellbore cement is a very essential element in wellbore systems that serve as a barrier between different zones in the subsurface. The fractures inside wellbore cement sheath, one of the possible pathways for CO_2 leakage to surface and/or fresh water aquifers, impair the effective sealing of the wellbore cement. Hence, the existence of microfractures poses a risk for Carbon capture and storage.

The purpose of this experimental study is to gain understanding about the effect of acidic brine on the behavior of cement fracture and porosity. Two experiments were conducted, one under atmospheric and one under high pressure conditions, using CO_2 saturated brine. Fracture widening was observed in CT images of the low pressure experiment and was verified with pressure drop calculations. The low pressure experiment resulted in the reduction of porosity whereas the high pressure experiment resulted in a slight increase in porosity. The porosity reduction was caused by calcite deposition which was confirmed by mineralogical analysis, ESEM images and effluent brine analysis. There were 2 mechanisms working simultaneously: leaching and precipitation (carbonation). It appeared that leaching took place first and drove the carbonation process. Leaching resulted in an increase in porosity whereas carbonation resulted in a reduction of porosity. In a possible leakage scenario, acidic brine exposure may result in a reduced fracture aperture due to carbonation coupled with confining stress around cement sheath.

`

CHAPTER 1

INTRODUCTION

1.1 Background

Statistics indicate that the concentration of carbon dioxide (CO_2) in the atmosphere is 388 ppm[1] (the pre-industrial level was 280 ppm[2]). Increasing awareness of climate change has led to extensive research and development of possible solutions to mitigate the effects of global climate change caused by greenhouse gases (GHG). Carbon Capture and Storage (CCS) technology is proposed as one of the steps to reduce atmospheric CO_2. The Intergovernmental Panel on Climate Change[3] (IPCC) defines CCS as "a process consisting of the separation of CO_2 from industrial and energy-related sources, transport to a storage location and long-term isolation from the atmosphere". Depleted oil and gas reservoirs are one of the favorable candidates for CO_2 storage because their subsurface geology is well known, and infrastructure, such as wells and pipelines already exist. For safe, sustainable and economic CCS projects, abandoned wells in fields used for carbon sequestration should not have conductive pathways for injected CO_2 to escape back to the surface. During the life of a well, the wellbore system experiences many pressure and temperature cycles due to completion, injection, and production operations, which can cause microannulus formation and/or fracture propagation in the wellbore cement. Cement fractures are identified as one of the potential leakage pathways for stored CO_2 to migrate along the wellbore back to the surface. Before implementing a storage project, the integrity of any existing wellbore network should be analyzed against the possible leakage scenarios. Behavior of cement fractures in CCS environment under long time periods (hundreds of years) should be understood as a part of the risk assessment process. Safe subsurface containment of CO_2 is manageable with the help of adequate monitoring and established remediation measures, which

`

can be deployed when required.

1.2 Objective

The objectives of this experimental study are to evaluate the change in the fracture aperture and investigate porosity alterations of neat, class-H Portland cement when exposed to CO_2 saturated brine through a controlled single fracture. The porosity is primarily affected by the dissolution and precipitation reactions occurring due to incompatibility of the highly alkaline cement system and acidic brine. Two reaction mechanisms take place which have opposite effects on porosity: leaching of cement and carbonation of Portlandite. In order to identify the dominant mechanism, a through material characterization of reacted cement was carried out, both qualitatively and quantitatively.

1.3 Methodology

To reach the stated objectives, flow-through experiments were conducted using 1 in by 12 in cement cores prepared using class-H cement (water to cement ratio-w/c=0.38). CO_2 saturated brine was obtained by bubbling CO_2 through a brine reservoir. Two sets of experiments were carried out using CO_2 saturated brine with 2 ml/min at different injection pressures to determine the effect of pressure on the porosity alteration. Quantitative and qualitative material characterization techniques were employed to have an understanding about chemical reactions between the cement and CO_2-brine system. Effluent brine samples were analyzed to support findings from analytical techniques.

1.4 Overview of Thesis

Chapter 1 outlines global climate change and Carbon Capture Storage (CCS) technology as a solution to reduce CO_2 concentration in the atmosphere. Next, objective and methodology of this study are presented.

`

Chapter 2 includes a literature review on relevant topics such as global carbon dioxide emissions, wellbore cements, and data from experimental and field studies in the literature related to cement degradation in CO_2-brine environments.

Chapter 3 describes the experimental set-up and procedures utilized to reach the proposed research objectives. Material characterization techniques, employed to understand the alterations in the cement internal structure, along with cement sample preparation and curing process are also documented in this chapter.

Chapter 4 provides the results of flow-through experiments with varying injection pressures. Microstructural characterization data, effluent brine analysis and porosity measurements are reported in Chapter 4 as well. The discussion section compares the reported data to similar studies.

Chapter 5 briefly summarizes this research and gives conclusions based on the interpretation of the experimental data. Recommendations are also made for improving the future experiments on durability of cement in acidic brine environments.

`

CHAPTER 2

LITERATURE REVIEW

The objective of this study is to understand the change of the porosity/permeability in fracture surfaces within wellbore cement due to CO_2 saturated brine exposure at two different injection pressures. A through literature review is presented in this chapter covering a wide range of subjects from CCS technology to flow-through fracture theory and deterioration of cement.

2.1 Carbon Dioxide (CO_2) Sources and Emissions

According to the Environmental Protection Agency (EPA) estimates, greenhouse gas emissions including carbon dioxide, methane, nitrous oxide and hydrofluoracarbons (HFCs) were 6,956.8 million metric tons of CO_2 equivalents in 2008, and U.S. CO_2 emissions alone from fossil fuel combustion were estimated as 5,572.8 million tons[4]. Stationary sources, which have a permanent location, constituted nearly 70% of the CO_2 emissions and the remaining portion was emitted from the transportation sector. Approximately 47% of the CO_2 emissions are produced by the refineries/chemical industry. Figure 2.1 shows CO_2 emissions (million tons) from different fossil fuel combustions based on the IEA estimates globally.

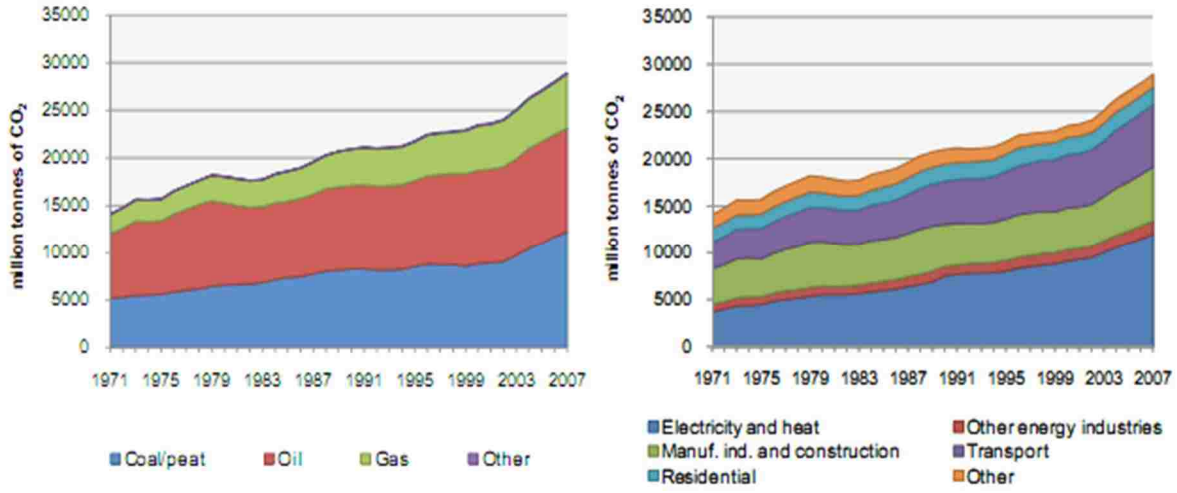

Figure 2.1: CO_2 Emissions from Fossil Fuel Consumption (IEA, 2009)[5]

`

2.2 Carbon Capture and Storage (CCS)

Carbon, capture and storage (CCS) is a proposed technology that could help reduce CO_2 concentration in the atmosphere. CCS starts with capturing CO_2 from major sources such as power plants, then processing it into a pure state, compressing it to the supercritical phase, and finally injecting it into a suitable geologic formation where it will be trapped for hundreds to thousands of years by means of the following trapping mechanisms[6];

- Physical Trapping (Structural and Stratigraphic Trapping): After CO_2 is injected it rises upward due to density difference with the formation water. Its migration will terminate when it encounters an impermeable layer which can be a structural or stratigraphic trap.
- Residual Trapping: As a CO_2 plume is moving in the reservoir, some amount of CO_2 is left behind at the tail of the plume due to pore spaces. With time, the saturation of CO_2 left behind the plume decreases and when it becomes lower than critical gas saturation, it becomes immobile and trapped.
- Solubility Trapping: Some amount of injected CO_2 goes into formation brine solution. The solubility of CO_2 inside the brine is affected by salinity, pressure and temperature.
- Mineral Trapping: After dissolving in formation brine solution, CO_2 in the solution will form carbonic acid (H_2CO_3). Carbonic acid can react with the minerals that exist in the reservoir to form solid carbonates which are immobile. Mineral trapping is the most favorable trapping mechanism since CO_2 becomes incorporated in mineral structure.

The activity levels of trapping mechanisms will be different during the life of the CCS project as shown in Figure 2.2. Mineral trapping starts to be active over long time scales. The containment of CO_2 underground becomes more secure from physical to mineral trapping.

`

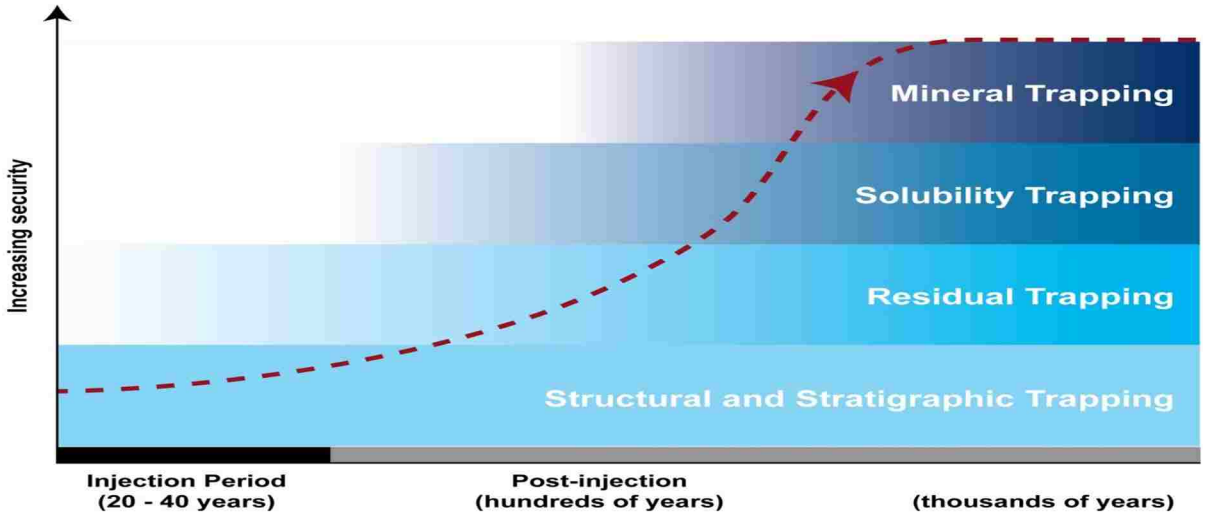

Figure 2.2: Trapping Mechanisms (downloaded from CRC Australia website)[7]

2.2.1 Capture

CO_2 can be captured with three different methods such as post-combustion, pre-combustion and oxy-fuel combustion[8,9]. The cost of each method is different and carbon recovery rates are different. The estimated cost of capturing CO_2 with current techniques is $150 per ton[10].

- Post-combustion: CO_2 can be separated from flue (exhaust) gases produced from burning fossil fuels in the air. The small volume of CO_2 in the flue gas (ranging from 3-15% by volume) is captured by dissolving the CO_2 into a liquid solvent such as amines, a class of organic chemical compounds.
- Pre-combustion: Fossil fuels can be separated into hydrogen and carbon dioxide before they are burnt. This process produces high concentrations of CO_2 between 35% and 45%.
- Oxy-fuel combustion: This method employs burning the fuel in an oxygen environment instead of air and results in an exhaust gas consisting only of concentrated CO_2 and water vapor. The CO_2 is typically greater than 80% by volume. This method results in the highest recovery of CO_2.

`

2.2.2 Storage

After CO_2 is captured and transported, storage operations will be implemented in a suitable geologic formation by injecting CO_2 at least at 1,071 psi (75.3 atm) and 31 ^oC for conversion from gas state to supercritical state[3,9]. Suitable storage sites for CO_2 sequestration are depleted oil and gas reservoirs, deep saline aquifers and unmineable coal beds[11].

- Depleted oil and gas reservoirs are favorable locations for storing CO_2 since detailed knowledge already exists about the geologic structure. Numerous active abandoned wells give access to the reservoirs, and they can be converted into CO_2 injection wells. These wells require attention: wellbore integrity studies about possible leakage risks should be carried out before implementing storage projects in depleted oil and gas fields.
- Saline aquifers have the largest volume available for storage which is shown for North America in Table 2.1. However, they are not as thoroughly characterized as depleted oil and gas reservoirs, and they do not have many wells penetrating into the target formations.
- Unmineable coal beds can be used if they are located below depths that cannot be economically extracted. The disadvantage is the depth window for this storage site is between 600-1,000 m which limits available volume for CO_2 storage[11].

The target formation should be at a minimum depth of 800-1,000 m to provide sufficient pressure to provide enough pressure for injected CO_2 to stay in the supercritical state[3,6,9]. In order to select a geologic storage location, three criteria should be considered; capacity, containment and injectivity[3,9]. The geologic formation should have enough capacity (pore volume) to store the injected volume of CO_2. Wellbore systems penetrating the storage reservoirs, faults, and caprocks should be impermeable to serve as a seal to prevent CO_2

`

migration from reservoir where it confined. Permeability of the formation should be enough to allow injection of CO_2 depending on the surface pressure limitations.

Table 2.1: Available Capacity for Carbon Storage in North America (2008 Carbon Sequestration Atlas of the United States and Canada) [12]

Depleted Oil and Gas Reservoirs	152 billion tons
Unminable Coal Seams	173-196 billion tons
Deep Saline Aquifers	3,634-13,909 billion tons

2.2.3 CO_2 Injection and Post-Injection

CO_2 is typically injected in its supercritical state to employ the maximum usage of the reservoir capacity[3,9]. Supercritical CO_2 ($SCCO_2$) has the highest density therefore it occupies the lowest volume among other CO_2 phases. After injection operations, some portion of the $SCCO_2$ goes into the brine solution. Depending on the pressure, temperature, and salinity conditions, some portion of the injected CO_2 does not dissolve. The undissolved CO_2 tends to rise upward due to density difference with the formation brine[13]. Some of the $SCCO_2$ may be converted to gaseous CO_2 when the pressure and temperature conditions are enough for supercritical transition. During injection, CO_2 displaces the brine that exists near the wellbore region. After injection is terminated, the pressure pulse created by the injection of CO_2 will dissipate with time[11]. The formation brine will migrate back towards the wellbore region, pushing injected CO_2 upwards due to density difference after the pressure pulse has dissipated[13]. Therefore, in the post injection period there is a high possibility that the wellbore cement will be exposed to CO_2 rich brine and this will be one of the main motivations for this study. This study is focused on

`

mimicking this scenario in the laboratory.

2.2.4 Outlook at Current and Planned CCS Projects Worldwide

There are three large scale projects currently in operation worldwide. The following list is ordered chronologically[14].

- Sleipner-Norway; 1 MM ton/year is injected to a saline aquifer since 1996, Statoil
- Weyburn-Canada, 1.2 MM ton/year is injected to a depleted oil reservoir since year 2000, JV between the governmental and major oil companies.
- In-Salah-Algeria, 500,000+ ton/year is injected to a saline aquifer since 2004, BP and Statoil

According to the National Energy Technology Laboratory (NETL) CCS database[15], there are around 190 other projects in 20 countries around the world.

2.2.5 Concerns about CCS Technology

Although CCS seems like the most feasible method for reducing atmospheric carbon content, there are concerns associated with this technology. The primary concern is that stored CO_2 will not stay underground for hundreds to thousands of years but instead migrate to upper formations (including the fresh water aquifers) and/or surface that will raise Health, Safety and Environment (HSE) issues[16]. The financial burden for countries is another concern. Compression and capturing cost in the US is estimated to be $91.90 billion in 2010[16]. Also, some researchers claim that CO_2 can occupy only 1% of the pore volume and injectivity will be reduced with time due to interaction between CO_2 and the reservoir rock[17]. This experimental study only focuses on the leakage potential of CO_2 through wellbores, not capacity. There are numerous depleted oil and gas fields which are planned to be converted to carbon storage locations. These fields have tens to thousands of abandoned wells, e.g. Alberta, Canada and West Texas, USA. For safe,

`

sustainable and economic CCS projects, abandoned wells in the fields used for CO_2 storage should not have conductive pathways for CO_2 to escape back to the surface. Pathways such as microannuluses between casing and cement and/or microfractures inside the cement sheath may act as potential leakage conduits for CO_2. Also the fluid adjacent to the wellbore cement also has some implications on the cement integrity. To understand the possible leakage problem through the wellbore cement, an understanding about cement and its interaction with CO_2-brine mixtures over extended periods of time and under dynamic conditions is essential.

2.3 Portland Cement and Its Usage in Petroleum Industry

2.3.1 Portland Cement Chemistry

In the petroleum industry Portland cement is the primary cement used for applications such as wellbore cementing (primary and remedial) and well abandonment. The chemical composition of Portland cement is predominantly Calcium (Ca^{2+}) and Silicon (Si^{4+}). It has four major minerals[18]. These are Alite, Belite, Aluminate and Ferrite. Table 2.2 shows alternative names and chemical compositions of these minerals.

Table 2.2: Mineral Phases in Portland Cement[18]

Alite	Tricalcium Silicate (Ca_3SiO_5)	C_3S
Belite	Dicalcium Silicate (Ca_2SiO_4)	C_2S
Aluminate	Tricalcium Aluminate ($Ca_3Al_2O_6$)	C_3A
Ferrite	Tetracalcium Aluminoferrite ($Ca_4Al_2Fe_2O_{10}$)	C_4AF

The silicate phases (C_3S and C_2S) comprise more than 80% of the Portland cement. Hydration takes place when cement is mixed with water. After complete hydration of cement, two main products are formed: Calcium Silicate Hydrate ($3CaO{\cdot}2SiO_2{\cdot}3H_2O$ or C-S-H)[18], which constitutes 70% of the hydrated cement and is the main binding material and Portlandite

`

($Ca(OH)_2$), which occupies 15- 20 % of the volume after hydration. There are also other minor minerals formed as a result of hydration such as Ettringite ($(CaO)_6(Al_2O_3)(SO_3)_3.32\ H_2O$). Even after partial hydration, the cement undergoes volumetric shrinkage due to the lower volume of hydration products. The cement pore solution (pore water) is highly alkaline (pH~13), depending on the water to cement ratio. The long curing times (it is reported that cement is hydrated 70% in 28 days[18]) may result in the conversion of the $Ca(OH)_2$ to C-S-H that leads to reduction in porosity and permeability.

2.3.2 Portland Cement in Wellbore Cementing

Because oil and gas wells drilled vary in terms of wellbore profiles and depths, there are many different cement formulations to satisfy the different needs associated with different well depths, formation fluids, pressures and temperatures. Cements are classified according to degree of sulfate resistance and hydration rate[18]. Therefore, they have different water to cement (w/c) ratios. Cements are available in the market from class-A to H to address different cementing needs[19]. Class-A (w/c=0.46) type of cement is manufactured for use up to 6,000 ft as a basic cement type without additives[19]. Class-G (w/c=0.44) and class-H (w/c=0.38) cements can be used up to 8,000 ft without additives but using additives it can be used in deeper depths. As the particle size of the cement gets smaller, the surface area (measured in Blaine fineness, m^2/kg or cm^2/gr) gets larger and hydration takes place at a more rapid pace. Class-H cement has 1,600 cm^2/gr of Blaine fineness whereas class-G has 1,800 cm^2/gr of fineness[18]. Class-H cement (w/c=0.38) has larger particle sizes and class-G (w/c=0.44) cement hydrates faster than class-H cement. Cement additives are used to obtain desired setting time such as accelerators and retarders. The most common accelerator used in cementing operations is $Ca(Cl)_2$. Lignosulfonates are typically used as a

`

retarder. Additives such as fly ash can be added to decrease the permeability of the cement system.

2.3.3 Wellbore Cementing

Oil and gas wells are cased and cemented based on pore and fracture pressure profiles to reach Total Depth (TD) safely. Primary cementing is carried out using a bottom plug, a top plug and a spacer. Upon reaching the target depth for a particular well section, the drillstring and bottomhole assembly (BHA) is pulled out of the hole (POOH). The drilling fluid (mud) is conditioned and mud cake on the formation walls is removed for a better displacement process. A casing string is run and a casing shoe is placed at the bottom of the casing string and float collar (where the top and bottom plug land) is placed 2-3 joint of casings above the casing shoe which consists of a float valve. Prior to the cementing operation, the lines are pressurized and checked against any leaks. The cementing operation starts with pumping the spacer together with the bottom plug, which allows fluid to flow through. The spacer pushes the mud and stays under the mud column in the annulus[20]. Secondly a tail cement slurry is pumped followed by the lead cement slurry. It pushes the spacer keeping the mud and cement slurry separated. Finally, the top plug is placed using the mud, and pressure build up is observed on the stand pipe when the top plug is placed. Once the cementing operation is completed, the wait on cement (WOC) period starts and depending on the laboratory tests, drilling of the next section begins after WOC time. There are other cementing methods available such as 2-stage cementing and dump bailer method[18,20].

Cemented holes are evaluated with well logs such as the Cement Bond Log (CBL) and the Variable Density log (VDL). A CBL qualitatively determines the bond quality of cement to the casing and may give an approximation of where the cement top (TOC) is.

`

In the case of an unsuccessful primary cementing, secondary cementing attempts are made to offset the possible effects of an unsuccessfully cemented hole on the life of the well.

Oil and gas wells are cemented for three main reasons:

- Zonal Isolation
- Structural support for the wellbore
- Casing protection against corrosive fluids

Amongst these reasons, zonal isolation is the most critical point for the long-term and safe CCS projects since containment of injected CO_2 in the subsurface is directly related to the isolation of zones. Hence, additional literature about zonal isolation is presented in the following section.

2.3.4 Zonal Isolation

The zonal isolation function of wellbore cement is to prevent unwanted fluid entry into wellbore which may eventually lead to Sustained Casing Pressure (SCP). SCP is defined as the casing pressure caused by trapped gas or liquid in the annulus, which can only be bled off temporarily[21]. Nelson and Guillot[22] reports that 11,000 casing strings in over 22,000 oil and gas wells in the Gulf of Mexico show sustained casing pressure which is an indication of inadequate zonal isolation. In order to achieve the zonal isolation function, the wellbore should be properly cased and cemented. SCP has three main causes given by Bourgoyne et al.[21]:

- Tubing and casing leaks
- Poor primary cementing
- Damage to primary cement during the life of the well

Tubing and casing leaks lead to migration of the fluid from reservoir to behind the casing resulting in annular pressure. Poor primary cementing can arise from not following the proper

`

cementing practices such as conducting the cement job without having a complete mud cake removal from the formation face. Due to insufficient mud cake removal, the cement will not form a strong bond to the formation face and which will eventually lead to a microannulus and/or microfractures[22].

Damage to primary cement is most possible in abandoned oil and gas wells some of which already have 30-50 years of service life. Primary cement can be damaged due to many pressure and temperature cycles caused by oilfield operations such as completion, pressure testing, production, and stimulation during the life of the well[23]. Since the thermal expansion and elasticity coefficients are different for casing and cement, the pressure and temperature change in the casing can result in a different expansion and contraction in cement which increases the possibility of forming a microannulus between casing and cement and/or microfractures within the cement sheath (Figure 2.3).

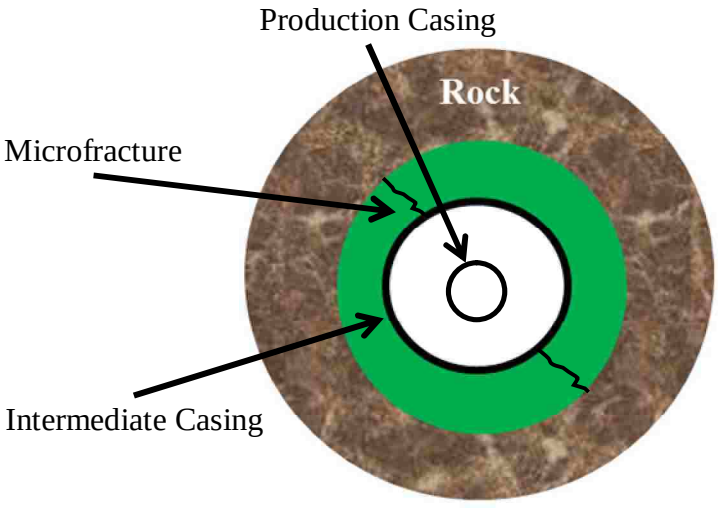

Figure 2.3: Schematic of Fractured Cement Sheath

`

2.3.5 Experimental and Simulation Studies on Wellbore Cement Integrity

There are numerous experimental studies reported in the literature which investigate the effects of wellbore stresses on cement integrity.

Ravi et al.[23] simulated the effect of wellbore stresses on the wellbore cement using Finite Element Analysis (FEA). They studied three different types of cement with different physical properties such as Young`s modulus and volumetric shrinkage in two different well geometries. Hydration of cement, depressurization of 3,750 psi caused by changing the fluid (13 lb/gal) to completion fluid (8.6 lb/gal) for a 16, 500 ft well and pressurization of 10,000 psi caused by hydraulic fracturing of the casing were simulated. Their results indicate that conventional oilwell cement (4% shrinkage and Young`s modulus of 1.2 x 10^6 psi) failed and de-bonded from casing at the end of the depressurization of the casing and pressurization resulted only in failure of cement not de-bonding from casing. On the other hand, cement with no volumetric shrinkage properties did not fail in any of the pressurization and depressurization simulations.

Boukhelifa et al.[24] studied the effect of casing expansion and contraction on the cement sheath using an experimental set-up with a core in the center, cement in the annulus and an outer ring simulating the casing. They tested conventional neat cement. They rotated the inner core to simulate the contraction and expansion of the casing. Single rotation corresponds an outer radial displacement of 30 μm which corresponds to 116 psi change inside the casing according to the calibration of their strain gauge. Initial permeability of the whole system was 7-8 mD (7-8x10^-15 m^2). They observed a permeability increase (measured using air) which indicated a microannulus was formed after 0.5 turns. Permeability was reduced after 2.5 turns indicating closure of the microannulus. However, radial cracks were observed on the cement surface. Three turns resulted

`

in opening of cracks and further turns lead to an increase in permeability to 1,000 mD ($10^{\wedge-12}$ m^2).

2.4 Geochemistry of Carbon Dioxide (CO_2) and Brine Mixture

2.4.1 Carbon Dioxide (CO_2)

Carbon dioxide has been used by the food industry, the oil industry, and the chemical industry. The petroleum industry has many years of experience using CO_2 for Enhanced Oil Recovery (EOR). CO_2 can exist in solid, gas, liquid and supercritical phases at different pressure and temperatures as shown Figure 2.4. At 25 ^oC, gaseous CO_2 liquefies around 800 psi[25]. CO_2 becomes supercritical when the pressure is above 1,071 psi and temperature is above 31 ^oC [3,9,13,14]. Supercritical CO_2 has a high density comparable to a liquid (density of 506 kg/m^3 at 1,071 psi and 31C^o) and viscosity comparable to a gas in the range of 0.02-0.1 centipoises[26]. CO_2 may also become dangerous to human health if its concentration exceeds 5,000 ppm[27].

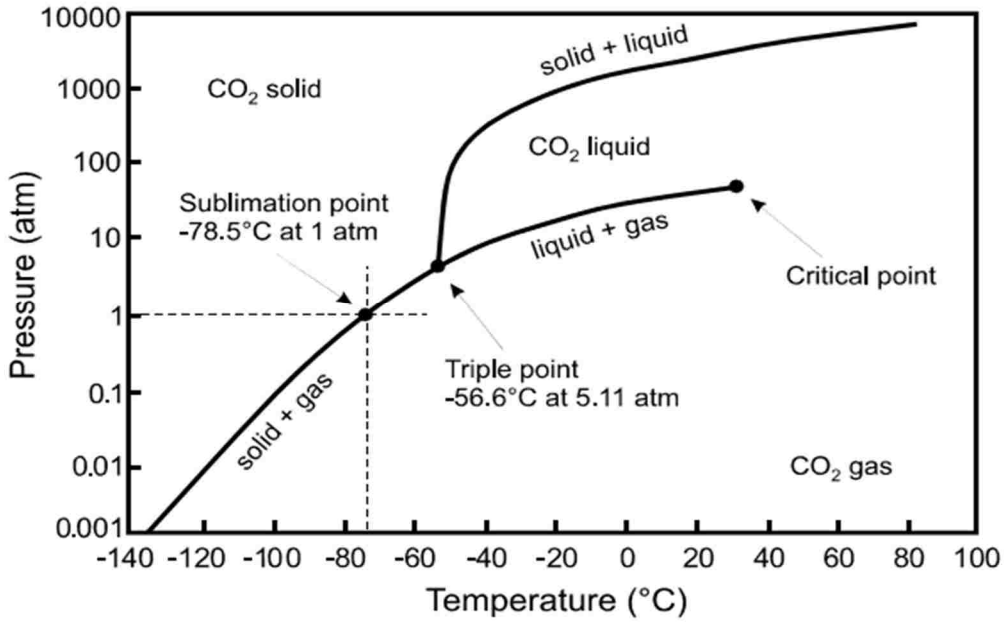

Figure 2.4: CO_2 Phase Diagram (downloaded from the Department of Chemistry website, University of Wisconsin) [25]

`

2.4.2 CO_2 Addition to Fresh Water

When CO_2 is introduced to water, carbonic acid (H_2CO_3) is formed (Equation 1). After the acid evolution, the pH of the solution drops until reaching equilibrium. Carbonic acid is also dissolved to produce bicarbonate (HCO_3^-) and further reaction results in forming the carbonate ions (CO_3^{-2}) [28]. The equilibrium constant for carbonic acid formation is given in Equation 2.

$$CO_2 + H_2O \Rightarrow H_2CO_3 \quad \text{.....(1)}$$

$$K_{CO2} = \frac{a_{H_2CO_3}}{a_{H2O} \times a_{CO2}} \quad \text{.....(2)}$$

where "a" stands for the activity. K_{CO2} is the equilibrium constant.

Activity is the multiplication of the activity coefficient (γ_i) and the molality (m_i). The activity coefficient can be calculated using Davies (Equation 4) or Debye-Huckel equations[29]. Davies equation is the simplified version of Debye-Huckel equation and it is reported to be valid until a few tenths molal ionic strength[29]. Ionic strength (I) is defined as;

$$I = 0.5 \times \sum m_i \times (z_i)^2 \quad \text{.....(3)}$$

where, m_i is the molality (mol/kg) and z_i is the charge of each ion.

$$\log(\gamma_i) = \frac{(-0.5091) \times (z_i)^2}{1+\sqrt{I}} + 0.102(z_i)^2 I \quad \text{.....(4)}$$

If the activity of CO_2 is replaced with its equivalent partial pressure, then Equation 2 can be written in an alternate way (Equation 5). Activity of H_2O can be assumed as 1 for aqueous solutions. Partial pressures of carbon dioxide are tabulated in the literature for different temperature and pressures[29]. ($P_{CO2}=10^{-3.5}$ bar at atmospheric conditions)

$$a_{H_2CO_3} = K_{CO_2} \times P_{CO_2} \quad \text{.....(5)}$$

`

The carbonic acid dissolution reaction is given by,

$$H_2CO_3 \Rightarrow H^+ + HCO_3^- \quad \text{.....(6)}$$

The equilibrium constant for this reaction is,

$$K_1 = \frac{a_{H^+} \times a_{HCO_3^-}}{a_{H_2CO_3}} \text{ and } K_1 = 10^{-6.35} \text{ at atmospheric conditions} \quad \text{.....(7)}$$

Equation 7 can be rewritten as,

$$a_{H+} = -\log(pH) \text{ and } a_{HCO_3^-} = \frac{K_1 \times a_{H_2CO_3}}{-\log(pH)} \quad \text{.....(8)}$$

The equilibrium constant for the bicarbonate dissolution reaction is given in Equation 10,

$$HCO_3^- + H^+ \Rightarrow CO_3^{-2} \quad \text{.....(9)}$$

$$K_2 = \frac{a_{CO_3^{-2}}}{a_{H+} \times a_{HCO_3^-}} \text{ and } K_2 = 10^{-10.33} \text{ at atmospheric conditions} \quad \text{.....(10)}$$

The activity of bicarbonate ions can be written in terms of the partial pressures and equilibrium constants,

$$a_{HCO3-} = \frac{K_1 \times a_{H_2CO_3}}{a_{H+}} = \frac{K_1 \times K_{CO2} \times P_{CO2}}{-\log(pH)} \quad \text{.....(11)}$$

$$\sum \text{Dissolved } CO_2 = m_{H_2CO_3} + m_{HCO_3^-} + m_{CO_3^{-2}} \quad \text{.....(12)}$$

If the pH of the solution is below 7, then the concentration of carbonate ion can be neglected (Figure 2.5).

Using Equation 12, the amount of dissolved CO_2 in the solution can be computed by knowing the molality of carbonic acid, bicarbonate and carbonate ions. Numerous studies exist in the literature which model the solubility of CO_2 in fresh water such as Duan-Sun[30] model which is developed for solutions containing Na^+ and Cl^-. Bicarbonate and carbonate concentrations are equal at a pH of 10.33[28,29,31]. At pH of 6.35, carbonic acid and bicarbonate concentrations are equal as shown in Figure 2.5.

`

For our study, it is important to determine whether calcite was precipitating or dissolving. Oversaturated or undersaturated aqueous solutions can be identified using a saturation index (SI) value criteria. The ion activity product (IAP) is the product of the activity of calcium and the activity of the carbonate ion, which can be calculated with Equation 13.

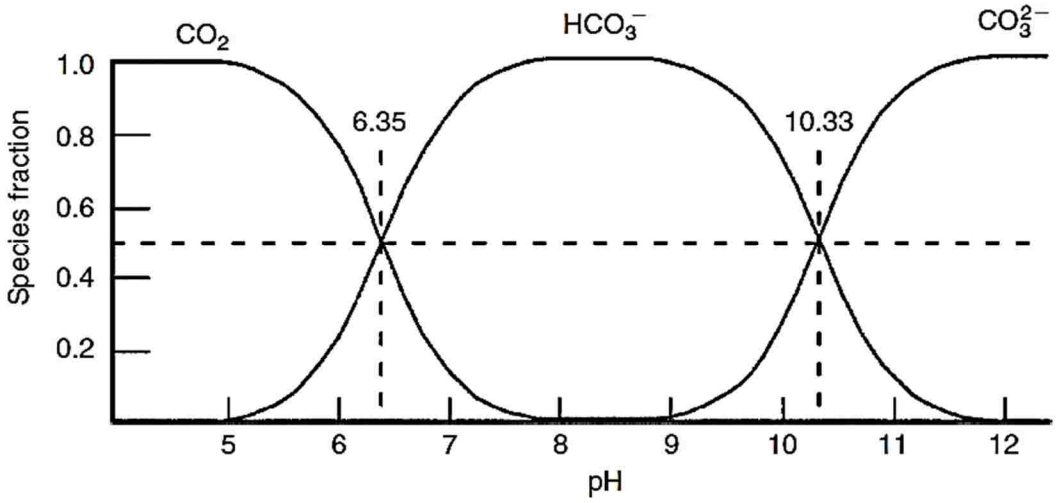

Figure 2.5: Activity of Carbonate, Bicarbonate and Carbonic Acid as a Function of pH (Applications of Environmental Aquatic Chemistry, Weiner E.) [32]

$$IAP = a_{Ca^{2+}} \times a_{CO_3^{-2}} \quad \text{..... (13)}$$

The saturation index is then,

$$SI = \log\left(\frac{IAP}{K_{sp}}\right) \quad \text{..... (14)}$$

Equilibrium constant (K_{sp}) can be obtained from geochemistry books[29,32]. K_{sp} can be adjusted to different T and P conditions by correction factors[29]. K_{sp} is equal to $10^{-8.48}$ at atmospheric conditions[29].

If the saturation index (SI) is less than zero, the brine solution is undersaturated and calcite dissolves. If SI is larger than 0, then the brine solution is precipitating calcite.

`

2.4.3 CO_2 Addition to Brine Solution

The solubility of CO_2 in brine solutions is different than the solubility of CO_2 in fresh water due to total dissolved solids (TDS), such as Na^+, Cl^- and K^+ in the brine solution. Solubility of CO_2 decreases with increasing salinity because the activity coefficient increases with salinity[33]. As pressure drops, the solubility of CO_2 in brine also reduces.

2.4.4 Chemical Interaction between Portland Cement and CO_2 Saturated Brine

When cement is exposed to CO_2 saturated brine, a series of chemical reactions[35,36,37] take place as summarized below;

$$CO_2 + H_2O \Rightarrow H_2CO_3 \quad \text{.....(15)}$$

$$Ca(OH)_2 + H_2CO_3 \Rightarrow CaCO_3 + H_2O \quad \text{(Also called as carbonation)} \text{.....(16)}$$

$$H_2CO_3 + CaCO_3 \Rightarrow Ca(HCO_3)_2 \quad \text{.....(17)}$$

$$Ca(HCO_3)_2 + Ca(OH)_2 \Rightarrow 2CaCO_3 + H_2O \quad \text{.....(18)}$$

After $Ca(OH)_2$ has been consumed, $CaCO_3$ begins to dissolve.

$$H^+(aq) + CaCO_3(s) \Rightarrow Ca^{+2}(aq) + HCO_3^-(aq) \quad \text{.....(19)}$$

Consumption of the hydrogen ions (H^+) results in a pH increase.

If all $CaCO_3$ is depleted then Calcium Silicate Hydrate (C-S-H), due to Ca^{2+} leaching, will be converted into a gel like structure[36] and wellbore cement will lose its integrity.

$$C-S-H(s) \Rightarrow Ca^{+2}(aq) + OH^-(aq) + \text{amorphous gel} - SiO_2(s) \quad \text{.....(20)}$$

The pH of the pore solution of cement decreases to 8 when the carbonation is totally complete[38]. In the literature, phenolphthalein has been used to determine if the carbonation is complete since phenolphthalein (pink color) becomes colorless when pH drops below 8.3[20]. The

`

carbonation process results in the decrease of the porosity because $CaCO_3$ (calcite, 36.9 cc/mol) occupies more space (larger volume) than Portlandite (33.1 cc/mol)[37]. Furthermore, calcite has a higher density than Portlandite[39] so cement paste undergoes an increase in mass with carbonation. Permeability of the cement is reported to decrease by carbonation due to blockage of macropores[40], but the further flow of carbonic acid can remove the carbonated layer and cause the permeability to increase again.

It is reported that leaching, which takes place when cement is exposed to a pH less than 13, has an opposite effect on cement porosity as it causes porosity to increase[38]. In our study, both carbonation and leaching take place because of exposure to acidic brine. Figure 2.6 is showing the time effect on the microstructure. As the cement becomes older ongoing hydration results in further C-S-H formation and creation of gel pores (smaller than 0.01μm).

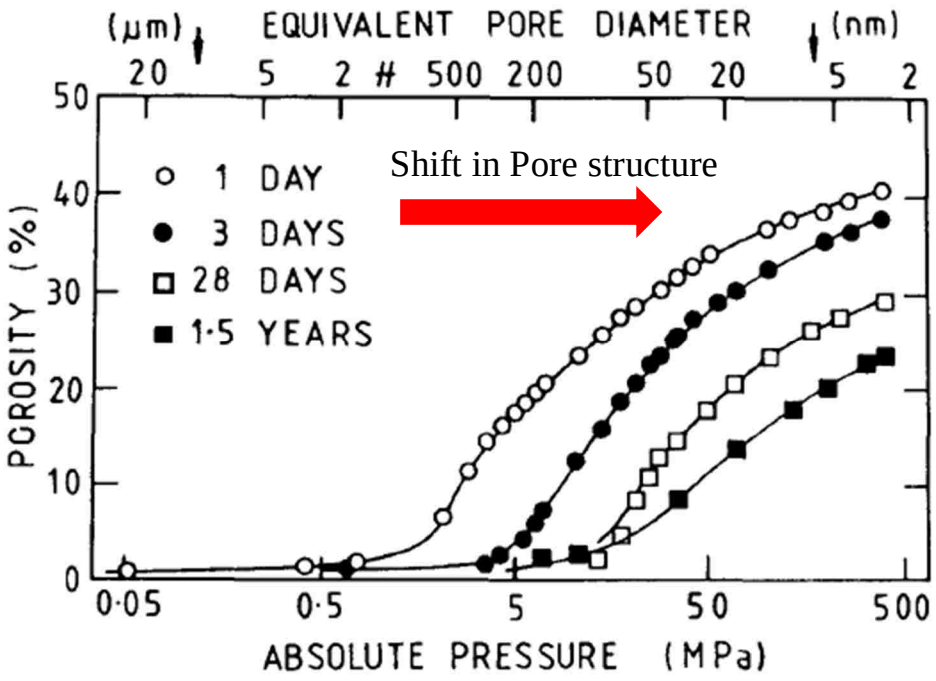

Figure 2.6: Time Effect on Microstructure of Hardened Cement

`

2.5 Experimental Studies and Field Data on Portland Cement-CO_2 Interaction

There are many well-documented studies in the literature which investigated the degradation phenomenon of Portland cement in CO_2 rich environments, some of which were also supported by field data.

Onan[41] investigated the effect of supercritical CO_2 on the samples prepared with different compositions (neat class-H cement and cement with pozzolan) under static conditions. Under low temperature and pressure (105 ^oF and 2,800 psi) partial carbonation was observed whereas high temperature and pressure testing conditions resulted in complete dissolution of Portlandite and C-S-H. No permeability change was noted from the tested conventional cements, but permeability increased for special systems.

Bruckdorfer[42] studied cement samples with exposure to CO_2-water. Experiments were conducted at 79.4 ^oC and 3,000 psi for 4-6 weeks. Strength loss was observed in the samples regardless of fly ash additions. Carbonation depths were measured and compared for the cement samples and fly ash addition was found to increase the carbonation depth. Under the constant pressure, increasing temperature resulted strength loss.

Duguid et al.[43] investigated the effect of carbonated brine on class-H cement. The authors used carbonic acid as permeant with pH of 2.4-3.7. They observed total removal of C-S-H and $Ca(OH)_2$ of cement in 31 days which lead to cement with no mechanical integrity.

Gouédard et al.[44] conducted an experimental study using class-G cement and they cured samples under ~ 3,002 psi and 90 ^oC. In their study, cement cores were submerged into brine solution so that the bottom part was exposed to CO_2 saturated brine and the top part exposed to supercritical CO_2 under ~ 4,061 psi and 90 ^oC. They extrapolated their data and estimated 100 mm alteration depth for 35 years of exposure. The alteration rates for CO_2 rich brine and

`

supercritical CO_2 are proportional to square root of time (defined by diffusion).

Kutchko et al.[45] carried out experiments using supercritical CO_2 and CO_2 saturated brine under static conditions with class-H cement. After curing the cement cores in 1% NaCl solution for 28 days, the cores were partially submerged in a solution so that the top portion of the core was exposed to supercritical CO_2, whereas, the bottom portion was exposed to CO_2 saturated brine. They analyzed the alteration depths in both sections with time and concluded that the alteration mechanisms are different. The alteration in the bottom part, which was exposed to CO_2 saturated brine, is similar to an acid attack and alteration rate is not constant due to $CaCO_3$ precipitation. The supercritical CO_2 attack was similar to an ordinary carbonation where the alteration rate is proportional to square root of time (defined by diffusion). After extrapolation, they concluded that 30 years of exposure to CO_2 rich brine would result in 1 mm of alteration depth in cement.

Huerta et al.[46,47] investigated the effect of HCl acidic solution on the behavior of fractures by employing confining stress cycles coupled with a set of flow through experiments using class-H cement. They cured their samples under 125 ^{o}F and atmospheric pressure. In their first set of experiments[46], they tried to establish a correlation between the confining stress and the fracture aperture using loading/unloading cycles. They observed elastic behavior, in which fracture apertures were returning to their same values after loading and unloading cycles without acid exposure. When exposed to a HCl solution (pH=0.3), they observed plastic behavior, in which the cement core was deformed permanently. In their second set of experiments[47], cement cores were fractured using the Brazilian method and immersed in a HCl solution (pH=3.5). The samples were treated with acid for 7 and 12 days to see the effect of acid exposure on cement. The cement core, which was exposed to acidic solution for 7 days, showed nearly elastic

`

behavior. However, the core, which was exposed for 12 days, showed plastic behavior. Fractures closed with increasing confining stress did not return to initial apertures with unloading cycles. They concluded that confining stress coupled with the acid exposure effect can close cement fractures and will prevent further flow.

Bachu and Bennion [48] carried out two sets of experiments with cores prepared using class-G cement to quantify the permeability changes with exposure to CO_2 saturated brine (saturated at ~2,198 psi and 65 ^oC) and supercritical CO_2. In the first set of experiments, the cement core was exposed to CO_2 saturated brine with ~ 2,198 psi pressure drop across the 3 cm core for 90 days under ~ 4,197 psi confining stress. In the second set of experiments, the cement-casing pair was exposed to supercritical ethane and $CaCl_2$ solution using ~ 1,998 psi pressure drop with perfect bond (0 cm annular gap) and 0.003, 0.0012 and 0.0018 cm annular gaps under a confining pressure of ~ 3,495 psi. Results of the first experiment showed that the permeability of the intact cement, 0.1μD (10^{-19} m^2), initially decreased to 0.01μD (10^{-20} m^2) then remained constant. The second set of experiments showed that the permeability of the cement-casing pair with a perfect bond was 0.001 μD (10^{-21} m^2) but existence of 0.01-0.3 mm microannulus and/or fractures inside the cement increased the permeability up to 1 mD (10^{-15} m^2). The authors concluded that the cement sheath, even after exposed to acid, has sufficient permeability for zonal isolation but existence of microannulus and/or cement fractures are the main conductive pathways for CO_2 leakage.

Brandvoll et al.[49] conducted static and flow-through experiments with cement samples (2.5 by 5 cm) which were prepared from class-G cement. The samples were cured for 28 days and the experimental conditions were 36 ^oC and 1,450 psi (100 bar) for both experiments. Static and flow through experiments were carried out using fluids with salinity of 16% and 3.5%

`

respectively. The static experiments were carried out with samples saturated with water and brine under 725 psi (50 bar) pressure supplied by CO_2 injection. Flow-through experiments were carried out under a confining pressure of 435 psi (30 bar) using flow rates values changing between 0.1 and 0.4 ml/min through a predrilled 1 mm radius channel. Static experiments show partial carbonation. Flow-through experiments resulted in consumption of Portlandite and C-S-H. Moreover, calcite/aragonite precipitation within channel and an increase in channel diameter was also observed. The effluent brine analysis confirmed that silica was leaching from the cement.

Wigand et al.[50] studied the effect of the brine and supercritical CO_2 on the shale-cement composite. The core holder containing shale-cement composite was held in the vertical position and fluid was injected from the bottom. Cement was fractured with the help of a hammer and chisel but fracture dimensions were not known. A total of 26.47 ml brine and 88.3 ml supercritical CO_2 was flowed through cement-shale composite in 113 days. XRD and SEM were utilized to characterize the mineralogical and microscopic changes. Two distinct zones were identified: a gray zone which still had Portlandite and calcite as the only carbonation product and an orange zone which contained different forms of $CaCO_3$ such as calcite and vaterite and amorphous material. They also observed both widening and closing (calcite filling) of the cement fractures. The resulting cement porosity (23.8%) is lower than its original value (37.8%) in the orange zone.

Carey at al.[51] investigated the effect of CO_2-brine flow on the microannulus simulated by the artificial channels, created between the cement and steel, as a casing. They prepared cement-casing composite in which steel was in the center of the cement (simulating the casing-cement system). A mixture of the supercritical CO_2 and brine was flowed through limestone and cement-

`

casing composite using ~ 2,030 psi injection and ~ 4,060 psi confining pressure with 0.333 ml/min and 0.1665 ml/min (used in last 5 days) for ~17 days. Limestone was placed ahead of the cement-casing composite to equilibrate the pH of the fluid before passing through the cement-casing composite. Permeability increased from 0.52 D ($0.52x10^{-12}$ m^2) to 1.5 D ($1.5x10^{-12}$ m^2) during the experiments probably due to dissolution. There were two zones: an orange zone was observed to contain $CaCO_3$ forms, and an unaltered zone contained Portlandite.

Two field studies are available in the literature to verify the experimental studies.

Carey et al.[52] investigated cement samples taken from a 55 year old well in SACROC field, a 30-year CO_2 EOR site located in West Texas. In this study, they observed alteration in wellbore cement exposed to CO_2. Casing and cement samples were taken from the shale caprock-cement and cement-casing interfaces. The casing samples did not show significant corrosion. The cement samples taken from the shale caprock-cement interface were orange in color. The cement sample taken from the casing-cement interface indicated carbonation with an orange coloration. Permeability of these cement samples was in the range of 0.1- 2 mD (10^{-16}-$2x10^{-15}$ m^2).

Crow et al.[53] analyzed the samples taken from a 30 year old natural CO_2 producer well (production casing was cemented with class-H cement and 50 % fly ash system), which did not show any sustained casing pressure history. Cement cores were taken from cement-rock and cement-casing interface. Formation fluid samples were found to have pH values of 5.2-6.1. Higher values of permeability (21 μD/$21x10^{-18}$ m^2) and porosity (41 %) were observed in samples taken closer to the CO_2 reservoir than the samples (1 μD and 25 % porosity) taken near the cement-caprock interface. A vertical interference test (VIT) was run to understand whether communication existed between the lower and upper perforations by pressuring and measuring the pressure pulses across the perforations. After numerical modeling of VIT data, the overall

`

permeability of the wellbore system (cement interfaces and casing) was computed as 0.01 D (10^{-14} m^2); whereas, the permeability of the cement core taken from the same depths was 1μD (10^{-18} m^2). This field data shows that the permeability of the cement-casing system is greater than the cement itself implying that there some artifacts (microfractures and/or microannulus) exist in the wellbore system.

2.5.1 Comparison of Experimental Studies and Field Data

Wellbore cement samples taken from wells exposed to CO_2 showed degradation to some degree, but they still provide a barrier by having a low permeability[52,53]. Existing field data suggests that intact cement sheath is not the primary concern for leakage from abandoned oil and gas wells. Instead, the microannulus between cement-casing and/or casing-formation interface and/or microfractures within cement sheath are the primary concerns for possible leakage. Moreover, interaction of these conduits, coupled with the effect of CO_2-brine mixtures, is not well understood. The behavior of interaction between the defects and the CO_2-brine mixtures will motivate our study. For the above reasons, the following experiments were designed to observe the interaction between the flowing CO_2 saturated brine and the cement fracture coupled with the confining stress applied to cement core.

2.6 Modeling Single Phase Flow through Single Fractures

2.6.1 Parallel Plate Approach

The study of naturally occurring fractures can be found in the petroleum literature, water resources research and rock mechanics literature. Fractures are important in Petroleum Engineering since they enhance the permeability of the reservoir system to a large extent (permeability of the fracture is equal to the square of the aperture). Underground water flows through fractures needs to be investigated for managing the available water resources. Fractures

`

are also important elements in rock mechanics since their mechanical behavior under stress is essential for solving rock mechanics problems. Fractures are characterized by the following properties; fracture aperture, width, length and roughness[54], as presented in Figure 2.7. Aperture (b) is the vertical distance between two fracture walls. Fracture width (w) is defined as the longitude of the fracture walls. Usually, roughness is expressed in terms of absolute roughness (e/b) which is basically the ratio of the height of the irregularities to the aperture (smooth surfaces have e/b equal to 0)[54].

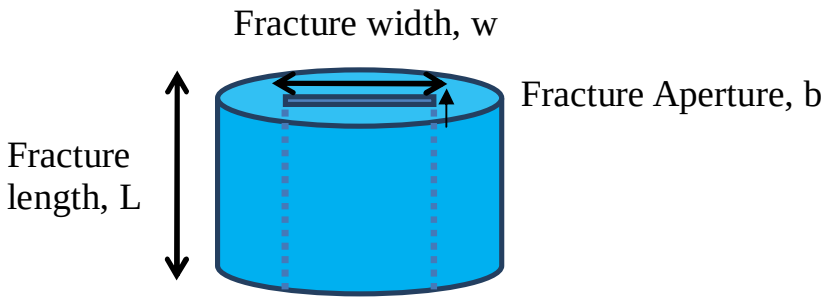

Figure 2.7: Schematic of Single Fracture

The first research about single fractures was carried out by Lomize[54] in 1951. He used parallel glass plates in his experiments. He assumed the fracture walls are smooth, parallel plates and that separation between these parallel plates are constant. Based on his experiments, he found that the flow rate passing through the fracture is proportional to the cube of aperture. He also developed correlations to predict the friction factors with different roughness ratios with laminar or turbulent flow. In reality, since aperture sizes are not the same at each point, many researchers use different definitions of aperture such as arithmetic and geometric average of local apertures.

`

2.6.2 Navier-Stokes and Stokes Equations

The motion of an incompressible fluid can be described by the "Navier-Stokes" equation[55].

$$\rho(u.\nabla)u + \rho\frac{du}{dt} = \mu\nabla^2 u - \nabla p - \rho g \quad \text{..... (21)}$$

where u is velocity, g is gravitational constant, ρ is density, μ is viscosity and ∇p is pressure difference. Assuming steady-state flow, acceleration can be neglected. If inertial forces are assumed to be small, the ρg term can also be neglected. The advective term causes this equation to be nonlinear. If the advective term is excluded, a very simple equation is obtained called "Stokes" equation.

$$\mu\nabla^2 u = \nabla p \quad \text{..... (22)}$$

Equation 22 can be used to model single phase fluid flow in single fractures [55].

2.6.3 Cubic Law

Witherspoon et al.[56] investigated the validity of the cubic law by conducting set of experiments. It is called the cubic law since flow rate depends on the cube of the aperture, "b". Using pressure drop (psi), fracture width (ft), fracture length (in), flow rate (bbl/day) and viscosity (cp) of the fluid, fracture aperture can be calculated. Equation 23 was originating from Equation 22.

$$Q = 5.11 \times 10^6 \left[\frac{w \times \Delta p \times b^3}{l \times \mu}\right] \quad \text{..... (23)}$$

Assumptions[56]:

- Parallel plates
- Smooth walls

In order to be able to use cubic law, one has to assume that flow is occurring between parallel-plates and smooth walls. Also, flow should satisfy laminar (N_{Re}<1150), steady-state

`

(dP/dt=0) and isothermal (T=constant) conditions[55,57]. Reynolds number is the ratio of the inertial forces to the viscous forces.

$$N_{Re} = \frac{928\ \rho\ v\ D}{\mu} \quad \text{.....(24)}$$

where, ρ is density (ppg or lb/gal), v is velocity (ft/sec), D is diameter (in) and μ is viscosity (cp).

2.6.4 Modifications to Cubic Law

Jones et al.[58] modified the cubic law equation (Equation 23) in order to account for the roughness effect which is given as Equation 27. It includes friction factor[59] which can be found using either Equation 25 or 26 depending on the flow regime (laminar or turbulent). According to de Marsily[57] the transition from laminar flow to turbulent flow takes place when Reynolds number (N_{Re}) exceeds 1150. Note that if f_f is equal to $96/N_{Re}$, the cubic law is obtained.

For laminar flow[59], $f_f = \left({}^{96}/_{N_{Re}}\right)\left(1 + 3.1 \times \left({}^{e}/_{b}\right)^{1.5}\right)$ .....(25)

For turbulent flow[59], $ {}^{1}/_{f_f{}^{0.5}} = 1 + 2\log 3.8\left({}^{b}/_{e}\right)$ ..... (26)

Modified cubic law[58], $Q = 5.06 \times 10^{4} \times w\left[\frac{\Delta p \times b^{3}}{f_f \times l \times \rho}\right]^{0.5}$ ..... (27)

2.6.5 Comparison of Cubic Law Based Models

Cubic law based models employ different hydraulic aperture definitions such that some models use the geometric mean of the all measured apertures and some models use the arithmetic mean of measured apertures for the hydraulic aperture. Also, some of the models integrate the effect of the contact area, roughness and tortuosity. Roughness is used for calculating the friction factors.

`

Konzuk et al.[60] presented a detailed experimental study comparing all the cubic law based models. In their study apertures were initially measured and the observed and calculated flow rates were compared. According to their results if Reynolds number is smaller than 1, calculated and observed flow rates are very close when one uses the geometric mean of the measured apertures or incorporates the roughness factor.

2.6.6 Aperture Measurements

Fracture aperture can be measured with various methods such as CT and resin impregnation method.

Hakami et al.[61] filled the fracture, within a granite core, with epoxy resin while applying confining stress. Then, the core (19 cm by 41 cm) was cut into pieces, cast into concrete and cut along the fracture and several images were taken along the core using stereo-microscope. Since the fracture is filled with epoxy, it was easily differentiated from the rock matrix and fracture aperture was measured.

Konzuk et al.[60] used the same technique, but they also mixed the resin with red dye in order to differentiate the rock and the fracture easily. This method creates a disadvantage that fractures filled with resin cannot be used for the next flow through experiments.

Keller[62] used X-Ray Tomography (CT) to measure fracture apertures while the core is kept inside the core holder. He used CT to measure apertures for a single fracture in granite core, sandstone core and multi fractures for a granite core. CT enables us to differentiate between the low and high mass regions by different levels of brightness. For this technique, in order to measure apertures, initially a calibration map should be set-up. A calibration map is prepared by scanning feeler gauges with known thicknesses placed inside between two flat surfaces so that aperture is known beforehand. After having the CT for the fracture with known aperture, the CT

`

signals can be correlated with the apertures. The correlation was used to convert CT signals into equivalent apertures. According to his results, fracture apertures along the core followed log-normal distribution.

2.6.7 Roughness Measurements

Although the parallel plate approach and cubic law assumes the walls of the fracture are smooth, in reality fracture surfaces are rough. A surface profiler can be used to determine the roughness by generating a topography map of the fracture surfaces[60].

Fractures can be studied accurately by utilizing aperture and roughness measurements and using a better defined cubic law, as presented above. Since these techniques were not available, a simple cubic law (Equation 23) will be used to infer the fracture apertures.

`

CHAPTER 3

EXPERIMENTAL SET-UP AND PROCEDURE

3.1 Cement Sample Preparation

Cement cores were prepared from a class-H cement slurry (w/c=0.38) according to API Recommended Practice for Testing Oil Well Cements, API RP-10B[19]. 327 grams of water and 860 grams of cement were mixed to prepare 600 ml of class-H slurry. After mixing the cement and water in required proportions at 4,000 RPM for 15 seconds and at 12,000 RPM for 35 seconds using a Hamilton Beach mixer, a vacuum pump was used to degas the cement slurry. After degassing, the cement slurry was poured into custom made molds (1 in by 13 in) as shown in the Figure 3.1. The wait on cement (WOC) period was 20 hours after pouring the slurry into molds. This optimum time was found by trial and error. After demolding the hardened cement, cement cores were cured in tap water for 4 to 6 months periods to allow time for the cement to complete its hydration (cement completes 70 % of its hydration in 28 days[18]). In the case of an existing irregular surface, the cement halves (Figure 3.2) were polished with sand paper to obtain smooth surfaces as much as possible. Two halves of cement (Figure 3.2) were put together using epoxy before starting the experiment, and the resulting core (1 in by 12 in) is shown in Figure 3.3. Fracture width reduced to 0.6 due to epoxy between the cement halves.

Figure 3.1: Cement Preparation Mold

`

Figure 3.2: Cement Halves

Figure 3.3: Cement Core (1 in by 12 in)

3.2 Experimental Fluids

A CO_2 saturated brine solution is used for all experiments. Brine is prepared with distilled water to ensure that unknown species are not present in the solution. The brine composition was originally designed to simulate West Texas formation fluids. This original brine contained Mg and $CaCO_3$ in minor amounts. The composition was then simplified to include only NaCl and KCl. As seen in the Table 3.1, the brine solution contained ~ 2% dissolved solids. After mixing water and salts, brine was filtered using filter papers to eliminate undissolved solid particles that can plug the flow lines in the experimental set-up. A filter was also installed upstream of the core to reduce the risk of plugging the flow lines. An accumulator (volume ~25 l) was used to accommodate the brine solution. CO_2 was bubbled through the accumulator at 15 psi resulting in a pH of 4.0. This method was selected instead of simultaneously flowing brine and CO_2, to prevent the possibility of multiphase flow through the cement fracture. However, the pump manufacturer did not recommend any pH value lower than 4.5. Therefore, fresh brine was mixed

`

with acidic brine to obtain pH values around 4.9-5.2 (in order to remain within manufacturer`s specifications) measured with an Oakton Waterproof pH Tester 10 which was also used to measure the effluent pH values throughout the experiments. The digital pH meter was calibrated with standard buffer solutions (pH=4, 7, 10) each week.

Table 3.1: Brine Composition

Chemical Reagents	Molecular Weight	Amount added to 1 l of Distilled Water	Molality (mol/kg)
Sodium Chloride (NaCl)	58.45 g/mol	20.196 g	0.3455 m
Potassium Chloride (KCl)	74.6 g/mol	0.345 g	0.0046 m

Table 3.2: Dissolved Solids in Brine Solution

Ions	Na^+	Cl^-	K^+
Concentrations	7,944 mg/l- 0.3455 m (mol/kg)	12,413.9 mg/l- 0.3502 m (mol/kg)	180.8 mg/l- 0.0046 m (mol/kg)

3.3 Experimental Set-up

The experimental set-up consisted of a Hassler type core holder (cell), syringe pump, hydraulic pump, back pressure regulator (BPR), cone shaped accumulator, pressure transducers, pressure gauges, data acquisition system and filter to prevent solid particles (larger than 50 μm) from flowing into the Hassler cell. A schematic of the experimental set-up is shown in Figure 3.4. The Hassler cell was mounted vertically on a stand position to mimic the upward flow of CO_2 saturated brine through the fractured vertical wellbore cement column.

`

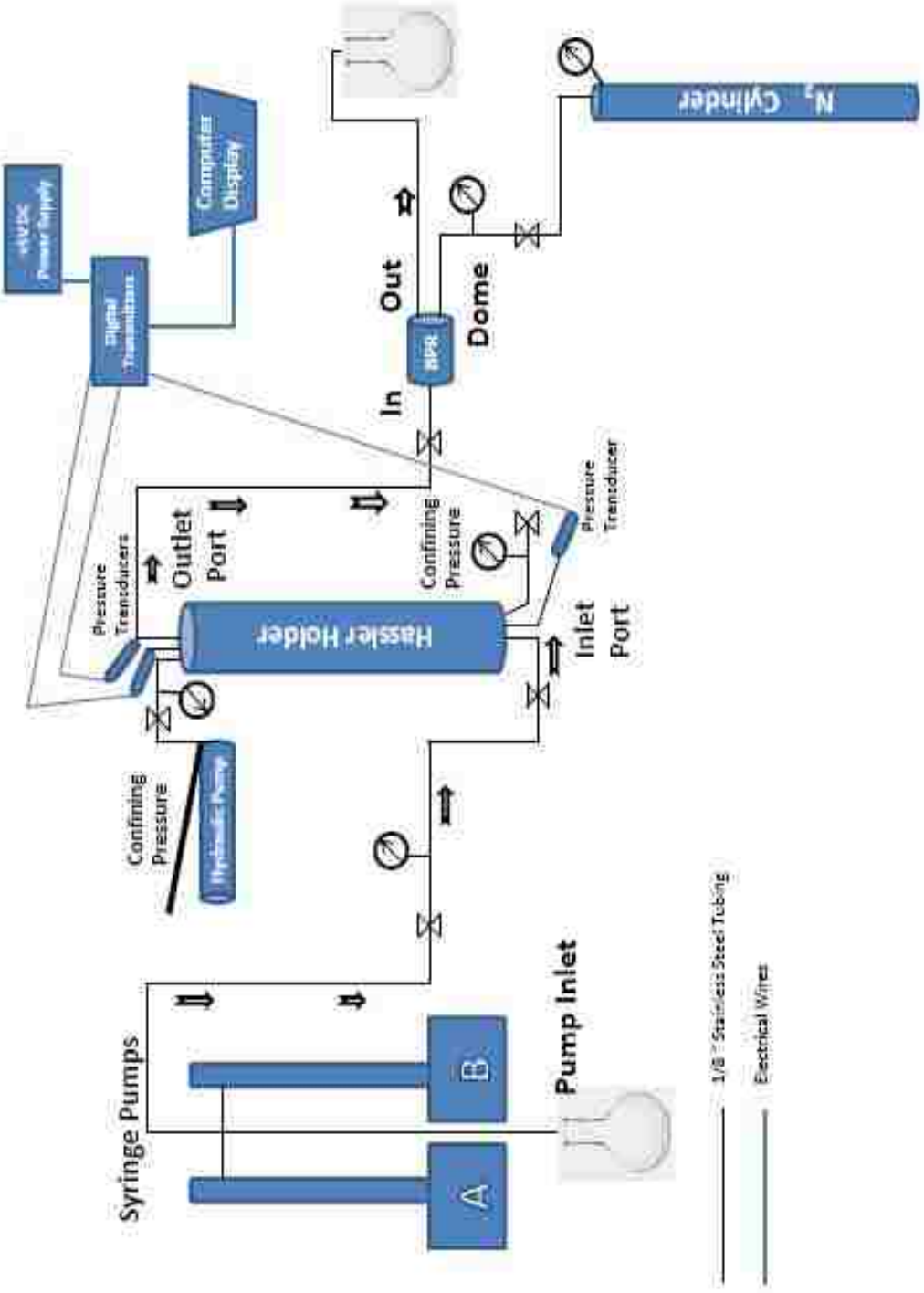

Figure 3.4: Schematic of Experimental Set-up

`

3.3.1 Syringe Pump

A Teledyne Isco E500 model syringe pump system capable of providing flow rates from 0.001 ml/min to 207 ml/min was used in this study. The pump can produce pressures up to 3,750 psi. It consists of two individual pumps (pump A and B), with 507 ml capacity each, which can be operated in independent pump mode as well as in continuous flow mode by the electronic controller. The lowest pH of 4 was recommended to prevent the corrosion of the pump. Pump A was used during the experiments in auto refill mode to provide continuous flow. It requires ~2.5 minutes to be refilled at a refill rate of 200 ml/min. Hence, CO_2 saturated brine was continuously pumped during 24 hours except the refills (total refill time is approximately 15 minutes per day).

Figure 3.5: Teledyne Isco Syringe Pump

3.3.2 Hassler Type Core Holder

The Hassler cell was manufactured by Temco-Tulsa, OK. It can accommodate cores up to 1 in diameter and 12 in length. The core holder has a Viton rubber sleeve. There are six pressure

`

taps along the sleeve with 2 inch spacing. The rubber sleeve requires at least 500 psi net overburden to seal the annulus of the core holder from the core sample. In order to prevent the entry of the confining fluid, the rubber sleeve is clamped to the fixed distribution plug. The first pressure tap and last pressure tap are located 1 in from the core inlet and outlet, respectively. The holder can withstand 3,750 psi of injection and confining pressure. Confining stress is applied to the rubber sleeve containing the cement core ensuring that linear flow occurs only through the cement fracture preventing the radial flow.

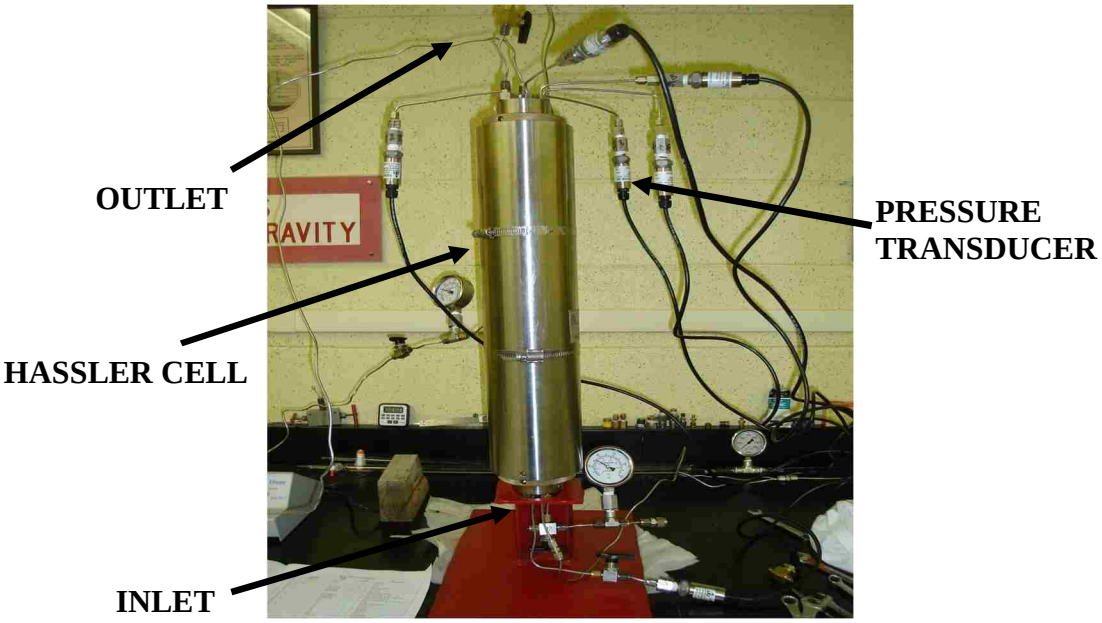

Figure 3.6: Hassler Type Core Holder

3.3.3 Data Acquisition System

Omega Pressure transducers were used to record the pressure drop data along the core and one transducer was used to record the inlet pressure at the core face. Two sets of transducers were used one for high pressure (0-5,000 psi) and the other for low pressure (0-50 psi) measurements. The transducers have a stated accuracy of 0.25% of the full pressure. Pressure transducers were then connected to six digital transmitters (Omega DIN-113) with electrical

`

wiring. Pressure transducers were calibrated directly with the pump which was calibrated by its manufacturer. Digital transmitters convert the voltage data, which is the output of the pressure transducers, to RS-232 signals. RS-232 signals were converted into RS-485 signals, which can be read by the computer. Afterward, the data is stored in the computer using a data logger program. The stable pressure drops were then selected and used to infer the fracture apertures.

3.3.4 Back Pressure Regulator (BPR) and Hydraulic Pump

A back pressure regulator (BPR), manufactured by Temco-Tulsa, OK, was used to achieve higher injection pressures. The BPR can accommodate flow rates up to 10 ml/min. Dome pressure was applied using Nitrogen (N_2). The upstream pressure (the pressure in the outlet) was adjusted to a value very close to the applied dome pressure (one to one ratio).

The hydraulic pump, manufactured by Enerpac, was used to exert confining stress on the cement core using hydraulic oil.

3.4 Experimental Program

The experiments were designed to see the effect of increasing injection pressure on the cement fracture. Therefore, injection pressure was the only different parameter. The 600 psi net overburden pressure ($P_{confining}$-$P_{injection}$) was maintained in the low and high pressure experiments. In Table 3.3, the experimental matrix is shown. Before starting the experiments, the system was tested using an unfractured cement core with water flow to see if the set-up provides an approximate permeability value (10^{-18}-10^{-20} m^2) for neat class-H cement.

Table 3.3: Experimental Matrix

Name	Curing	Back P.	$P_{Confining}$	$P_{Overburden}$	Q(ml/min)	Duration
Low P.	180 days-water	0 psi	600 psi	~ 600 psi	2	30 days
High P.	120 days-water	1,800 psi	2,400 psi	~ 600 psi	2	10 days

`

3.5 Material Characterization Techniques

Prior to and after the experiments, material characterization techniques were employed to gain insight into physical and mineralogical alterations inside the cement internal structure.

3.5.1 X-Ray Computed Tomography (Low Resolution CT)

X-Ray computed tomography, also known as CT, is a non-destructive technique[62,63] which utilizes rotating X-ray source around the sample to build the CT image. It was first used for medical applications, but was adapted later for petroleum engineering applications[63]. CT-scanning enables a quick determination of the core sections where dissolution/precipitation occurred. In fractured core samples, it provides information about the fracture geometry. Unreacted and reacted cement cores used in the low and high pressure experiments were scanned in Weatherford Laboratories using a Picker PQ5000 4th generation CT-scanner with a spatial resolution of 0.25 mm (250 μm) at an energy level 140 keV for quick determination of dissolved sections. The cement core was scanned inside the rubber sleeve first but the stainless steel pressure taps adversely affected the scanning process. Cement cores were later scanned without the rubber sleeve[64]. X-Ray Computed Tomography was also used to measure the distance between the fracture walls prior and post to acidic brine exposure in order to determine the widening or closing of the fracture.

3.5.2 Micro-CT (High Resolution CT)

Micro-CT is becoming a common tool used for porosity modeling[65]. The reacted and unreacted cement mini-cores (3 mm by 5 mm) were drilled in the Rock Preparation Laboratory in the Geology and Geophysics Department at LSU using a drill press. The Center for Advanced Microstructures and Devices (CAMD) was utilized and images were taken using 2.5 μm resolution and 34 keV monochromatic energy. Imaging the height of 1 mm lasted about 1 hour

`

and sequential heights were reconstructed with 0.5 degree spacing. The resulting files for 1 mm height were around ~ 1 GB (giga-byte) and combining images for 5 mm height was ~3.8 GB. The large size images were cropped using Avizo sofware in the Visualization Center located in Middleton Library, LSU to obtain images in the order of ~1 GB in size that can be handled in average computers.

3.5.3 Mercury Intrusion Porosimetry (MIP)

In MIP technique, mercury is injected into cement to understand the pore throat size distribution[35]. Cement samples require to be dried prior to MIP analysis to remove surface water. The injection pressure is gradually increased to be able to intrude even smaller pore throats with a lower limit of 0.001 μm. MIP assumes that all the pores are connected[66]. Besides its disadvantages, it is a quick technique that has been in application for many years; therefore, it was employed to see the effect of acidic brine on the pore throat size distribution.

3.5.4 Environmental Scanning Electron Microscopy (ESEM)

Portions of unreacted and reacted cement core samples were imaged using ESEM for microstructural characterization. ESEM was deployed to further investigate the nature of altered zones within the cement at a much finer scale and under low vacuum conditions in order to prevent cement dehydration during the analysis. The sections with higher atomic mass appear brighter. ESEM images were obtained using EDAX model electron microscope at Chevron ETC, Houston.

3.5.5 Energy Dispersive Spectroscopy (EDS)

EDS is a spot analysis that can be used while using ESEM. It detects the chemicals that are present in section of interest. When it is used on a low magnification image, it also detects chemicals surrounding the section of interest. This technique is a powerful tool to detect an

`

increase or reduction in Ca/Si that may be an indication of precipitation and dissolution.

3.5.6 X-Ray Diffraction (XRD)

XRD is a bulk analysis technique, used to determine the mineralogical content of a core sample, in which the section of interest is powdered and placed inside the X-Ray diffractometer. X-rays are emitted and rotated from 2 to 70 degrees at a step of 0.02 degree increments with Cu $K\alpha_1$ (copper) radiation. The X-ray source sends the signal and receives a response. Each mineral has a characteristic response. Computer software determines the type of mineral and outputs peak versus intensity plots for the minerals present in the core sample. Since XRD can only determine crystalline substances, the amorphous materials cannot be identified by XRD. XRD analyses were conducted on the control (unreacted) sample and reacted samples in the LSU Geology Department using a Siemens Kristalloflex D5000 X-Ray diffractometer.

3.5.7 Inductively Coupled Plasma-Optical Emission Spectroscopy (ICP-OES)

ICP-OES is a method which was conducted to determine Ca^{2+} content in the fluid. The fundamental characteristic of this process is that each element emits energy at specific wavelengths peculiar to its atomic character. By determining which wavelengths are emitted by a sample and their intensities, the analyst can determine the elements from the given sample relative to a reference standard qualitatively and quantitatively. The samples were analyzed in the LSU Department of School of Plant, Environmental and Soil Sciences using a Spectro $Ciros^{CCD}$ ICP-OES machine. During the experiments, effluent brine samples were monitored for pH and collected daily and samples were selected for ICP-OES analysis depending on pH values.

3.6 Image Based Porosity

After Micro-CT images were reconstructed and cropped to a smaller size image, the ImageJ[67] (National Institutes of Health, USA) software was utilized to determine the threshold values for

`

the images. Threshold values are selected from a 0-255 scale (8-bit image contains 2^8 = 256 colors). Using the Pelican high performance computer at LSU the gray scale images were converted into binary images (i.e. solid and void) using an indicator based kriging algorithm[68]. This process assigns zero to void spaces and one to matrix. The output images were then processed with ImageJ[67] software, and using the histogram tool, the percentage of void spaces (ratio of 0`s to the whole image) were obtained. The porosity obtained from Micro-CT gives an estimation about the macroporosity depending on the resolution (e.g. volume of the pores larger than 10 μm is identifiable when 5 μm resolution is used).

Figure 3.7 shows cross-sectional schematic of the 12 in cement core and sections prepared for the analytical techniques presented above. Fracture surface was directly in contact with acidic brine. Low Resolution CT was conducted on the entire core whereas small regions were cut apart for ESEM, Micro-CT and MIP techniques. Pictures of these sections are presented in Appendix A.

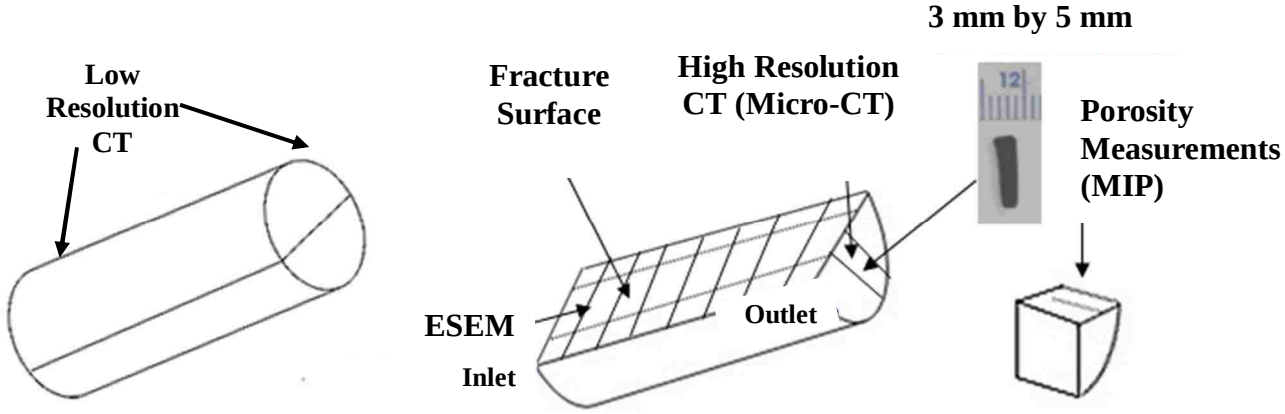

Figure 3.7: Locations of Samples Prepared for Different Analytical Techniques

`

3.7 Geochemical Analysis

The alkalinity values were determined using phenolphthalein and methyl orange solutions according to standard alkalinity measurement procedure[69]. This procedure involves adding 0.02 N H_2SO_4 (sulfuric acid) to reduce the pH to 8.3 and 4.3. The amount of acid used to reduce the pH to 8.3 (known as phenolphthalein end point, p_f) and 4.3 (known as methyl orange end point, m_f) are recorded. HCO_3^- and CO_3^{-2} concentrations are then calculated in mg/l according to Table 3.4. As seen from the table, carbonate is not detected when p_f is 0 or pH is below 8.3.

Table 3.4: Alkalinity Determination (OFITE Drilling Fluids Manual) [69]

$p_f = 0$	m_f x 1,220 = mg/l HCO_3^-	Bicarbonate only
$p_f = m_f$	p_f x 340 = mg/l OH^-	Hydroxide only
$2p_f < m_f$	$2p_f$ x 600 = mg/l CO_3^{-2} ($m_f - 2p_f$) x 1,220 = mg/l HCO_3^-	Carbonate Bicarbonate
$2p_f = m_f$	m_f x 600 = mg/l CO_3^{-2}	Carbonate only
$2p_f > m_f$	($2p_f - m_f$) x 340 = mg/l OH^- ($m_f - p_f$) x 1,200 = mg/l CO_3^{-2}	Hydroxide Carbonate

The standard procedure of alkalinity test presented above, was followed and used coupled with ICP analysis to decide whether the brine solution was oversaturated or undersaturated with calcite.

`

CHAPTER 4

RESULTS AND DISCUSSION

This chapter will report and discuss the results obtained from the low and high pressure experiments. In order to understand the microstructural alterations caused by the acidic brine, unreacted (control) cement cores were compared with reacted cores using analytical techniques described in Chapter 3.

4.1 X-Ray Computed Tomography (Low Resolution CT)

As an initial point for microcharacterization, low resolution CT images, shown in Figure 4.1, were taken at 8 different locations (8 axial slices) along the 12 in cement core prior to and after the low pressure experiment to nondestructively visualize the alterations due to acidic brine exposure. The locations of axial slices were the same in the unreacted and the reacted cores as they were recorded in the CT scanner`s memory. The light areas around the axial slices are caused by the beam hardening effect which is an artifact caused by absorption of X-Rays of certain energies prior to penetrating the sample[63]. The section between slice #1 and slice #2, section 1-2, is the outlet section -the last contact point with acidic brine. The section between slice #7 and slice #8, section 7-8, is the inlet section which is the first contact point with acidic brine. Sections 1-2 and 7-8 were dissected for further microcharacterization. Since X-Ray Computed Tomography is sensitive to sample density; regions having higher atomic mass appear brighter in CT images, and completely dark areas represent void spaces such as pores or fractures. The Ca^{2+}-depleted regions along the fracture walls are indicated by darker color, due to their lower atomic mass compared to the other sections within the axial slices.

Fracture apertures were measured using ImageJ[67], before and after exposure to CO_2 saturated brine, illustrated in Figure 4.2. As observed, Figure 4.2 reveals the dissolution along the fracture

`

walls, indicated with darker color, and widening of the fractures. Measurements were done at the center of the slices. Table 4.1 tabulates measured fracture apertures for the low pressure experiment. Fracture aperture became 26% wider in slice #1 (outlet) in the reacted cement core than in the unreacted cement core under unconfined stress conditions. The widening percentage appears to be the largest in slice #2 whereas the smallest increase occurred in slice #3. The average of these changes was 24.4 % and the standard deviation was 8.6%.

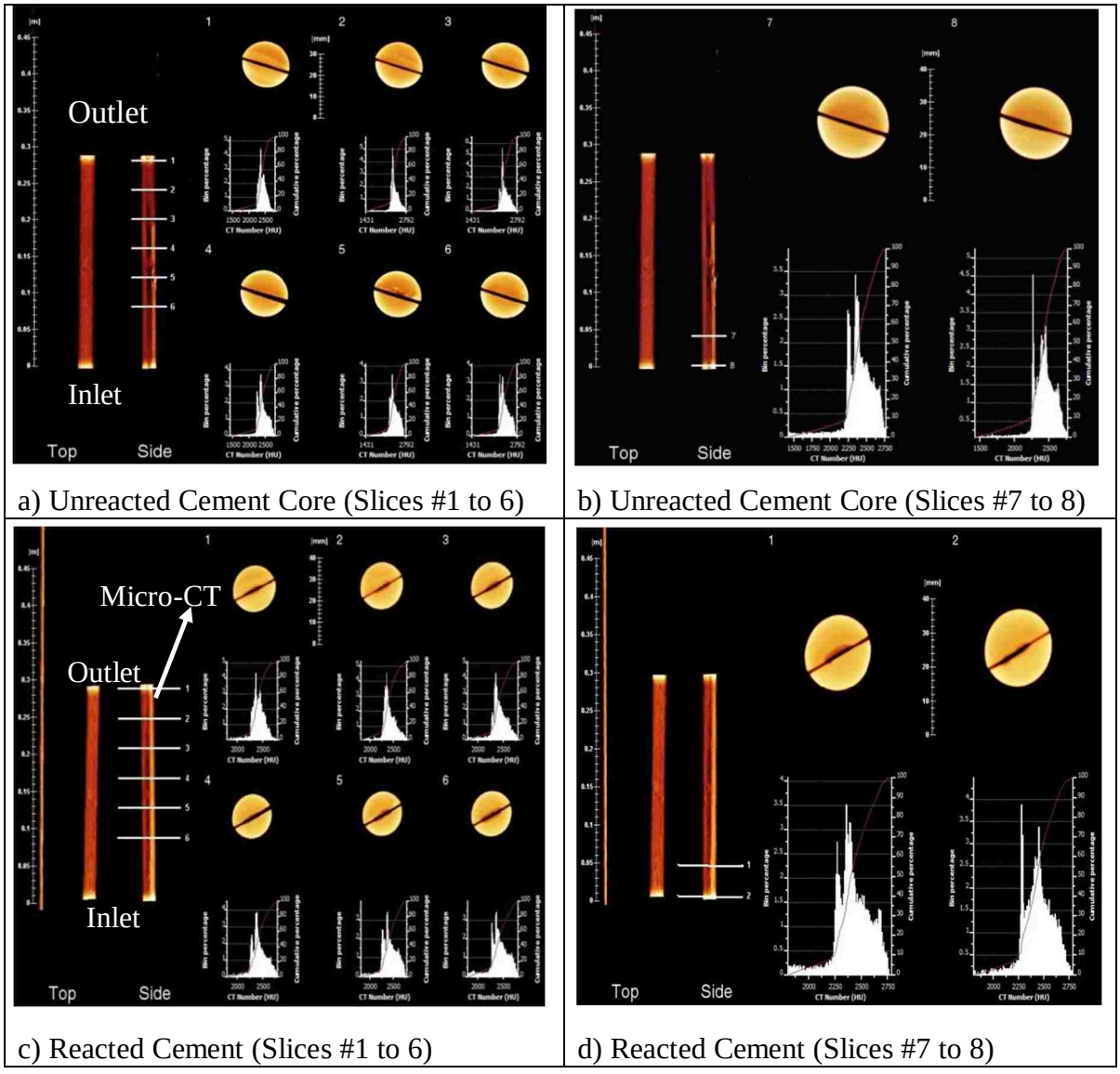

a) Unreacted Cement Core (Slices #1 to 6)

b) Unreacted Cement Core (Slices #7 to 8)

c) Reacted Cement (Slices #1 to 6)

d) Reacted Cement (Slices #7 to 8)

Figure 4.1: Low Resolution CT Images for Low Pressure Experiment

`

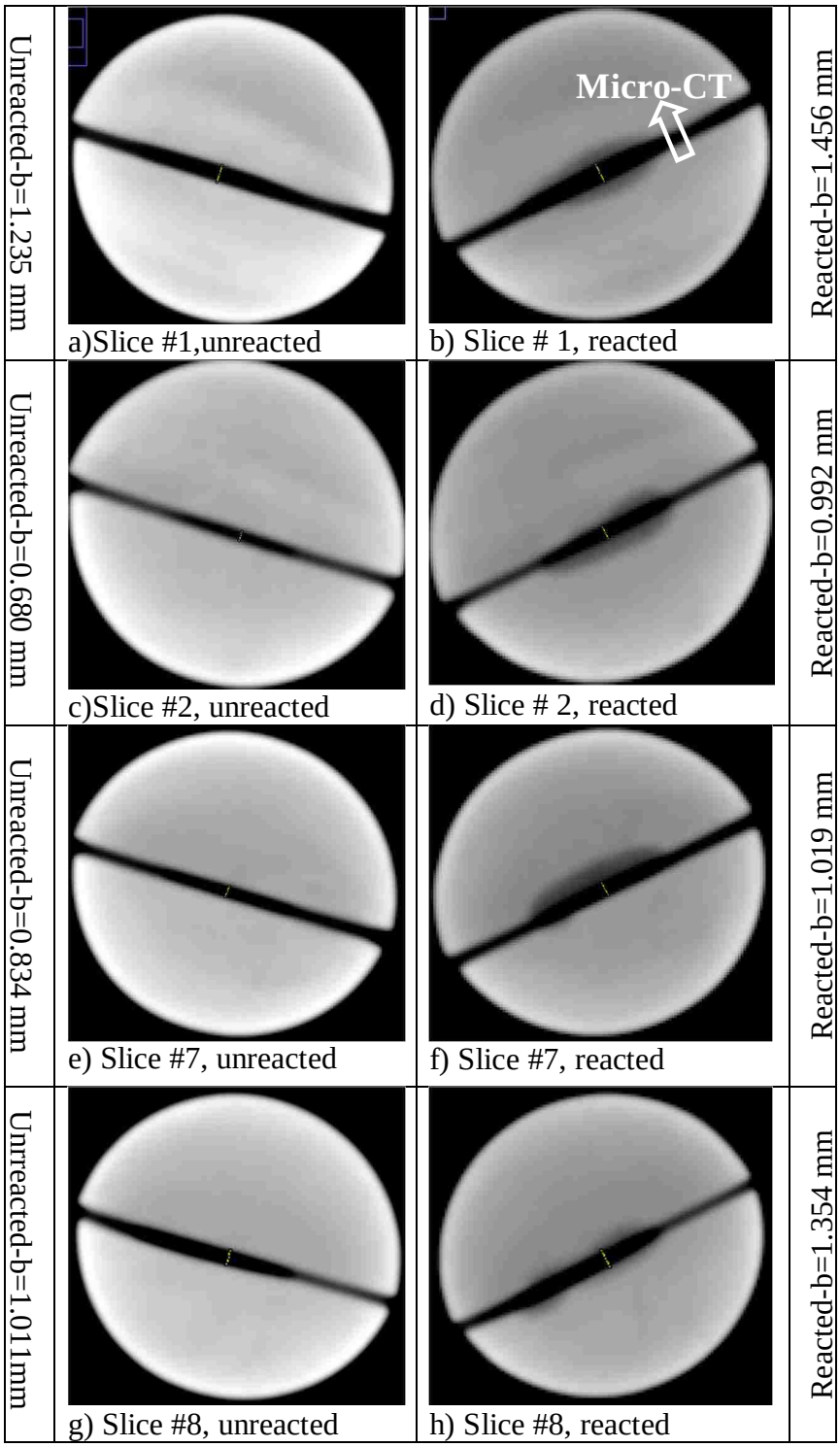

Figure 4.2: Widening of Fracture and Dissolution along the Fracture Walls in Parts b, d, f and h for Low Pressure Experiment

`

Table 4.1: Aperture Measurements Using Low Resolution CT for Low Pressure Experiment

Axial Slice #	Aperture, unreacted	Aperture, reacted	% Increase
1 (outlet)	0.71 mm	0.90 mm	26 %
2*	0.59 mm*	0.81 mm	35 %
3	0.97 mm	1.06 mm	9 %
4	1.15 mm	1.34 mm	16 %
5	1.05 mm	1.35 mm	28 %
6	0.85 mm	1.04 mm	21 %
7	0.72 mm	0.91 mm	26 %
8 (inlet)	0.79 mm	1.04 mm	31 %

(Fracture aperture indicated with * is low compared to other axial slices probably due to an erroneous measurements during CT scanning or an irregular fracture surface.)

Fracture widening was validated with aperture calculations using pressure drop data collected during the flow-through experiments. The cubic law (Equation 23, page 29) was used to calculate an average fracture aperture along the 12 in cement core. Parameters used to compute the fracture aperture,

Fracture Width (w) = 0.6 in = 0.05 ft Viscosity (μ) = 0.9 cp[34]

Fracture Length (L) = 12 in Flow Rate(Q) = 2 ml/min = 0.018 bbl/day

Results are shown in Table 4.2. Aperture calculations show that the fracture is widening by 2.2 µm or ~4% as a result of the 30 day acid brine flow. Fracture aperture decreased in the first 14 days of the experiment but increased to a larger value than the initial aperture.

Table 4.2: Aperture Calculations Using Cubic Law for Low Pressure Experiment

Number of Days	Average Pressure Drop	Aperture	% Change
0 (Unreacted)	5.6 psi	57.2 µm	-
1	5.6 psi	57.2 µm	0%
7	7 psi	53 µm	- 7.3%
14	8 psi	50.8 µm	-11.2%
21	5.2 psi	58.6 µm	+ 2.45%
28	4.9 psi	59.6 µm	+ 4.2%
30	5 psi	59.4 µm	+ 4%

`

Low resolution CT was not carried out for the high pressure experiment due to experimental problems. Therefore, identification of the samples was not possible for inlet and outlet sections. The samples analyzed from the high pressure experiment will be designated as reacted samples in the following sections.

4.2 Micro-CT (High Resolution CT) and Image Based Porosity

After scanning the 12 in core using low resolution CT, higher resolution analysis was conducted to evaluate alterations on a finer scale. The Micro-CT analytical tool is widely used for image based porosity characterization. In this study regions identified with low resolution CT images were used to determine locations where mini-cores were extracted for Micro-CT. The outlet region of the core in the low pressure experiment was selected for Micro-CT analyses.

4.2.1 Low Pressure Experiment

The mini-core for Micro-CT (3 mm by 5 mm) was drilled from the fracture surface into the core in the outlet section (indicated in Figure 4.1 and Figure 4.2). Micro-CT images were obtained at 2.5 μm resolution. The 5 mm height of the mini-core, extracted from the reacted outlet section was imaged. Micro-CT image of the unreacted (control) sample is shown in Figure 4.3 and porosity was found to be 0.25 % (Table 4.3) using a threshold value of 141. Figure 4.4 depicts the density change in the z-direction from fracture surface to the inner part of the core indicated with darker/brighter coloration. The transition zone from region I (fracture surface) to region II (inner part of the core) is identified and cross-sections are shown in Figure 4.5. Two subvolumes were extracted from the image volume—one in region I and one in region II. Once the two phases were identified (void and matrix) using simple thresholding with ImageJ[67], the porosity was calculated by calculating the volume fraction of the void phase. Threshold values used for Region I and Region II were 109 and 90 respectively. Porosity values were then found

`

to be 1.39 % and 0.45 % for subvolumes cropped from regions I and II, respectively for pores larger than 5 μm (Table 4.3). Porosity, defined as the volume fraction of void space that contains pores on the order of 5 μm or larger for image based porosity, seemed to increase in region I (the region in contact with acidic brine).

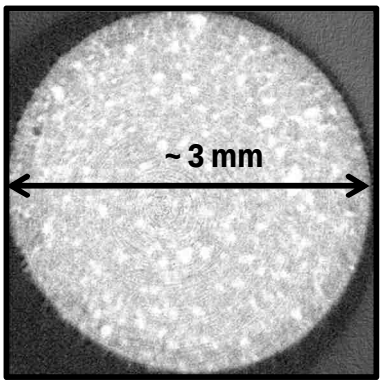

Figure 4.3: Micro-CT Image (axial slice #178) of Unreacted Core for Low Pressure Experiment

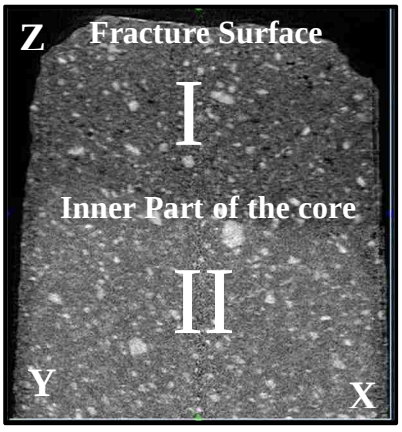

Figure 4.4: Cross-sectional View of Micro-CT Image (2.24 ×2.25 × 2.01 mm^3) along the Length of Mini-core for Low Pressure Experiment (outlet section)

`

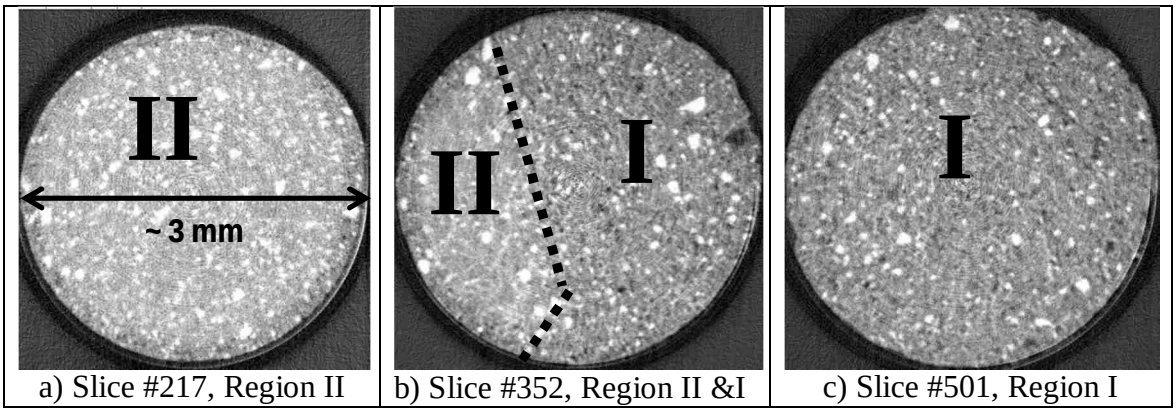

a) Slice #217, Region II | b) Slice #352, Region II &I | c) Slice #501, Region I

Figure 4.5: Micro-CT Image (axial slices) of Reacted Cores for Low Pressure Experiment (outlet section)

Table 4.3: Image Based Porosity for Low Pressure Experiment (outlet section)

Unreacted-Low Pressure	Reacted-Low Pressure	
Porosity	Porosity-Region I	Porosity-Region II
0.25 %	1.39 %	0.45 %

4.2.2 High Pressure Experiment

The resolution of 2.5 μm was also used to image mini-core for the high pressure experiment. Porosity was found to be 0.36% for the unreacted (control) sample, illustrated in Figure 4.6, using a threshold value of 140. A three mm height of reacted sample was imaged (Figure 4.7). Figure 4.8 shows similar brightness values, indicating a slight difference in the density in the high pressure experiment, across z-direction. There was no apparent transition observed from region I to II as opposed to the low pressure experiment. Porosity values were calculated for region I and II by utilizing the same procedure used for the low pressure experiment. Threshold values used for Region I and Region II were 120 and 134 respectively. Results of imaged based

`

porosity analysis are shown in Table 4.4. The high pressure experiment resulted in a smaller porosity increase when compared to the low pressure experiment.

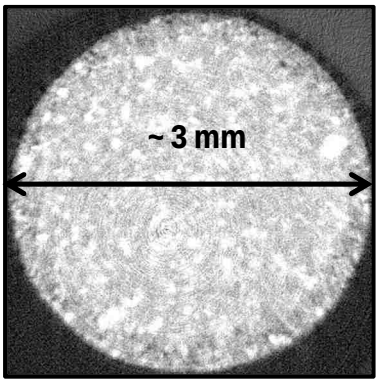

Figure 4.6: Micro-CT Image (axial slice #254) of Unreacted Core for High Pressure Experiment

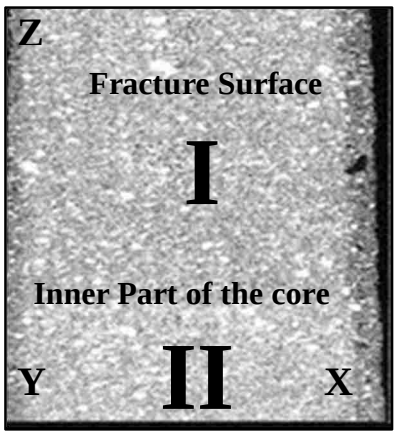

Figure 4.7: Cross-sectional View of Micro-CT Image (2.45 × 2.45 ×3.2 mm^3) along the Length of Mini-core for High Pressure Experiment

`

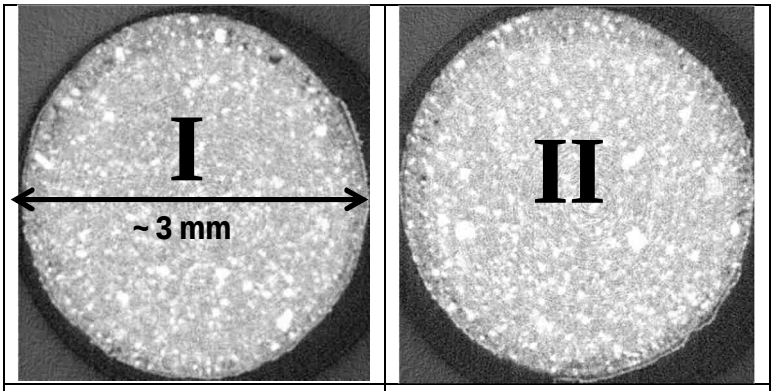

a) Slice #275, Region I | b) Slice #925, Region II

Figure 4.8: Micro-CT Image (axial slices) of Reacted Core for High Pressure Experiment

Table 4.4: Image Based Porosity for High Pressure Experiment

Unreacted-High Pressure	Reacted-High Pressure	
Porosity	Porosity-Region I	Porosity-Region II
0.36 %	0.45 %	0.41 %

When Figures 4.4 and 4.5 are compared with Figures 4.7 and 4.8, it can be observed that change in porosity was more evident in the low pressure experiment because of the distinct change in brightness with exposure to acidic brine.

4.3 Mercury Intrusion Porosimetry (MIP)

MIP raw data includes incremental intrusion (ml/g), cumulative intrusion (ml/g), capillary pressure (psi) and pore throat sizes (μm) in a tabulated format. Porosity (percent of sample volume) values were calculated for each pore throat size by dividing incremental intrusion values to the cumulative intrusion values. The summation of porosity values results in total (global) porosity.

`

4.3.1 Low Pressure Experiment

MIP standard provided the pore throat size distribution ranging from 0.0018-70 µm. This wide range of pore throats was further divided into four sub-intervals: 0.0018-0.1 µm, 0.1-0.5 µm, 0.5-5 µm and 5-70 µm as shown in Figures 4.9 to 4.12. The control sample is represented by Unreacted LP. Inlet and outlet sections of the cement core are denoted by Reacted LP_7-8 and Reacted LP_1-2 respectively. Porosity values were plotted against pore throat sizes.

Figure 4.9 suggests a reduction in the porosity between 0.01 µm and 0.04 µm (indicated with a circle) with acidic brine exposure. The porosity reduction is more pronounced in Reacted LP_1-2 (outlet) sample than Reacted LP_7-8 (inlet) sample. There is no change in porosity below 0.01 µm (10 nm).

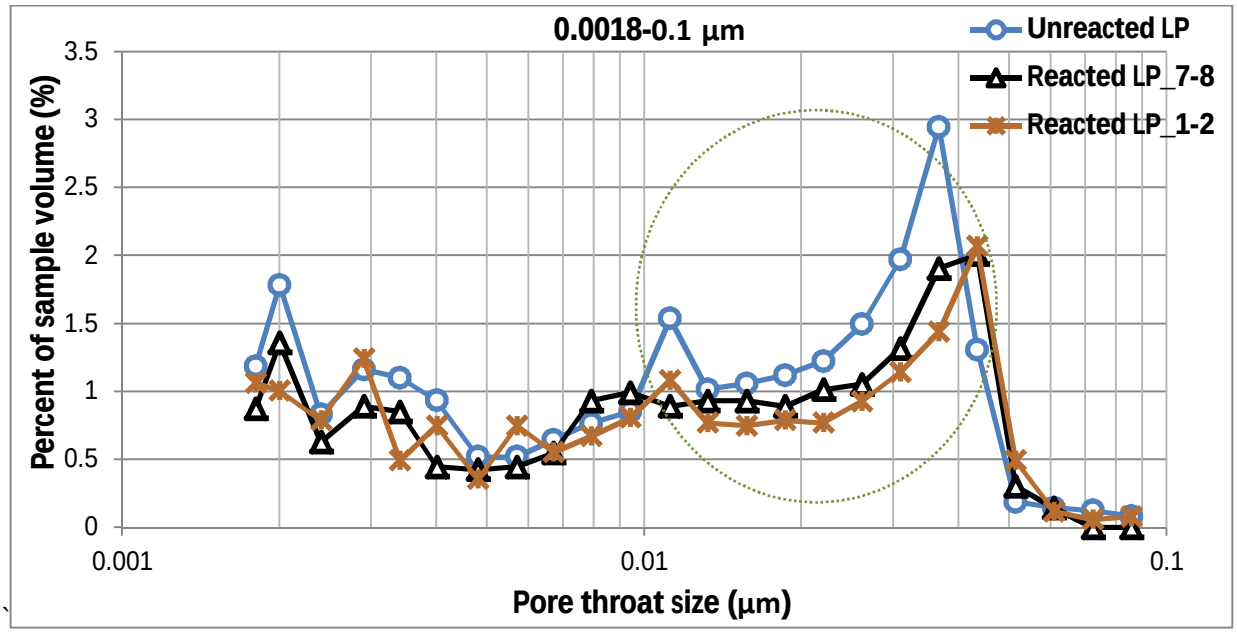

Figure 4.9: Pore Throat Size Distribution between 0.0018 µm and 0.1 µm for Low Pressure Experiment

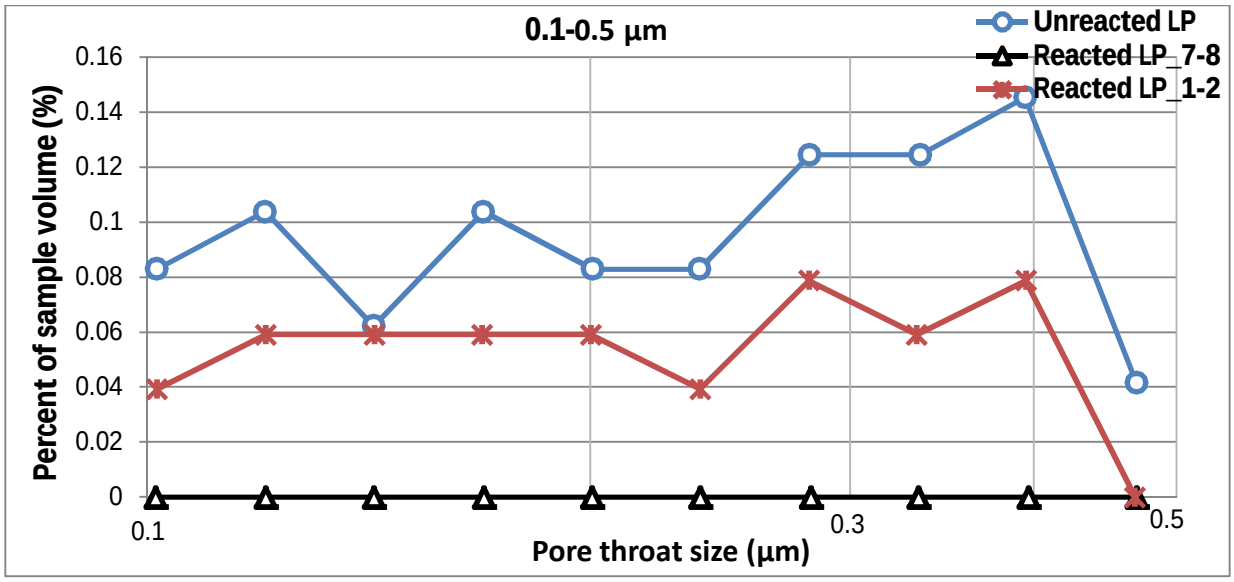

Figure 4.10: Pore Throat Size Distribution between 0.1 µm and 0.5 µm for Low Pressure Experiment

Pore throats between 0.1 µm and 0.5 µm are analyzed in Figure 4.10. Porosity was reduced with the acidic brine exposure. It is also observed that there were no pore throats between 0.1 µm and 0.5 µm in the Reacted LP_7-8 (inlet) sample. The Unreacted LP (control) sample had higher porosity than the Reacted LP_1-2 (outlet) sample except the pore throat size of 0.14 µm in which their porosity values are very similar.

Figure 4.11 shows the pore throat size distribution between 0.5 µm and 5 µm. For 3 µm pore throat size, the porosity was highest in the Unreacted LP (control) sample. The reacted LP_7-8 (inlet) sample had higher porosity than the Reacted LP_1-2 (outlet) sample. Interestingly, at a pore throat size of 3.55 µm, the Reacted LP_1-2 (inlet) sample had higher porosity than the Unreacted LP (control) and the Reacted LP_7-8 (outlet) samples. The porosity values were nearly identical around 4.5 µm.

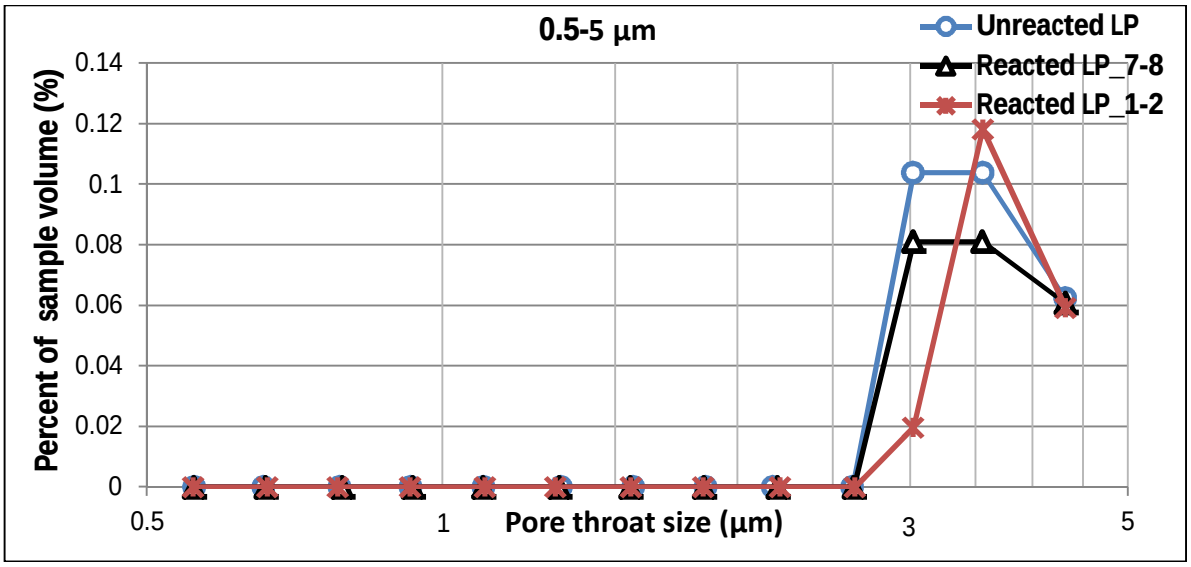

Figure 4.11: Pore Throat Size Distribution between 0.5 µm and 5 µm for Low Pressure Experiment

The pore throat size distribution of the 5-70 µm sub-interval is illustrated in Figure 4.12. MIP analysis suggested that there were no pore throats larger than 62 µm. The largest measured pore throat was 62 µm. There was an increase in the porosity between 32 µm and 62 µm which is easily distinguishable from the dotted region for the Reacted LP_1-2 (outlet) sample.

Figure 4.13 presents the pore throat size distribution between 0.0018 µm and 70 µm. The reduction in total porosity can be recognized from the dotted region where Unreacted LP (control) sample has the highest porosity. Smallest pore throats (0.0018 µm -0.1 µm) showed a reduction in porosity. Pore throats larger than 0.1 µm did not show a distinct separation between the control and reacted samples.

`

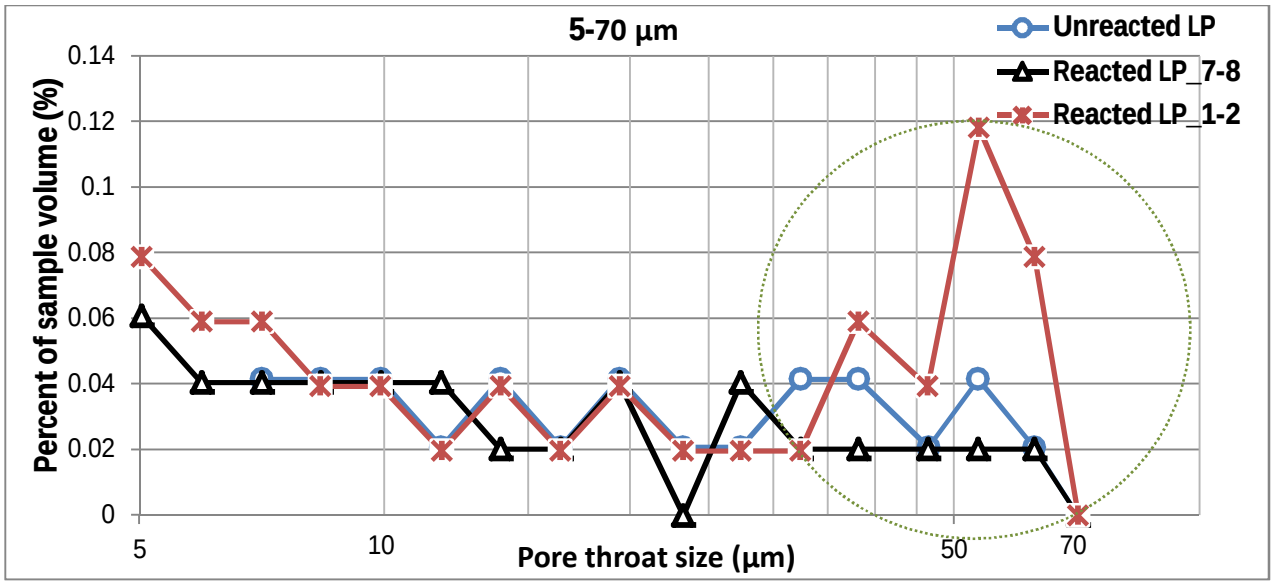

Figure 4.12: Pore Throat Size Distribution between 5 µm and 70 µm for Low Pressure Experiment

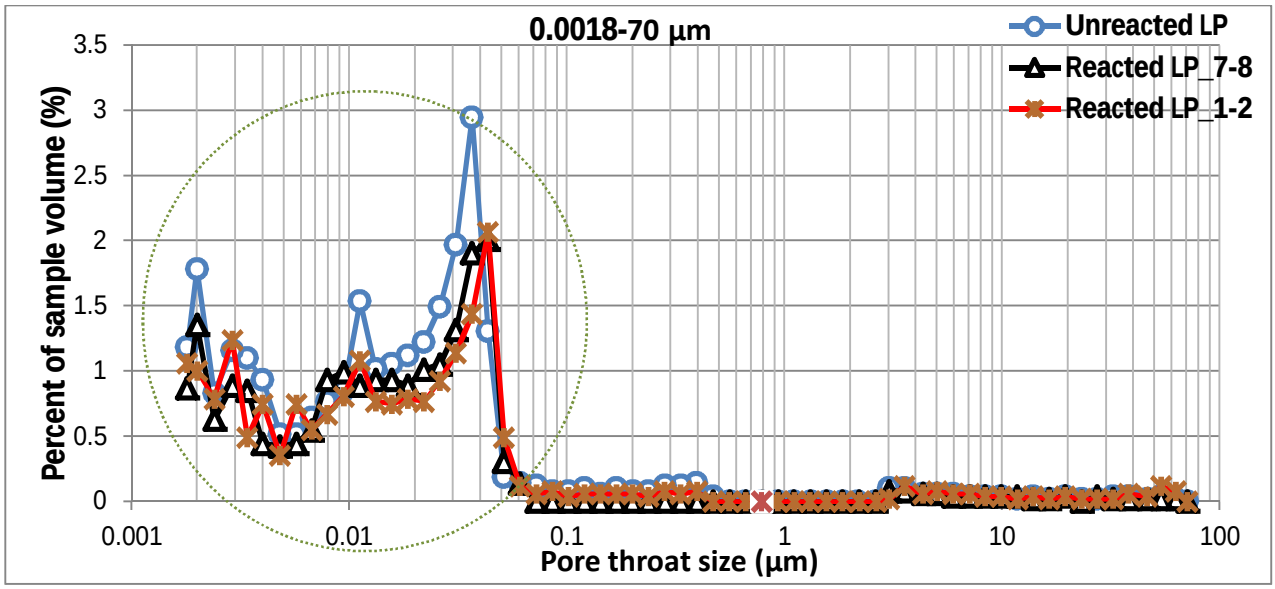

Figure 4.13: Pore Throat Size Distribution for Low Pressure Experiment between 0.0018 µm and 70 µm

4.3.2 High Pressure Experiment

Figure 4.14 shows that porosity diminished as a result of the high pressure experiment in the 0.0018-0.1 µm sub-interval. Although the porosity increased around 0.04 µm, porosity

`

associated with the pore throats smaller than 0.005 µm has reduced more therefore, overall porosity decreased in this sub-interval.

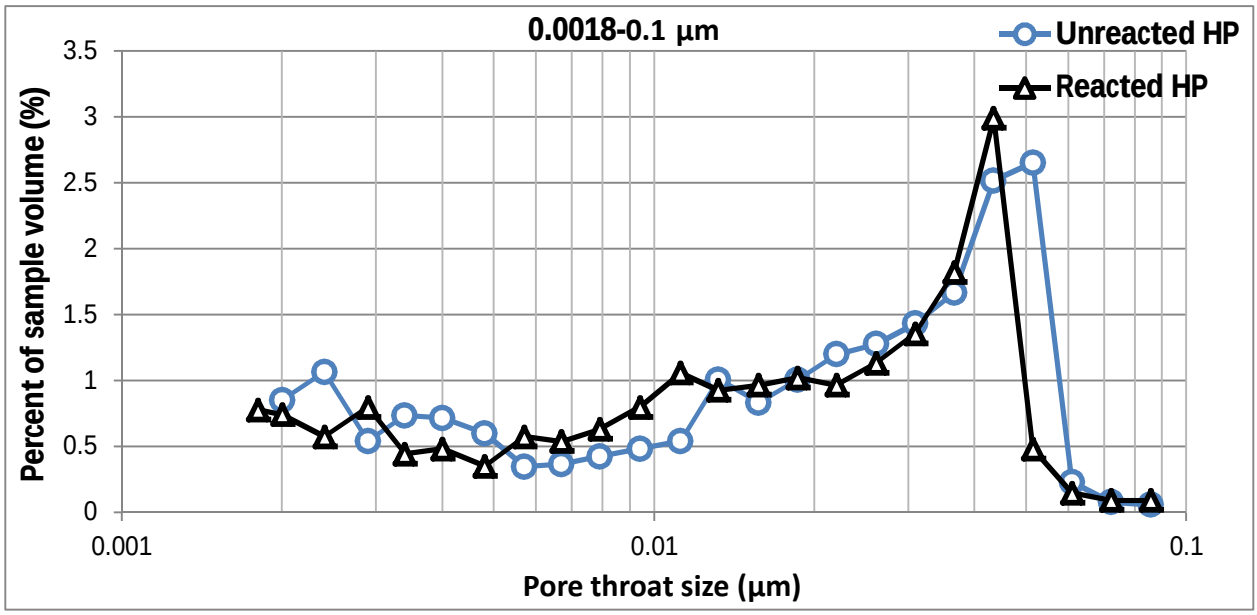

Figure 4.14: Pore Throat Size Distribution between 0.0018 µm and 0.1 µm for High Pressure Experiment

There was an obvious increase in porosity in the 0.1-0.5 µm sub-interval due to acidic brine exposure as shown in Figure 4.15. There were no pore throats, between 0.14 µm and 0.47 µm, present in the unreacted cement core. A pore range that was not observed in unreacted (control) sample seems to have developed.

Figure 4.16 presents pore throats between 0.5 µm and 5 µm. New pore throats became accessible to mercury and the trend of development of pore throats continued until 0.92 µm. There were no pore throats present in the unreacted (control) or reacted samples between 0.92 µm and 2.6 µm. Overall, porosity increased in this range.

`

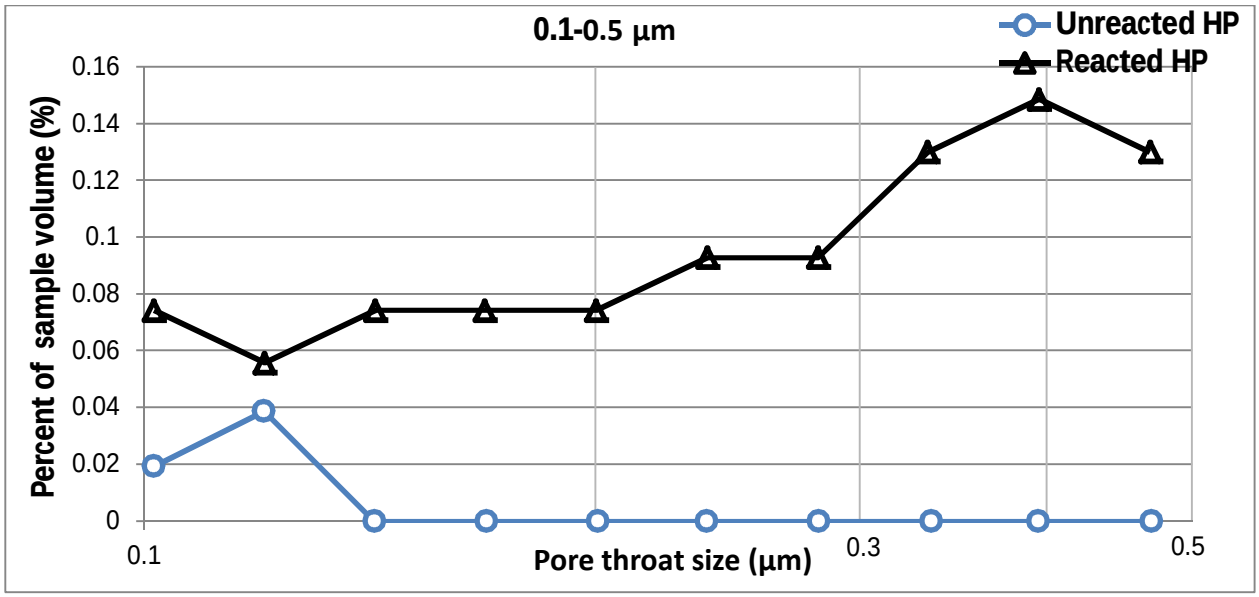

Figure 4.15: Pore Throat Size Distribution between 0.1 µm and 0.5 µm for High Pressure Experiment

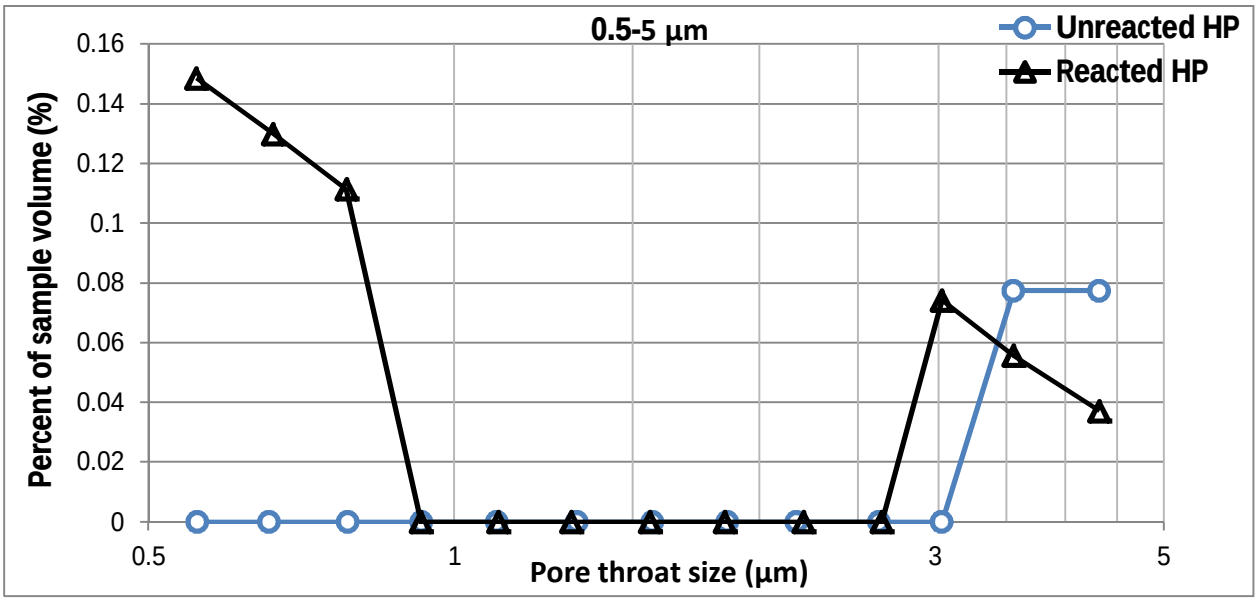

Figure 4.16: Pore Throat Size Distribution between 0.5 µm and 5 µm for High Pressure Experiment

The largest pore throats (5-70 µm) measured by MIP show a reduction in porosity as presented in Figure 4.17. The overall reduction in porosity was caused by a porosity decrease between 5 and 10 µm pore throats although porosity increased at 19 µm and 54 µm.

`

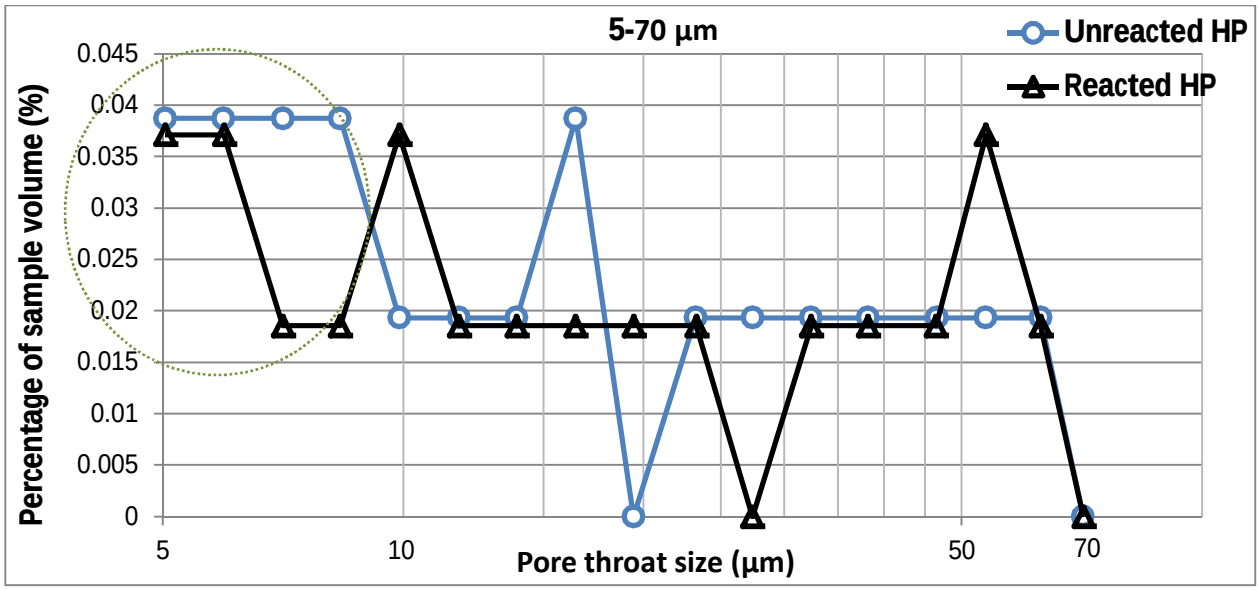

Figure 4.17: Pore Throat Size Distribution between 5 µm and 70 µm for High Pressure Experiment

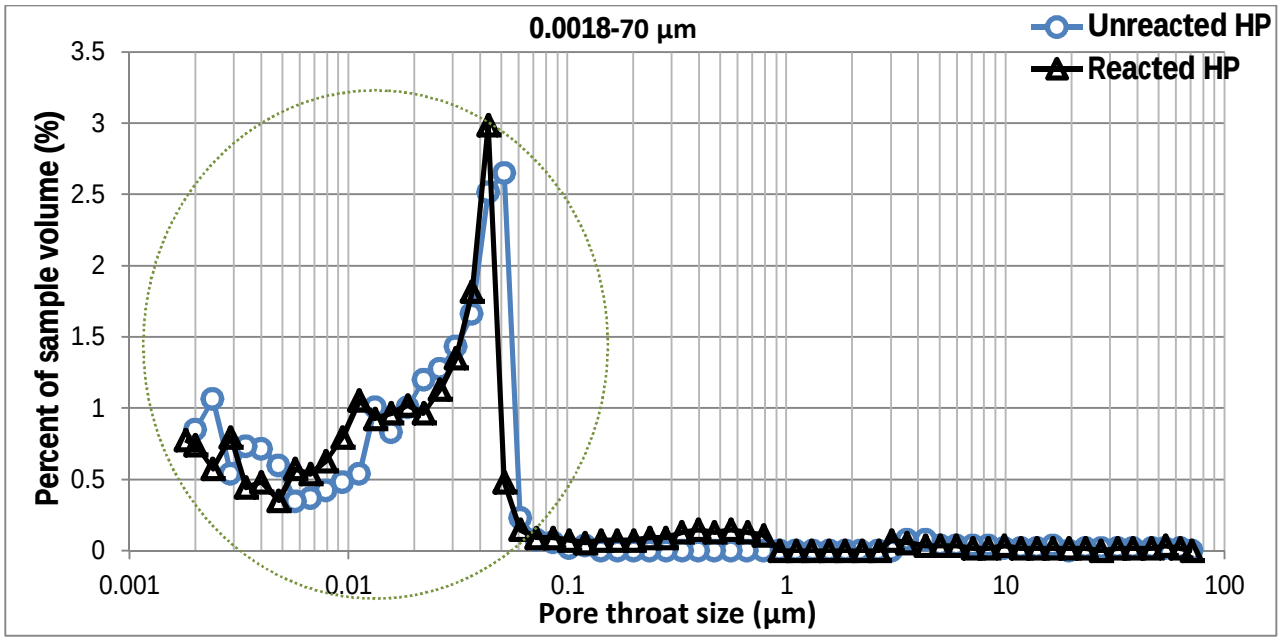

Figure 4.18: Pore Throat Size Distribution between 0.0018 µm and 70 µm for High Pressure Experiment

Figure 4.18 shows the pore throat size distribution for all sub-intervals in the high pressure experiment. In contrast to the low pressure experiment, the high pressure experiment did not

`

always show porosity reduction between 0.002 μm and 0.04 μm. Instead, porosity increased between 0.005-0.01 μm at 0.04 μm. There is also a noticeable increase between 0.1 μm and 1 μm. Contribution of pore throats between 0.0018 μm and 0.1 μm to total porosity is very high (above 90%) compared to contribution from pore throats larger than 0.1 μm in the low and high pressure experiments. All the porosity changes in sub-intervals are tabulated in Table 4.5.

Here, pores having pore throats smaller than 5 μm are referred to as micropores while pore pores having pore throats equal to or larger than 5 μm are considered macropores. Total porosity is the sum of microporosity and macroporosity. Total porosity decreased from ~26% to ~20% in the low pressure experiment. Microporosity decreased in the low pressure experiment and slightly increased as a result of the high pressure experiment. Macroporosity decreased in the Reacted LP_7-8 (inlet) sample and increased in the Reacted LP_1-2 (outlet) sample. The high pressure experiment resulted in the reduction in macroporosity. As opposed to the low pressure experiment, the high pressure experiment resulted in a slight (1.8%) total porosity increase.

Table 4.5: Summary of Pore Throat Size Distribution for Low and High Pressure Experiments

Pore throat size Sub-Interval	Unreacted LP (Control)	Reacted LP_7-8 (Inlet)	Reacted LP_1-2 (Outlet)	Unreacted HP (Control)	Reacted HP
0.0018-0.1μm	24.51 %	19.79 %	18.95 %	20.64 %	19.78 %
0.1-0.5 μm	0.95 %	0 %	0.53 %	0.058%	0.947 %
0.5-5 μm	0.27 %	0.22 %	0.198 %	0.1548 %	0.557 %
5-70 μm	0.58 %	0.49 %	0.748 %	0.387 %	0.35 %
Total Porosity	**26.31 %**	**20.5 %**	**20.426 %**	**21.24 %**	**21.63 %**

`

4.4 Environmental Scanning Electron Microscopy (ESEM) Coupled with Energy Dispersive Spectroscopy (EDS)

Microstructural characterization provides spatial distrubution of different mineral phases before and after the flow-through experiments. EDS analysis is routinely applied to provide chemical elemental identification of microstructural features. ESEM analyses are presented in order to understand the microstructural alterations causing porosity changes in reacted cement cores. These images also provide insight into dissolution and precipitation reactions which occur during acidic brine exposure. The ratio of Calcium to Silicon (Ca/Si), determined by EDS analysis, is an aid in determining influx of Ca^{2+}. When Ca^{+2} rich minerals precipitate in the cement matrix, spot analysis of that region will show increased Ca/Si ratios. Figure 4.19 compares the unreacted and reacted cement cores for an inlet section in the low pressure experiment. Figure 4.19-b reveals calcite deposition within cement matrix and remaining Portlandite minerals indicated with arrows. Ca/Si is 5.64 for the unreacted cement core, shown in Figure 4.19-a. Reacted core has a Ca/Si of ~30 (Figure 4.19-b).

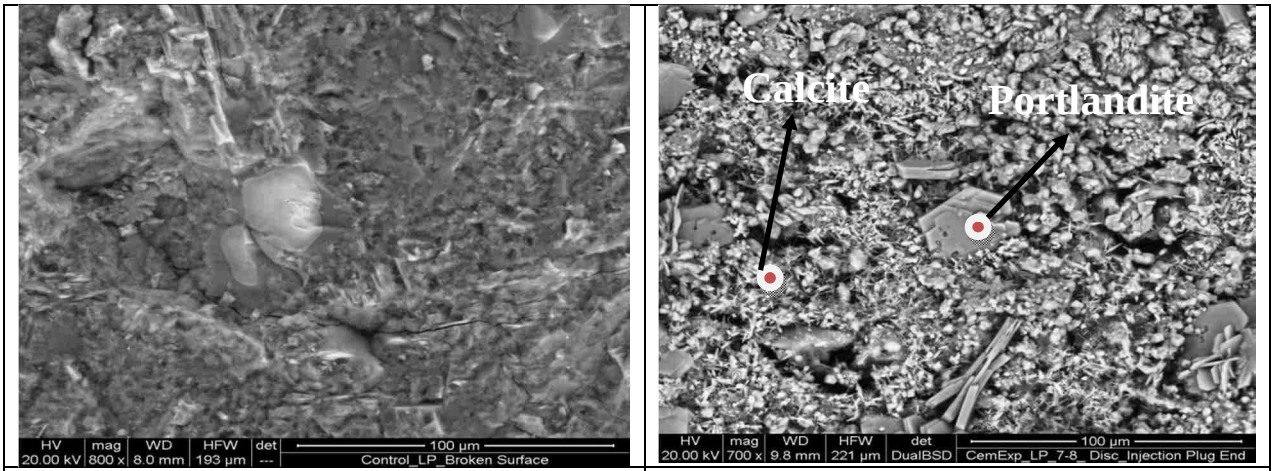

a) Unreacted core, dense cement matrix

b) Reacted core showing calcite precipitation

Figure 4.19: ESEM Images of Unreacted and Reacted Cement Cores for Low Pressure Experiment (inlet section)

`

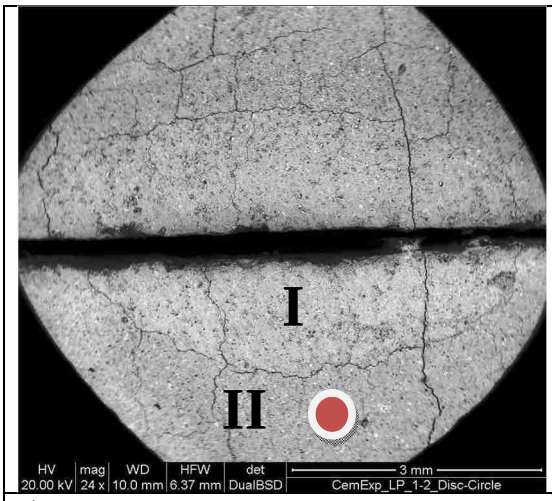

a) Fracture–top view

Element	Wt %	At %
O K	42.14	62.65
SiK	10.81	09.16
ClK	00.84	00.56
CaK	39.24	23.29
FeK	03.87	01.65

b) EDS analysis of the spotted region

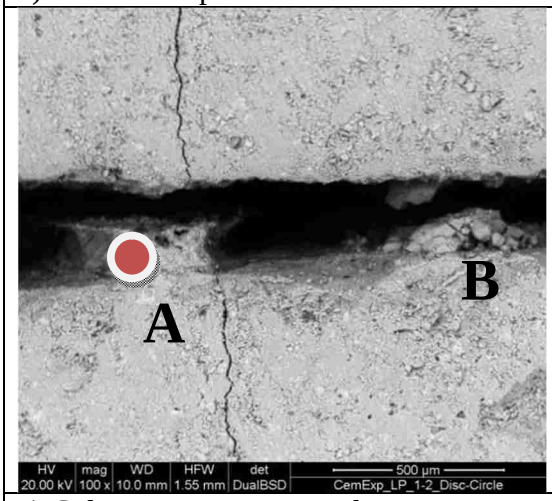

c) Calcite Deposition Inside Fracture

Element	Wt %	At %
C K	02.18	04.41
O K	37.86	57.53
SiK	04.06	03.51
ClK	02.25	01.54
CaK	51.87	31.47

d) EDS data verifies calcite deposition

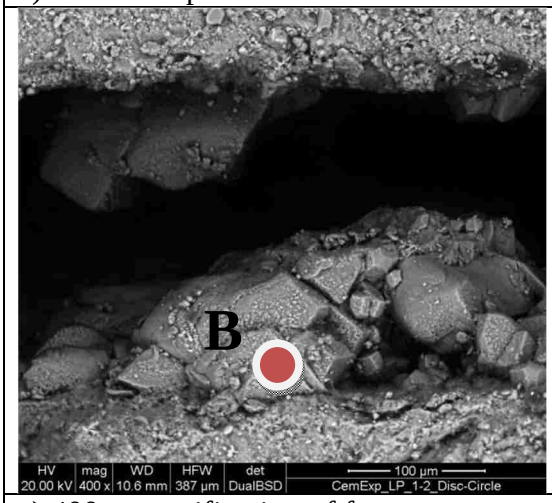

e) 400x magnification of fracture

Element	Wt %	At %
C K	02.98	05.50
O K	48.20	66.85
SiK	01.56	01.24
S K	00.26	00.18
CaK	45.65	25.27

f) EDS analysis of Ca^{2+} rich deposits

Figure 4.20: ESEM Images of Fracture Wall for Low Pressure Experiment (outlet section)

Figure 4.20 shows the top view of the fracture in 24x, 100x and 400x magnifications for an outlet section in the low pressure experiment. Deposits inside the fracture, denoted with A and B, are shown in Figure 4.20-a, c and e.

Also Ca/Si ratios can be calculated from the EDS analyzes (weight percentages are given in K count) for selected regions. For the region II shown in Figure 4.20-a, Ca/Si ratio was 3.62 which indicates leaching of Ca^{2+} from that region, when it is compared to the unreacted sample which has a Ca/Si of 5.64. For structures A and B in the Figures 4.20-c and e, Ca/Si increased to ~13 for structure A and ~30 for structure B. This suggests that Ca^{2+} leached from the cement matrix and deposited in the form of calcite inside the fracture. The structures are considered to be $CaCO_3$ due to both the crystal shape and the EDS analysis which suggests the co-existence of Ca^{2+}, C^{4+} and O^{-2}.

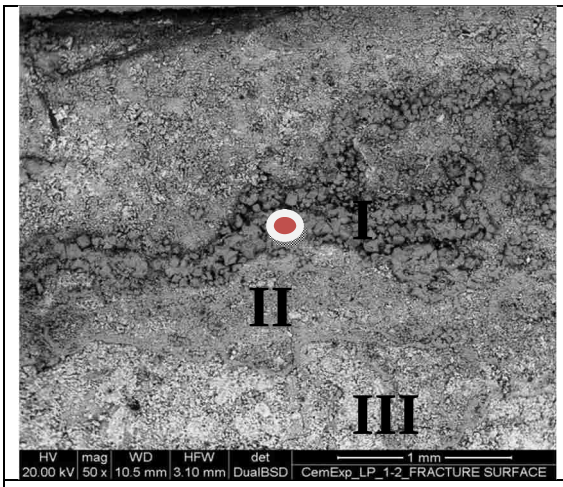

a) Calcite precipitation on fracture surface

Element	Wt %	At %
C K	04.13	07.42
O K	50.27	67.81
SiK	02.38	01.83
CaK	41.02	22.09
FeK	02.21	00.85

b) EDS data for region I

Figure 4.21: ESEM Image of Fracture Surface Shown with EDS analysis for Low Pressure Experiment (inlet section)

Figure 4.21 shows the fracture surface of the outlet section of the cement core. The fracture surface was exposed directly to the acidic brine therefore, most structural changes would be

`

expected in this region. There are 3 regions that are visibly different as shown in Figure 4.21-a. The Ca/Si ratio for regions I and III are ~17 and ~9 (Appendix C) respectively. There was no measurement done in region II but EDS analyses of regions I and III suggest a gradual Ca/Si ratio reduction from region I to III. Figure 4.21-b also shows the existence of Fe^{3+} which is likely coming from an unhydrated Ferrite component of the Portland cement.

Figure 4.22 is a high magnification image of Portlandite-$Ca(OH)_2$ (EDS data shows 40% calcium and 47% oxygen-Appendix C) minerals surrounded by calcite minerals in the inlet section of the core for the low pressure experiment.

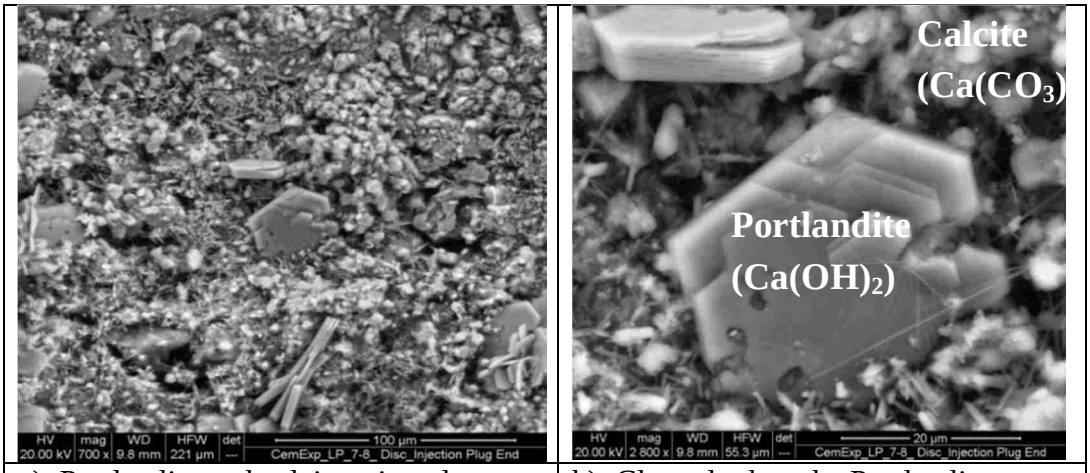

a) Portlandite and calcite minerals | b) Closer look at the Portlandite

Figure 4.22: High Magnification ESEM Images for Low Pressure Experiment (inlet section)

Low magnification ESEM images of the unreacted and reacted cores for the high pressure experiment are shown in Figure 4.23. The cement core is not significantly altered with acidic brine exposure since unreacted and reacted cement cores have visibly similar matrixes.

Figure 4.24 presents higher magnification images of the reacted cores for the high pressure experiment. Figure 4.24-a is an 800x magnification image of the reacted sample. Calcite

`

minerals are deposited in the middle (region II) in the forms of cubes. Region I and III are primarily composed of C-S-H, which appears like needles, but Region III appears denser than Region I. Region II has Ca/Si of ~10, suggesting the existence of Ca^{2+}-rich minerals; Region I has a Ca/Si ratio of 3.7, which is close to the Ca/Si of 4.94 for the unreacted cement core showing it was significantly altered.

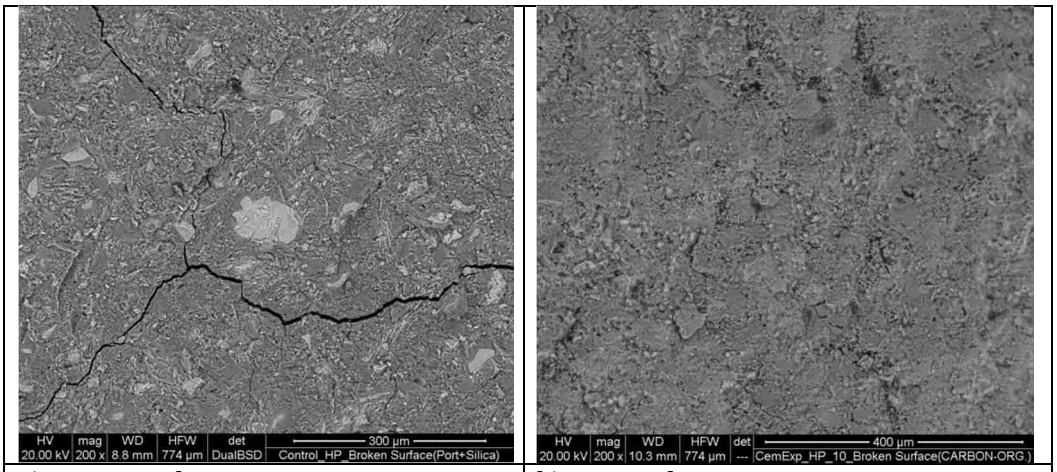

a) Unreacted cement core | b) Reacted cement core

Figure 4.23: Low Magnification ESEM Images for High Pressure Experiment

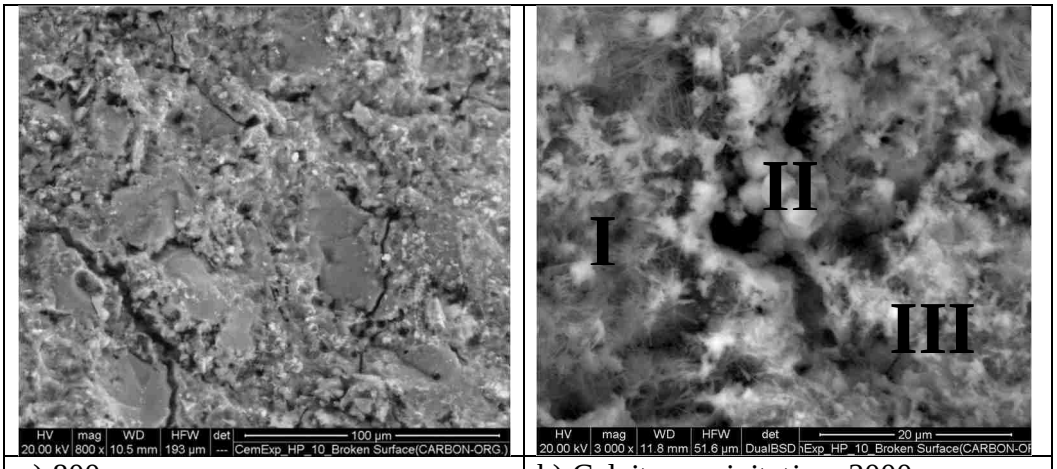

a) 800x | b) Calcite precipitation, 3000x

Figure 4.24: High Magnification ESEM Images of Reacted Samples for High Pressure Experiment

`

4.5 X-Ray Diffraction (XRD)

XRD analyses were conducted to complement the results which were presented related to fracture aperture change, porosity and microstructural alterations, in terms of mineralogy. Reference Intensity Ratios (RIR) were required to compute the weight percentages of the minerals, and they were not integrated into the computer software used in XRD. Therefore quantification of weight percentages of minerals could not be achieved. Although there was no weight percentage data for experiments, the reduction or increase in the amount of the mineral phases can be identified from the peak ratios of relevant phase diffractograms, for example Portlandite peaks before and after the flow-through experiments.

In this study, flow was achieved through a controlled fracture therefore, cement/fluid interaction is expected to be highest at the fracture wall. XRD is a bulk technique that requires powdering a sample and analyzing it as an average of the amount of minerals present in the sample. Averaging minerals may lead to misunderstanding of the minerals in the region of interest. In order to avoid this, XRD analyzes were conducted on the sections which were cut directly from fracture surfaces so that actual alteration can be identified. Portlandite (marked with P) has a main peak at around 34 degrees and calcite (marked with CC) has a main peak at 29 degrees. Both minerals have other minor peaks presented below.

Figure 4.25 presents 2-theta versus intensity plot for XRD analyzes for low and high pressure experiments. It depicts that Portlandite mineral was totally dissolved and calcite amount increased to approximately 5 times of its original value as a result of cement/fluid interaction. The high pressure experiment resulted in similar mineral characteristic alterations with the low pressure experiment, as identified from the peaks

`

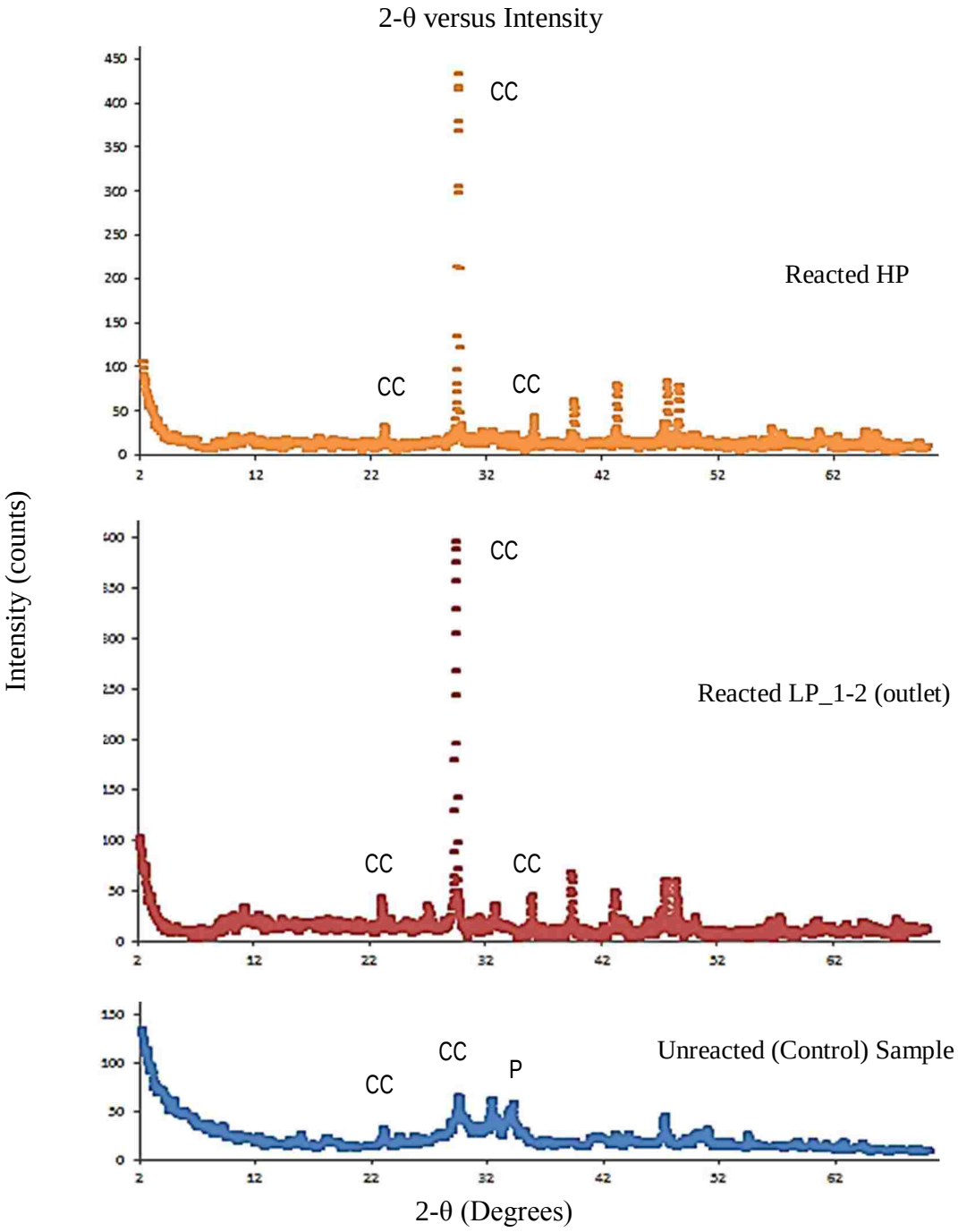

Figure 4.25: XRD Plot Showing Mineralogical Alterations for Low and High Pressure Experiments (CC and P represent Calcite and Portlandite respectively)

4.6 Inductively Coupled Plasma-Optical Emission Spectroscopy (ICP-OES)

Analyzing unreacted and reacted cement cores using several material characterization techniques provides insight into alterations in the cement internal structure, the changes that occurred in the solid specimen needed to be verified with changes in the fluid component of the cement/brine system. Acidic brine was flowed through the controlled fracture, and it interacted with the cement fracture surface. Hence, brine chemical analysis can contribute to our understanding of the dissolution and precipitation processes. CO_2 saturated brine samples, both influent and effluent, were evaluated by measuring pH, ICP analysis and carbonate/bicarbonate concentrations. ICP analysis of effluent brine samples and experimentally determined alkalinity values are provided in Table 4.6 for the low pressure experiment. Carbonate ions were not detected in the first 4 effluent brine samples due to pH being lower than 8.3 (Table 3.4)[69]. When calcium leached out of the cement matrix as a result of the acidic brine attack the concentration of Ca^{2+} in the effluent brine increased. Saturation index (SI) calculations were carried out in order to decide whether the brine solution was oversaturated or undersaturated in terms of calcite.

Table 4.6: Alkalinity Measurements for Low Pressure Experiment

#Days	Ca^{2+} (mg/l)	Influent pH	Effluent pH	m_f	p_f	HCO_3^- (mg/l)	CO_3^{-2} (mg/l)	OH^- (mg/l)
Control	0.48	4.9	-	0.22	0	134.2	0	0
1	39.40	5.2	5.9	0.56	0	341.6	0	0
6	16.65	5.2	6.9	0.23	0	140.3	0	0
12	14.83	5	6.8	0.12	0	73.2	0	0
15	12.69	5.1	9.5	0.42	0.11	122	66	0
18	18.05	4.9	10.2	0.17	0.06	30.5	36	0
21	11.55	4.9	9.6	0.22	0.01	122	6	0
24	11.51	5	9.3	0.15	0.02	67.1	12	0
30	20.05	4.9	10.1	0.25	0.13	0	72	1.7

`

An example calculation for the effluent sample taken after 24 days of experiment is shown below. Na^+ (0.3455 m), K^+ (0.0046 m) and Cl^- (0.3502 m) co-exist in our system and ionic strength calculations were computed based on these species.

Activity coefficient calculations:

$$\text{Ionic Strength} = 0.5\,(0.3455 + 0.0046 + 0.3502) = 0.35\ \text{m}$$

$$\log \gamma_{Ca^{+2}} = \frac{(-0.5091 \times (2)^2 \times 0.351/2)}{1 + \frac{0.351}{2}} + (0.10182 \times (2)^2 \times 0.35)$$

$$\gamma_{Ca^{+2}} = 0.243 \qquad \gamma_{HCO_3^-} = 0.702 \qquad \gamma_{CO_3^{-2}} = 0.243$$

Activity calculations:

$$a_{Ca^{+2}} = \gamma_{Ca^{+2}} \times \text{molality (mol/kg)}$$

Molality (m) values for ions are obtained by dividing their concentrations (given in mg/l) to their molecular weights.

Saturation Index calculations for the sample collected after 24 days;

Activity of Calcium can be computed as,

$$a_{Ca^{+2}} = 11.51 \div 40 \div 1000 \times 0.243 = 6.99E-05 \ (\text{Molecular Weight of } Ca^{+2} = 40\ \text{g/mol})$$

Activity of Carbonate is found to be,

$$a_{CO_3^{-2}} = 12 \div 60 \div 1000 \times 0.243 = 4.86E-05 \ (\text{Molecular Weight of } CO_3^{-2} = 60\ \text{g/mol})$$

Ion Activity Product (IAP) can be calculated by multiplying activities of Ca^{2+} and CO_3^{-2}.

$$IAP = a_{Ca+2} \times a_{CO_3^{-2}} = 3.39E-9$$

$$\text{Saturation Index (SI)} = \log(IAP) - \log(K_{sp}) = \log(3.39E-9) - \log(10-8.48) = 0.011$$

(Equlibrium constant is known at atmospheric conditions, $K_{sp} = 10^{-8.48}$)[29]

`

Since SI is positive, calcite is slightly oversaturated in the sample collected after 24 days. Hence, calcite should be precipitating in cement at that time.

As shown in Table 4.7, saturation indices were positive except for the effluent sample collected after 21 days of experiment. When the pH of the sample is below 8.3, carbonate concentration is 0 according to OFITE Drilling Fluids Manual[69] because carbonate concentration is very small that it cannot be detected with alkalinity test. Hence, carbonate concentrations in the first four data points (Table 4.6) are 0. Even though no carbonate ions were measured for these data points using alkalinity test, carbonate concentration can still be calculated using measured bicarbonate concentrations from Equation 10, page 18. Carbonate concentrations and saturation indices were computed for these points. Saturation indices were plotted against time in Figure 4.26. As Figure 4.26 illustrates, initial brine composition was highly undersaturated with calcite and effluent brine samples were becoming oversaturated in the second half of the experiment. The trend of being oversaturated with calcite implies that calcite was precipitating on the cement matrix.

Table 4.7: Saturation Indices for Low Pressure Experiment

#Days	Ion Activity Product	Saturation Index
Control	1.05E-14	-5.49, undersaturated
1	3.48E-11	-1.97, undersaturated
6	6.06E-11	-1.73, undersaturated
12	2.23E-11	-2.16, undersaturated
15	2.06E-8	0.79, oversaturated
18	1.59E-08	0.68, oversaturated
21	1.7E-09	-0.28, undersaturated
24	3.39E-09	0.011, oversaturated
30	3.55E-08	1.03, oversaturated

`

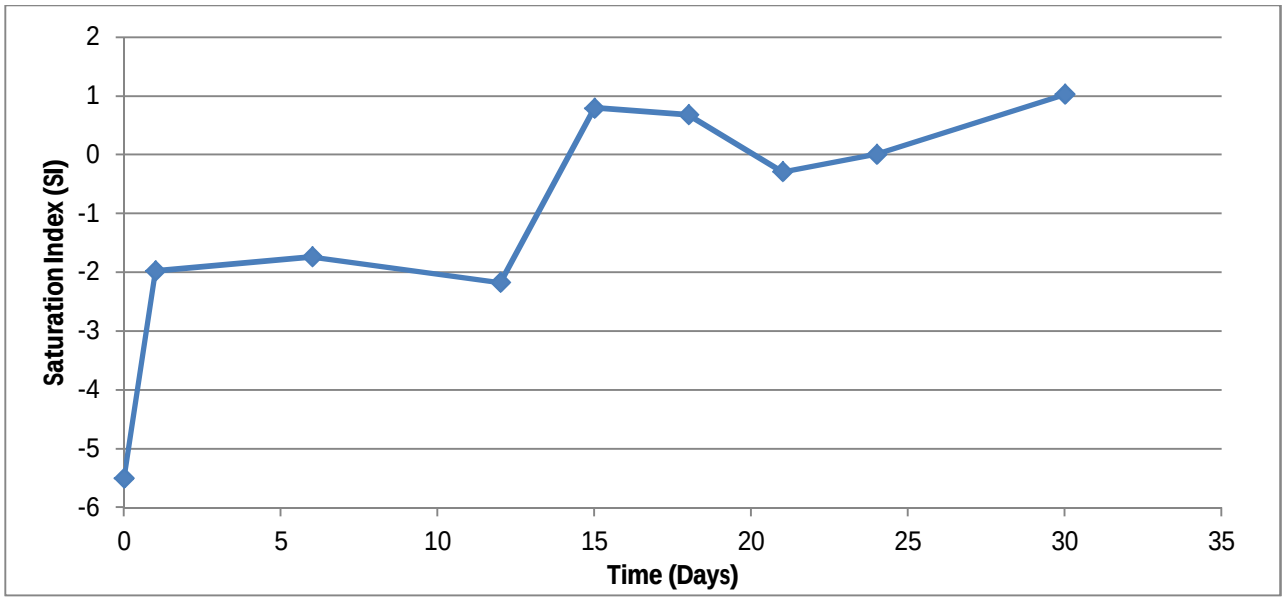

Figure 4.26: Saturation Indices for Low Pressure Experiment

The degree of oversaturation/undersaturation with calcite is strongly dependent on the pH of the analyzed brine sample. Since CO_3^{-2} does not virtually exist at pH values lower than 8.3, which is also shown in Figure 2.5 (page 19), it is impossible to obtain an oversaturated solution because IAP is very low resulting in negative SI values. In samples having pH values higher than 8.3, as samples presented in Table 4.7 (except sample collected after 21 days), carbonate concentration is high leading to high IAP and positive SI values. Hence, brine samples became oversaturated.

4.7 Discussion of Results

4.7.1 Dissolution and Precipitation Reactions

When solutions with different pH values come into contact with each other, they tend to equilibrate by exchanging the H^+ and OH^- ions. In this study, acidic brine which had a low pH, was flowed through a controlled fracture within a core. As previously stated, the cement pore solution is highly alkaline (pH ~13) and the acidic brine used in this study had pH values from

`

4.9 to 5.2. The high alkalinity property of the cement pore solution is provided by the abundance of Na^+, K^+, and OH^- ions in the pore solution. At the same time, the high pH environment provided favorable conditions for Portlandite ($Ca(OH)_2$) crystal growth. This incompatibility between two different systems resulted in leaching of OH^- from the pores. Portlandite ($Ca(OH)_2$) starts to dissolve in order to provide a new supply of OH^- ions to the environment to help the system come into equlibrium. Calcium in solution from the dissolution of Portlandite combine with CO_3^{-2} ions and precipitate as calcite ($CaCO_3$). Our results show that precipitation of calcite occurrs in preferential locations on the fracture surface, especially within the dissolved regions where reaction provided new free volume as shown in ESEM images (Figure 4.21). However, conversion from Portlandite to $CaCO_3$ is a volume reducing reaction[37] resulting in a decreased volume of dark areas (reduction in porosity), shown in Figure 4.24. Carbonation also resulted in having a Ca/Si of 12 and 45 (Figure 4.20-d&f) from the unreacted sample having Ca/Si of 5.64 as presented in ESEM images (Figure 4.19-a). As described before, fracture surfaces are directly in contact with the acidic brine so dissolution is expected in these regions. This showed that precipitation took place where dissolution reactions occur. This indicates that dissolved regions are preferential regions for carbonation. ESEM image (Figure 4.24) showing calcite precipitation inside pores are in agreement with field study results presented by Carey et al.[51].

Calcium which was not converted into calcite was detected in the effluent brine samples for the low pressure experiment. Further geochemical calculations indicated that samples were oversaturated with calcite. That clearly shows the occurrence of precipitation while leaching of Ca^{2+} takes place. One of the brine samples was slightly undersaturated (SI= -0.28) but in overall, samples were oversaturated with calcite. Figure 4.26 clearly shows the transition from being undersaturated to oversaturated.

`

Figure 4.27 summarizes the chemical processes taking place on the fracture surface upon contact with acidic brine resulting in the widening of the fracture. XRD data revealed that calcite precipitated during the low and high pressure experiments as shown in Figure 4.25.

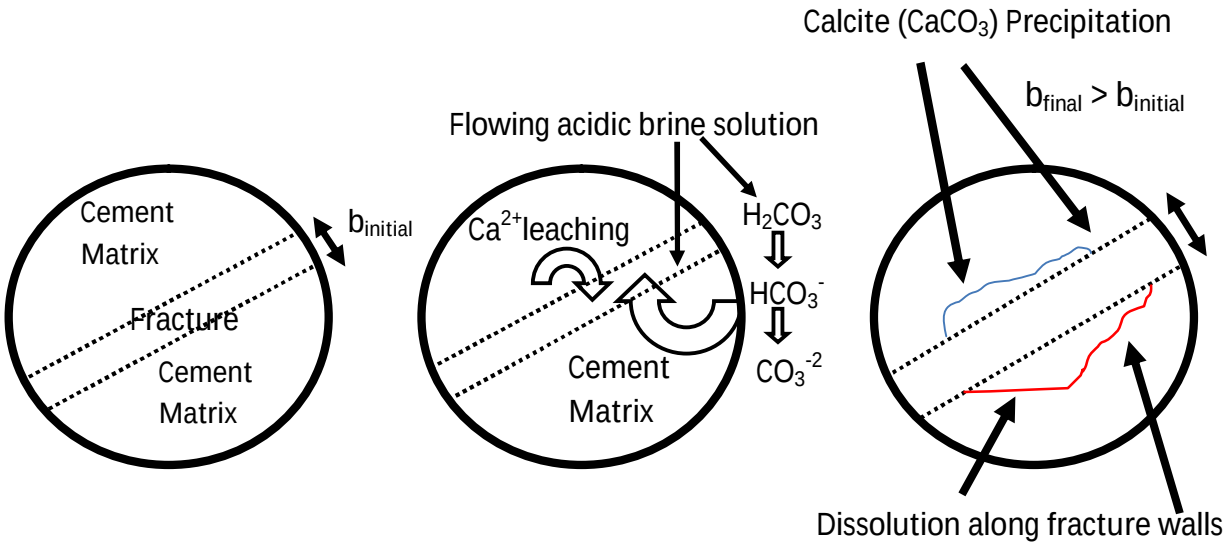

Figure 4.27: Summary of Chemical Reactions Occurring around Fracture Wall with Acidic Brine Exposure

It should be noted that since XRD is a bulk analysis technique, averaging of the mineral amounts may not reflect the true percentages on the reacted surfaces but still provide more reliable results than powdering the samples. Wigand et al.[50] reported depletion of Portlandite and calcite precipitation after supercritical CO_2 exposure which agrees with our observations shown in Figure 4.25.

4.7.2 Fracture Aperture Widening

The primary objective of this study was to investigate the change in the fracture aperture with exposure to acidic brine. It was found that fracture aperture was larger as a result of the low pressure experiment. First, fracture apertures were compared using low resolution CT, a non-destructive technique which was utilized prior to and post experiment. Measurements conducted

`

using ImageJ[67] at similar locations (Figure 4.2) showed widening of the fracture 20% to 50%. Slice #8 showed a higher percent of widening (34%) than slice #1 (18%) probably due to being the first contact point with acidic brine and having more severe reactions. The widening of the fracture was supported with the cubic law calculations done using pressure drop measurements. Calculated apertures showed fluctuations due to dissolution and precipitation reactions with time but the final calculated fracture aperture was larger than the initial value indicating widening of the fracture. The increase in the calculated fracture aperture is small compared to the measurements from the low resolution CT images. This can be explained with the difference in measurement techniques; aperture calculations were carried out under confined stress conditions and CT images were obtained under unconfined conditions. Confined stress conditions tend to minimize the widening of the cement fracture. The widening of the fracture and precipitation of calcite (Figure 4.20) inside the fracture were also observed by Wigand et al.[50].

Possible reaction scenarios between a cement fracture and acidic brine in the field may result in fracture widening smaller than the widening observed in this experiment due to the higher confinement stress. This is contradicting with the Huerta et al.[47] study where they conclude that fractures may close under the loading stress cycles because their experiments are more applicable to injection wells during injection. In a possible injection scenario loading cycles may result in closing the fracture but dynamic alteration on the fracture surface tend to increase the fracture aperture. Moreover, after the injection ceases and there are no more loading cycles, dynamic alteration still contribute to the widening of the fracture.

4.7.3 Porosity Alteration

Dissolution (leaching) and precipitation (carbonation) have opposite effects on porosity; carbonation in confined space reduces porosity whereas leaching increases the porosity[38].

`

Carbonation[37], the conversion of Portlandite into calcite, as reported in the literature results in losing some of the void space since Portlandite (33.1 cc/mol) occupies less volume than calcite (36.9 cc/mol).

During the low pressure experiment precipitation reactions dominantly took place resulting in the reduction of total porosity from 26% to 20% (~23% reduction). Figure 4.28 shows the cumulative intrusion curve which indicates porosity reduction and cumulative intrusion values plotted against capillary pressures for the low pressure experiment. Capillary resistance increased indicating a higher pressure differential needed to reach same pore throats in the reacted samples. For capillary pressures lower than 2,000 psia cumulative intrusion was larger in the Reacted LP_1-2 sample (outlet) than the Reacted LP_7-8 sample (inlet), probably due to more severe dissolution and precipitation reactions taking place in the inlet section. In capillary pressures higher than 2,000 psia cumulative intrusion values of inlet and outlet sections appeared to follow similar trends. This suggests that with a pressure differential lower than 2,000 psia fluid can access more space in the outlet section. In higher capillary pressures a fluid can intrude the same amount of space in inlet and outlet sections. In the low pressure experiment, four sub-intervals were identified: 0.0018-0.1 μm, 0.1-0.5 μm, 0.5-5 μm and 5-70 μm. Pore throats smaller than 5 μm constituted more than 90% of the total porosity. The porosity associated with the lowest pore throat size range (0.0018-0.1 μm) was reduced. Porosity associated with the largest pore throats increased for the outlet section of the cement core, confirmed by MIP and image based porosity using Micro-CT images which were also in agreement with results reported by Bishop et al.[70]. Calcite precipitation blockage caused the porosity reduction. Leaching took place in large pore throats (5-70 μm) which resulted in an increase in the porosity in the outlet section. An

`

opposite behavior was observed in the inlet section of the cement core which can be due to the continuous contact of fresh acidic brine (rich in CO_2) having a low pH with cement. This contact resulted in a carbonation dominant reaction which decreased total porosity.

Pore throats smaller than 0.01 μm are not involved in the leaching process of Ca^{2+}, therefore this is not the primary concern for cement degradation process. As more Portlandite leaches from the cement matrix the void space becomes larger. This reflects into the volume of the larger pore throats between 5-70 μm which is important as large pore throats become accessible at lower pressures.

The high pressure experiment resulted in a slight increase (1.8%) in total porosity from 21.26% to 21.64%. The cumulative intrusion curve for the high pressure experiment is shown in Figure 4.29. Capillary resistance was increased with acidic brine exposure in this experiment. Separation between cumulative intrusion curves around 1,000 psi is more distinct suggesting that larger pore throats are more affected by leaching than smaller ones. The short duration of this experiment possibly played a role in the increase of the porosity due to leaching. Large pore throats (5-70 μm) decreased in this experiment but it may be more reasonable to say they did not change because MIP measurements may not be very accurate. Micro-CT suggested that macroporosity remained at a value close to the unreacted sample. It does not completely agree with MIP measurements but it suggests that less alteration took place than the low pressure experiments. Also, the two measurements are different, as MIP is more like a bulk analysis whereas Micro-CT is a more localized analysis.

`

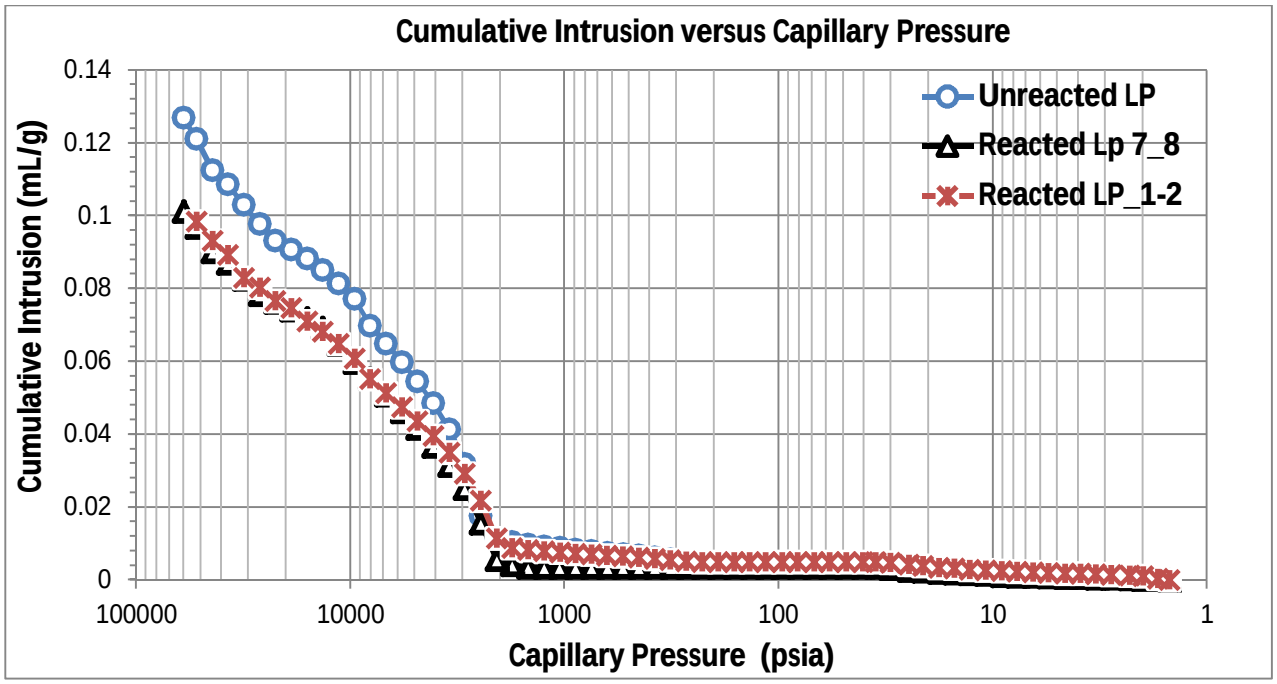

Figure 4.28: Cumulative Intrusion Curve for Low Pressure Experiment

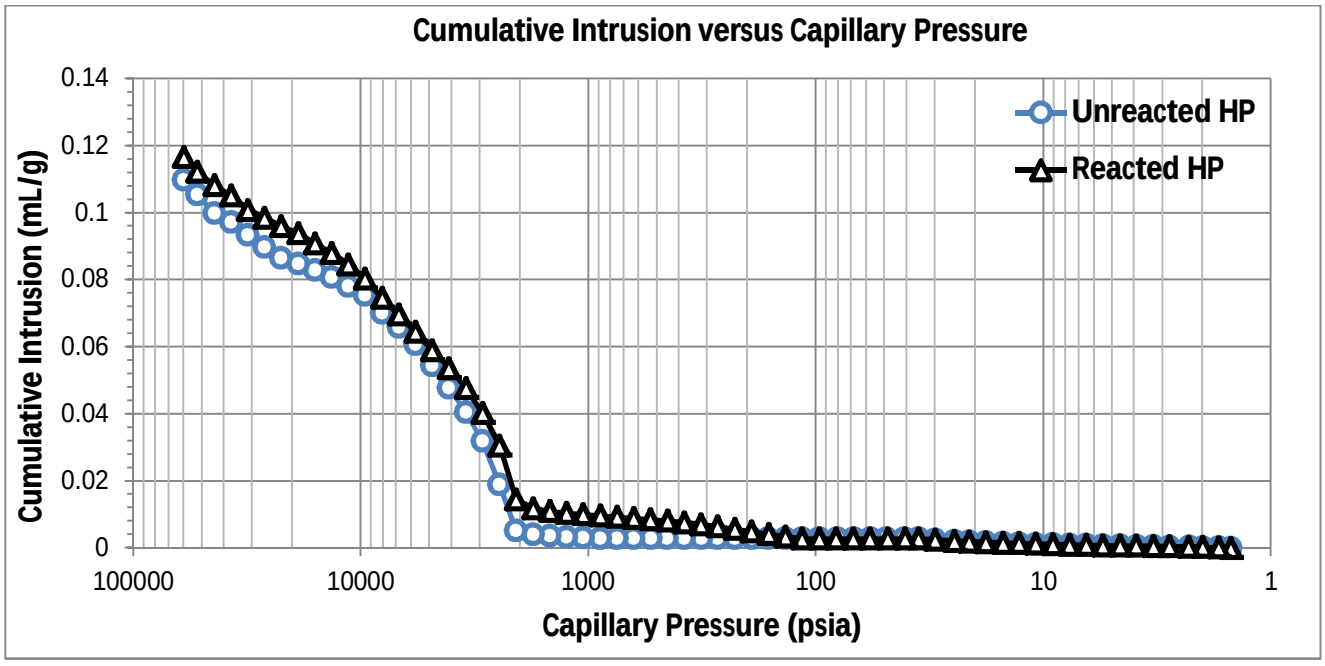

Figure 4.29: Cumulative Intrusion Curve for High Pressure Experiment

`

4.7.4 Effect of Time

Time appears to be the main factor when deciding on the dominant mechanism during the reactions. Differences observed in low and high pressure experiments show the effect of time. Thirty days were sufficient for the carbonation to be the dominant reaction, whereas, 10 days was not enough for the carbonation mechanism to be dominant over leaching as implied by the change in porosity.

Quantitative XRD analysis is presented in Table 4.8. It revealed complete consumption of Portlandite and precipitation of calcite. Initial amounts of Portlandite were converted into calcite, silicate phases and some of them were carried out with the acidic brine solution. When Portlandite is totally consumed calcite will be dissolved (Equation 19, page 20). The preliminary study showed that 8 weeks of exposure was not even sufficient to start calcite consumption. It should be noted that as dissolution occurs, hydration of cement continues as inferred from increasing amount of Calcium Silicate (C-S-H).

The preliminary study was conducted in spring 2009 semester for 8 weeks. In the first 4 weeks, acidic brine was flowed at a rate of 1.65 ml/min. The flow rate was increased to 1 ml/min in the second 4 weeks. Acidic brine was flowed through an artificial fracture in the center of 1 in by 2 in core under unconfined stress conditions. Micro-CT images, shown in Figure 4.30, showed one fold porosity increase in pores greater than 10 μm from Region I to Region III. Region I has no porosity. Region III, which was directly exposed to acidic brine, had 2% of porosity which is larger than the value calculated for the low and high pressure experiments (0.47% and 0.2% respectively). Consequently, observations show that macro porosity tends to increase with the duration of the experiment.

`

Table 4.8: Quantitative XRD Analysis for Preliminary Study (Spring 2009)

Sample Identity	Calcite (weight %)	Portlandite (weight %)	Calcium Silicate (weight %)
Control cement (unreacted)	4	87	6
After 4 weeks of 1.65 ml/day	2	88	8
After 8 weeks of 1.65 ml/day	12	63	12
After 4 weeks of 1.65 ml/day plus 4 weeks of 1 ml/min	59	3	22

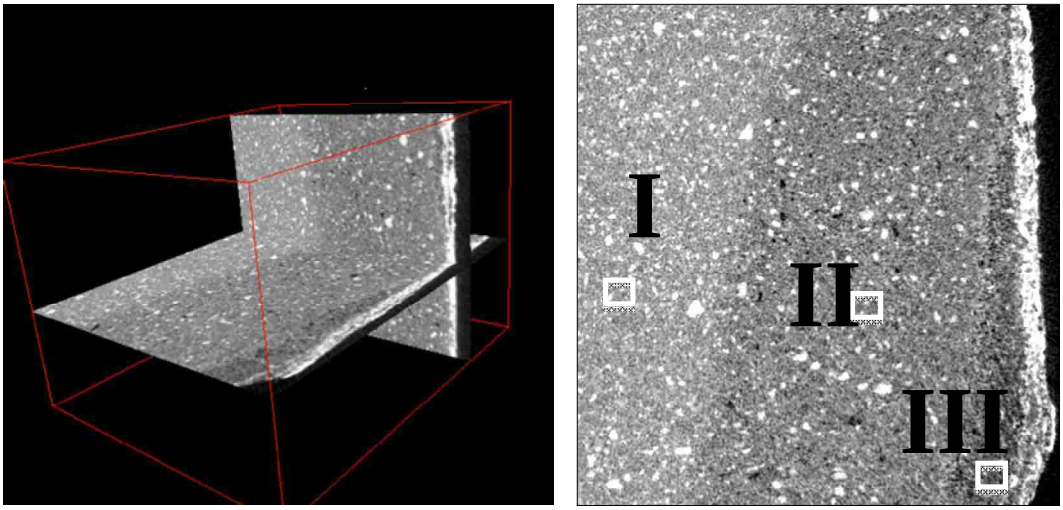

Figure 4.30: Micro-CT Image of 1 in by 2 in Core from Preliminary Study (Spring 2009)

`

CHAPTER 5

CONCLUSIONS AND RECOMMENDATIONS

5.1 Summary of Findings and Conclusions

Two sets of experiments were conducted in order to study the effect of CO_2 saturated brine on cement fractures to mimic the fractured wellbore cement sheath exposed to flowing acidic brine. A low pressure experiment was carried out for 30 days whereas a high pressure experiment was terminated after 10 days due to experimental problems. The first objective was to determine the change in the fracture aperture and the second objective was to evaluate the alterations in porosity of the reacted cement.

Fracture widening was determined from both CT images and pressure drop calculations suggesting microfractures inside the wellbore cement sheath will constitute a risk for safe and long-term CO_2 containment in the subsurface.

The low pressure experiment resulted in a lower total porosity as a result of carbonation dominant reactions. The high pressure experiment caused a slight increase in the porosity due to short duration of the experiment. These experiments confirmed that leaching and carbonation take place simultaneously. Leaching appears to be the driving force for the carbonation reaction as it initially takes place when cement is exposed to an acidic fluid. It is proven that Micro-CT enables similar porosity estimation for macropores and serves as a confirmation tool for MIP measurements as well as elucidating the change in the spatial distribution of the pore throat network.

Preliminary experiments were run for 4 and 8 weeks in spring 2009. Four weeks of experimentation did not cause any mineralogical change but 8 weeks of experimentation caused consumption of Portlandite and calcite precipitation.

`

5.2 Recommendations for Future Work

These experiments should be repeated under HPHT condition in order to make reliable long-term projections for the field conditions. Confining and net overburden stresses should be similar to downhole conditions since their effect on the behavior of cement fracture would be different. Under high pressure and temperature, solubility of CO_2 will be different which results in having different chemical kinetics between cement and acidic brine.

The effect of flowing acidic brine can be tested on the formation-cement and/or casing/cement interfaces since different formations can have a different impact on the cement and acidic brine interaction.

`

REFERENCES

1) Dr. Pieter Tans, NOAA/ESRL (www.esrl.noaa.gov/gmd/ccgg/trends) Downloaded from Earth System Research Laboratory, http:// www.esrl.noaa.gov/ gmd/ ccgg/ trends/ # global.

2) Reichle, D. et al.: "Carbon Sequestration Research and Development," U.S. Department Of Energy Report DOE/SC/FE-1, Washington D.C., USA, 1999.

3) Metz, B.,O. Davidson, H. C. de Coninck, M. Loos, and L. A. Meyer, "IPCC Special Report on Carbon Dioxide Capture and Storage," Prepared by Working Group III of the Intergovernmental Panel on Climate Change Cambridge University Press, Cambridge, United Kingdom and New York, NY, USA, 442 pp. IPCC, 2005.

4) Inventory of U.S. Greenhouse Gas Emissions and Sinks: 1990 – 2008, U.S. Environmental Protection Agency, 2010.

5) CO_2 Emissions from Fossil Fuel Combustion Highlights, International Energy Agency (IEA), 2009.

6) Downloaded from CO_2 Capture Project Official Website, http:// www.co2captureproject.org/ co2_trapping.html.

7) Downloaded from Cooperative Research Center of Australia Official Website, http:// www.co2crc.com.au/ imagelibrary2/ storage.html.

8) Downloaded from CO_2 Capture Project Official Website, http://www.co2captureproject.org/ about_capture.html.

9) A Technical Basis for Carbon Dioxide Storage, Members of the CO_2 Capture Project, 2009.

10) Downloaded from (http://www.fossil.energy.gov/programs/sequestration/capture/)

11) Downloaded from Global CCS Institute website http://www.globalccsinstitute.com/about_css/storage.html

12) Carbon Sequestration Atlas of the United States and Canada (Atlas II), Second Edition, Department of Energy (DOE), 2008

13) Ennis-King J., Paterson L., "Engineering Aspects of Geological Sequestration of Carbon Dioxide," SPE Paper 77809 presented at SPE Asia Pacific Oil and Gas Conference and Exhibition, Melbourne, Australia, 8-10 October, 2002.

14) Sengul, M.: "CO_2 Sequestration - A Safe Transition Technology," SPE 98617 presented at the SPE International Health, Safety & Environment Conference, Abu Dhabi, UAE, 2-4 April, 2006.

`

15) Downloaded from http://www.netl.doe.gov/technologies/carbon_seq/database/index.html

16) Xie X., Economides M.J., "The Impact of Carbon Geological Sequestration," SPE Paper 120333 presented at SPE Americas E&P Environmental and Safety Conference, San Antonio, Texas, March 23-25, 2009.

17) Economides M.J., Ehlig-Economides C.A., "Sequestering Carbon Dioxide in a Closed Underground Volume," SPE Paper 124430 presented at SPE Annual Technical Conference and Exhibition, New Orleans, Louisiana, October 4-7, 2009.

18) Nelson, B. E.: "Well Cementing," Schlumberger, Sugar Land, Texas, 1990.

19) Recommended Practice For Testing Oil-Well Cements And Cement Additives, API Recommended Practice 10B, Twentieth Edition, American Petroleum Institute, April, 1977.

20) Bourgoyne A.T., Millheim K.K., Chenevert M.E., Young F.S., Applied Drilling Engineering, Society of Petroleum Engineers, Texas, USA, 1986.

21) Bourgoyne A.T., Jr., Scott S. L., Manowski W.: "A Review Of Sustained Casing Pressure Occurring On the OCS," 2000.

22) Nelson B. E., Guillot D., Well Cementing. Second Edition, Schlumberger, 2006.

23) Ravi, K., Bosma, M., Gastebled, O.: "Improve the Economics of Oil and Gas Wells by Reducing the Risk of Cement Failure," SPE 74497presented at the IADC/SPE Drilling Conference, Dallas, Texas, USA, 26-28 February, 2002.

24) L. Boukhelifa; N. Moroni,; S.G. James, S. Le Roy-Delage, M.J. Thiercelin,; G. Lemaire, "Evaluation of Cement Systems for Oil and Gas Well Zonal Isolation in a Full-Scale Annular Geometry", IADC/SPE Drilling Conference, 2-4 March 2004, Dallas, Texas, USA, 2004.

25) Downloaded from http://scifun.chem.wisc.edu/chemweek/pdf/CarbonDioxide.pdf

26) Downloaded from www.gov.pe.ca/photos/original/ftc_novnews.pdf.

27) Downloaded from http://dhs.wi.gov/eh/ChemFS/fs/CarbonDioxide.htm

28) Hanor, J., "Geochemistry Lecture Notes," Louisiana State University, Spring 2010.

29) Zhu C., Anderson G.M., "Environmental Applications of Geochemical Modeling," 2002.

30) Duan Z., Sun R., "An improved model calculating CO_2 solubility in pure water and aqueous NaCl solutions from 273 to 533 K and from 0 to 2000 bar", Chemical Geology 193, 257– 271, 2003.

`

31) Downloaded from http://www.geo.cornell.edu/geology/classes/geo455/Chapters.HTML

32) Weiner E. R., Applications of Environmental Aquatic Chemistry: A Practical Guide, Second Edition, 2007.

33) Downloaded from http://www.kgs.ku.edu/PRS/publication/2003/ofr2003-33/P1-05.html34)

34) Kestin J., Khalifa HE., Correia RJ.: "Tables of the dynamic and kinematic viscosity of aqueous NaCl solutions in the temperature range 20–150 C and the pressure range 0.1–35 MPa, "Journal Of Physical & Chemical Reference Data Volume: 10 (1), January, 1981.

35) Hewlett P.C., Lea's Chemistry of Cement and Concrete, Fourth Edition, Elsevier, 1998.

36) Kutchko, B. G., Strazisar, B. R., Dzombak, D. A., Lowry, V. G., Thaulow, N.:"Degradation of Well Cement by CO_2 under Geologic Sequestration Conditions, " Environmental Science Technology, 41 (13), 4787-4792, 2007.

37) Glasser F. P., Marchand J., Samson E., "Durability of concrete — Degradation phenomena involving detrimental chemical reactions," Cement and Concrete Research, Volume 38, Issue 2, , Pages 226-246, February 2008.

38) Van Gerven T., Cornelis G., Vandoren E., Vandecasteele C., "Effects of carbonation and leaching on porosity in cement-bound waste," Waste Management, Volume 27, Issue 7, Pages 977-985,2007.

39) Balonis M., Glasser F.P., "The density of cement phases," Cement and Concrete Research, Volume 39, Issue 9, Pages 733-739, September 2009.

40) García-González C. A., Hidalgo A., Fraile J., López-Periago A.M., Andrade C., Domingo C., "Porosity and Water Permeability Study of Supercritically Carbonated Cement Pastes Involving Mineral Additions," Industrial & Engineering Chemistry Research, 46 (8), pp 2488–2496, 2007.

41) Onan, D.D.: "Effects of Supercritical Carbon Dioxide on Well Cements," SPE 12593 presented at the Permian Basin Oil and Gas Recovery Conference, Midland, Texas, USA, 8-9 March, 1984.

42) Bruckdorfer, R.A.: "Carbon Dioxide Corrosion in Oilwell Cements," SPE 15176 presented at the SPE Rocky Mountain Regional Meeting, Billings, Montana, USA, 19-21 May, 1986.

43) Duguid, A., Radonjic, M., Bruant, R., Scherer, G.W.: "Degradation of well cements exposed to carbonated brine" Proceedings of the 4th annual conference on carbon capture and sequestration, Monitor and exchange publications and forum, Washington D.C., USA, May 2-5, 2005.

`

44) Barlet-Gouedard, V., Rimmele, G., Goffe, B. and Porcherie, O.: "Mitigation Strategies for the Risk of CO_2 Migration through Wellbores," IADC/SPE 98924 presented at the IADC/SPE Drilling Conference, Miami, Florida, USA, 21-23 February, 2006.

45) Kutchko, B. G., Strazisar, B. R., Dzombak, D. A., Lowry, V. G., Thaulow, N.: "Rate of CO_2 Attack on Hydrated Class H Well Cement under Geologic Sequestration Conditions," Environmental Science Technology 42 (16), 6237-6242, 2008.

46) Huerta N.,J., Bryant Steven, L., Conrad Lauren, C.: "Cement Core Experiments With a Conductive Leakage Pathway, Under Confining Stress and Alteration of Cement's Mechanical Properties via a Reactive Fluid, as an Analog for CO_2 Leakage Scenario," SPE 113375 presented at the SPE/DOE Symposium on Improved Oil Recovery, Tulsa, Oklahoma, USA, 23 April, 2008.

47) Huerta N., J., Bryant Steven, L., Strazisar Brian, R., Kutchko Barbara, G., and Conrad Lauren, C.: "The Influence of Confining Stress and Chemical Alteration on Conductive Pathways within Wellbore Cement," Energy Procedia-1, 3571–3578, 2009.

48) Bachu S., Bennion B.D.: "Experimental assessment of brine and/or CO2 leakage through well cements at reservoir conditions," International Journal of Greenhouse Gas Control Volume 3 (4), 494-501, July, 2009.

49) Brandvoll Ø., Regnault O. , Munz I.A., Iden I.K., Johansen H., "Fluid–solid Interactions Related to Subsurface Storage of CO_2 Experimental Tests of Well Cement", Energy Procedia 1,3367-3374, 2009.

50) Wigand, M., Kaszuba, J. P., Carey, J. W., Hollis, W. K.: "Geochemical effects of CO_2 sequestration on fractured wellbore cement at the cement/caprock interface," Chemical Geology 265 122–133, 2009.

51) Carey J.W., Svec R., Grigg R., Zhang J., Crow W.: "Experimental investigation of wellbore integrity and CO2–brine flow along the casing–cement microannulus," International Journal of Greenhouse Gas Control Volume 4 (2), 272-282, March, 2010.

52) Carey, J. W., Wigand M., Chipera S. J., Wolde G., Pawar R., Lichtner P. C., Wehner S. C., Raines M. A., Guthrie G. D.: "Analysis and performance of oil well cement with 30 years of CO_2 exposure from the SACROC Unit, West Texas, USA," International Journal of Greenhouse Gas Control 1, 75 – 85, 2007.

53) Crow W., Carey W.J., Gasda S., Williams B.D., Celia M.: "Wellbore integrity analysis of a natural CO_2 producer, " International Journal of Greenhouse Gas Control, Volume 4 (2) , 186-197, March, 2010.

54) Lomize M.G.: "Flow in Fractured Rocks," Moscow, Gosenergoizdat, 1951.

`

55) Sarkar S., Toksöz M.N., Burns D.R., “Fluid Flow Modeling in Fractures,” Earth Resources Laboratory, Department of Earth, Atmospheric and Planetary Sciences, Massachusetts Institute of Technology, 2000.

56) Witherspoon et al.: “Validity of the Cubic Law for Fluid Flow in a Deformable Rock Fracture,” Water Resources Research16 (6), 1016–1024, 1980.

57) de Marsily, G.: 1986, “Quantitative Hydrogeology”, Academic Press, San Diego, California.

58) Jones W.T., Wooten S.O., Kaluza T.J.,“Single-Phase Flow through Natural Fractures”, SPE Paper 18175 presented at the 63rd Annual Technical Conference and Exhibition, 1988.

59) Louis, C., “A Study of Groundwater Flow in Jointed Rock and its Influence on the Stability of Rock Masses,” 1969.

60) Konzuk J.S., Kueper B.H., “Evaluation of Cubic Law Based Models Describing Single-Phase Flow through a Rough Walled Fracture,” Water Resources Research 40, W02402, 2004.

61) Hakami E., Larsson E., “Aperture Measurements and Flow Experiments on a Single Natural Fracture” International Journal of Rock Mechanics and Mining Sciences & Geomechanics Abstracts, Volume 33, Issue 4, , Pages 395-404, June 1996

62) Keller A.A., “High Resolution CAT Imaging of Fractures in Consolidated Materials” International Journal of Rock Mechanics and Mining Science, Volume 34, No ¾, page 358, paper number 155, 1997.

63) Akin S., Kovscek A.R., “Computerized Tomography in Petroleum Engineering Research,” Geological Society, London, Special Publications, v. 215, p. 23-38, 2003.

64) Verbal Communication with Barry Newton, Weatherford Laboratories, Houston, TX.

65) Best S. T., Sears S. O., Willson C. S., “Integration of Imaging Techniques over Multiple Scales”, 2010.

66) Abell A.B., Willis K.L, Lange D.A., “Mercury Intrusion Porosimetry and Image Analysis of Cement Based Materials,” Journal of Colloid and Interface Science, 211, 39-44, 1999.

67) Rasband W.S., ImageJ, U.S. National Institutes of Health. Available: http://rsb.info.nih.gov/ij/. Bethesda, MD, 2009.

68) Bhattad, P., W, Willson C. S, Thompson K.E., “Segmentation of low-contrast three-phase X-Ray computed tomography images of porous media”. Proceedings of the GeoX 2010: 3rd International Workshop on X-ray CT for Geomaterials edited by K. Alshibli and A.H. Reed, pp. 254-261, New Orleans, LA, March 1-3, 2010

`

69) OFITE Drilling Fluids Manual, Downloaded from http://www.ofite.com/products.asp?category=Drilling_Fluids

70) Bishop P. L., Gong R., Keener T. C., “Effects of Leaching on Pore Size Distribution of Solidified/ Stabilized wastes”, 1992.

`

APPENDIX A
Cement Sections Prepared For Material Characterization Techniques

Figure A.1: Cement Core (1 in by 12 in)

Figure A.2: Dissected Cement Core (Top View)

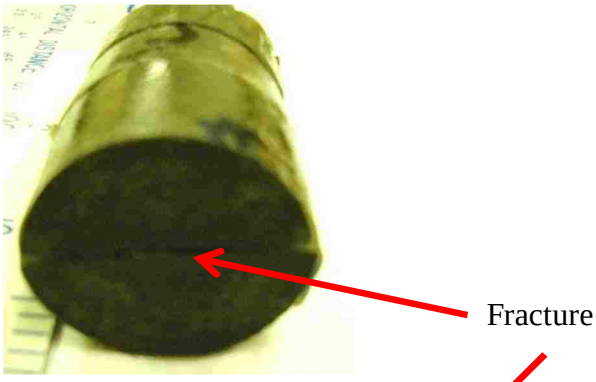

Figure A.3: Side View of Dissected Cement

Figure A.4: Top View of the Fracture

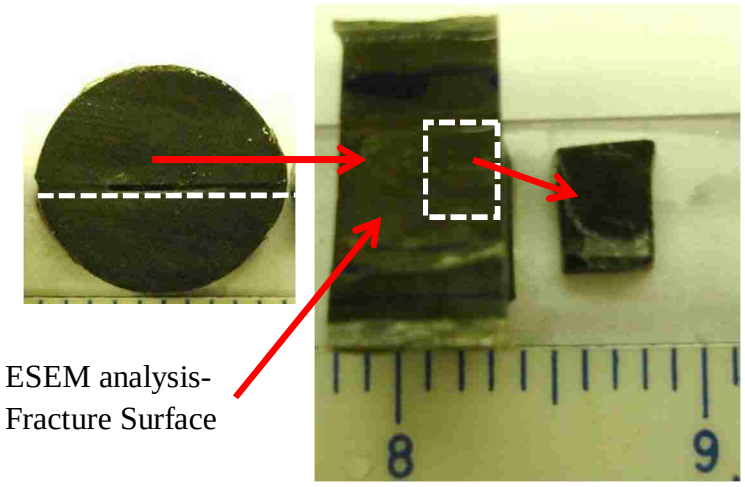

Figure A.5: Section Prepared for XRD analysis (cut from the fracture surface)

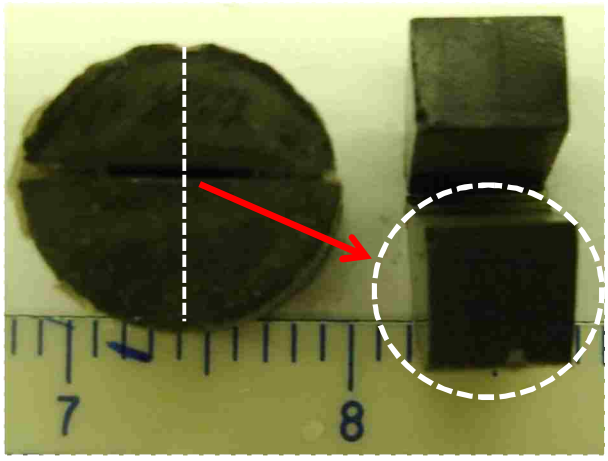

Figure A.6: Section Prepared for MIP analysis (circled region)

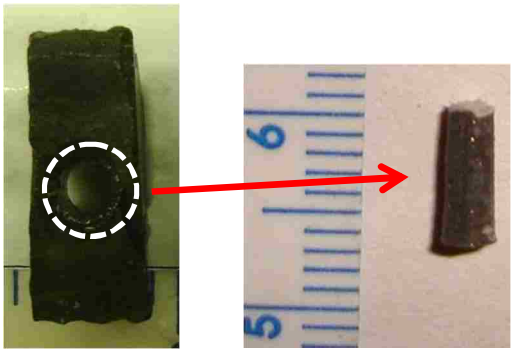

Figure A.7: Section Prepared for Micro-CT analysis (drilled from the fracture surface)

`

APPENDIX B
Micro-CT Images of the Reacted LP_7-8 (Inlet) Sample

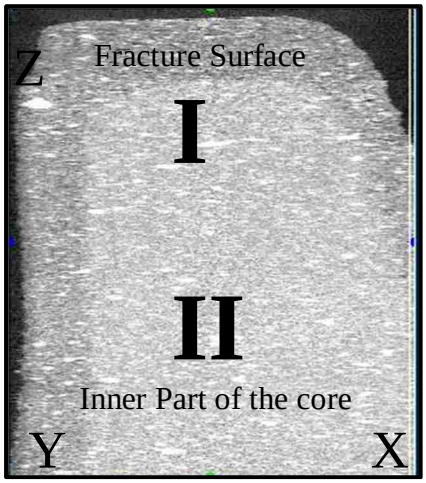

Figure B.1: Cross-sectional view of Micro-CT image (1.93 ×1.93 × 7.5 mm^3) along the length of mini-core

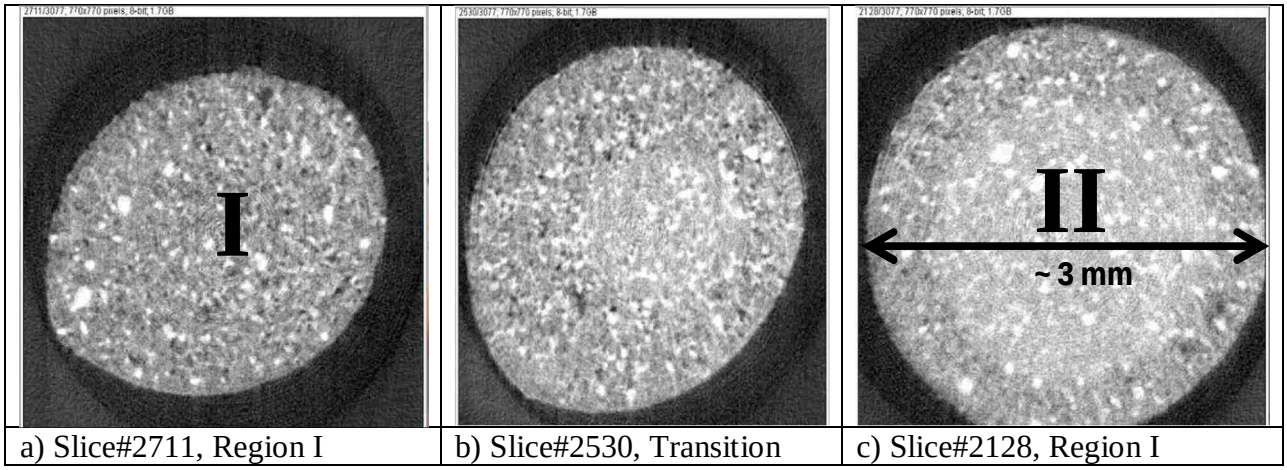

a) Slice#2711, Region I	b) Slice#2530, Transition	c) Slice#2128, Region I

Figure B.2: Micro-CT image (axial slices) for reacted cores for the low pressure experiment (inlet section)

Table B.1: Image Based Porosity for the low pressure experiment (inlet section)
for the low pressure experiment (outlet section)

Unreacted-Low Pressure	Reacted-Low Pressure	
Porosity	Porosity-Region I	Porosity-Region II
0.25 %	2.15 % (Threshold-35)	0.75% (Threshold-70)

`

APPENDIX C
Additional ESEM Images

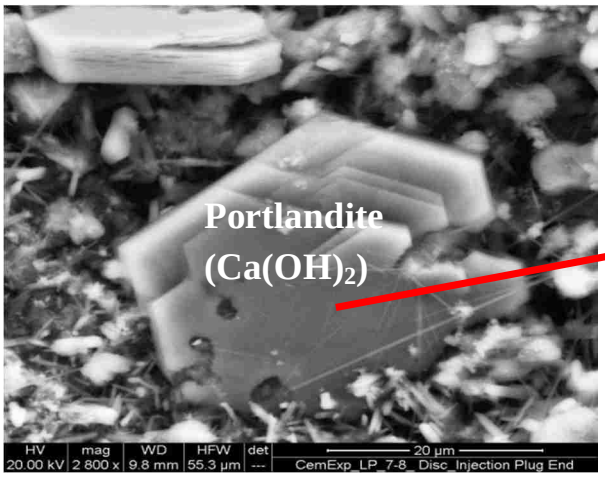

Element	Wt %	At %
O K	47.94	68.25
AlK	05.75	04.86
SiK	01.00	00.81
ClK	04.56	02.93
CaK	40.74	23.15

Figure C.1: Portlandite Mineral and its EDS analysis

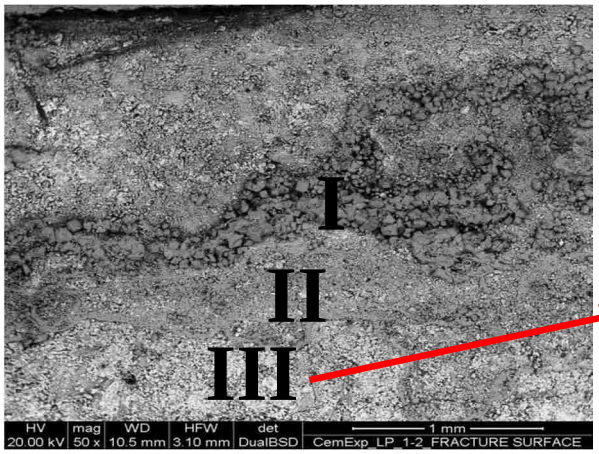

Element	Wt %	At %
O K	24.07	48.46
SiK	03.02	03.47
ClK	00.47	00.42
K K	00.52	00.43
CaK	27.19	21.85

Figure C.2: Fracture Surface of the Reacted LP_1-2 (Outlet)

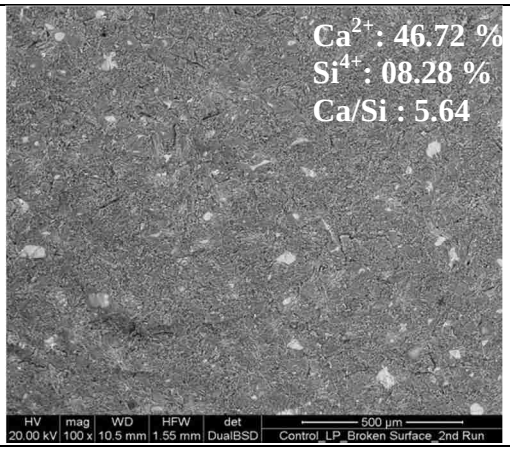

a) Unreacted core

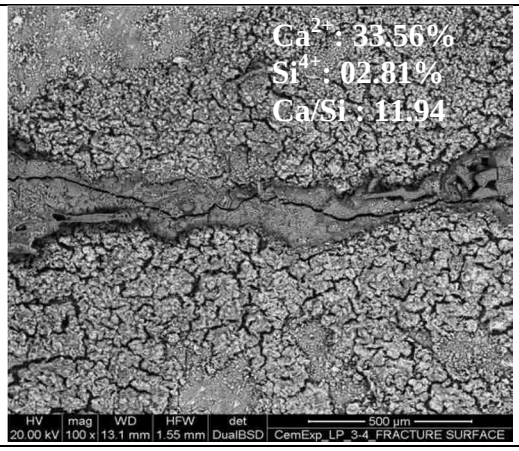

b) Reacted LP_3-4, calcite precipitation

Figure C.3: Fracture Surface of the Reacted LP_3-4

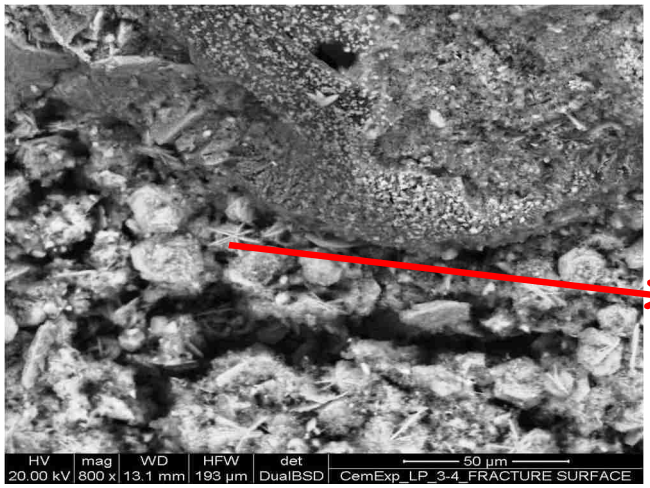

EDS of the needle shape structure (C-S-H)

Element	Wt %	At %
O K	39.63	63.28
MgK	00.69	00.73
SiK	01.83	01.66
ClK	01.24	00.89
CaK	41.92	26.72
FeK	14.69	06.72

Figure C.4: Fracture Surface of the Reacted LP_3-4

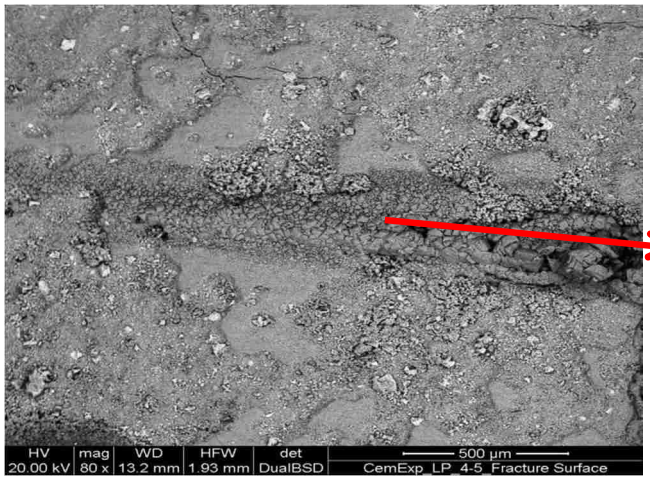

Element	Wt %	At %
O K	41.79	64.67
MgK	00.84	00.86
SiK	01.23	01.08
ClK	00.90	00.63
CaK	47.40	29.28
FeK	07.83	03.47

Figure C.5: Fracture Surface of the Reacted LP_4-5

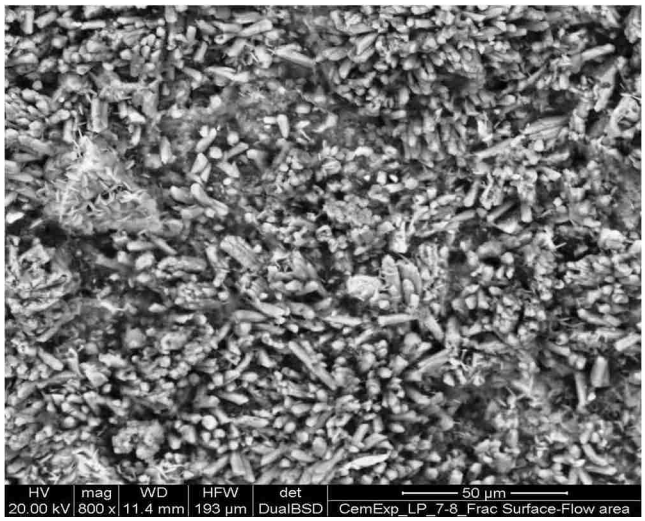

EDS of the entire image

Element	Wt %	At %
O K	30.63	53.72
AlK	01.83	01.90
SiK	01.83	01.83
ClK	01.23	00.98
CaK	46.48	32.54
FeK	17.99	09.04

Figure C.6: Fracture Surface of the Reacted LP_7-8 (Inlet)

`

VITA

Tevfik Yalcinkaya was born in Tarsus, Turkey, in August, 1984. He received his Bachelor of Science degree in the Petroleum and Natural Gas Engineering Department from the Middle East Technical University (M.E.T.U.), Ankara, Turkey, in 2007. After graduating from M.E.T.U., he worked as a mud engineer for a short period of time in the drilling operations in Turkey. He then attended Louisiana State University in Baton Rouge, Louisiana, where he is currently pursuing his Master of Science degree. His research interests include drilling and completions engineering. The degree of Master of Science in Petroleum Engineering will be conferred in December 2010.

`